Alma Mater Studiorum - Università di Bologna

DOTTORATO DI RICERCA IN MECCANICA E SCIENZE AVANZATE DELL'INGEGNERIA

Ciclo 34

Settore Concorsuale: 09/A1 - INGEGNERIA AERONAUTICA, AEROSPAZIALE E NAVALE

Settore Scientifico Disciplinare: ING-IND/05 - IMPIANTI E SISTEMI AEROSPAZIALI

TOWARDS AUTOMATION OF CONSTELLATION MANAGEMENT WITH ANALYTICAL MODELS FOR COLLISION AVOIDANCE

Presentata da: Giacomo Curzi

Coordinatore Dottorato

Marco Carricato

Supervisore

Paolo Tortora

Co-supervisore

Dario Modenini

Esame finale anno 2022

Abstract

The growing interest for constellation of small, less expensive satellites is bringing space junk and traffic management to the attention of space community. At the same time, the continuous quest for more efficient propulsion systems put the spotlight on electric (low thrust) propulsion as an appealing solution for collision avoidance.

Starting with an overview of the current techniques for conjunction assessment and avoidance, we then highlight the possible problems when a low thrust propulsion is used.

The need for accurate propagation model shows up from the conducted simulations. Thus, aiming at propagation models with low computational burden, we study the available models from the literature and propose an analytical alternative to improve propagation accuracy.

The model is then tested in the particular case of a tangential maneuver. Results show that the proposed solution significantly improve on state of the art methods and is a good candidate to be used in collision avoidance operations. For instance to propagate satellite uncertainty or optimizing avoidance maneuver when conjunction occurs within few (3-4) orbits from measurements time.

Acknowledgements

I would like to thank Prof. Paolo Tortora and Prof. Dario Modenini for giving the possibility to start this work. More importantly, I thank them for the provided support during my research path giving advice without imposing directions.

Secondly, I would like to thank my family for the moral support, especially in the more stressful periods of this journey.
Lastly, a special thank to my grandfather Almerino who taught me to work passionately and attentive to details.

Contents

List of Tables

List of Figures

List of Acronyms

AI	Artificial Intelligence
CAM	Collision Avoidance Maneuver
CDM	Conjunction Data Message
COLA	COLlision Avoidance
ECI	Earth-Centered-Inertial frame of reference
EKF	Extended Kalman Filter
ESA	European Space Agency
GMM	Gaussian Mixture Model
GNSS	Global Navigation Satellite System
GPS	Global Positioning System
GSF	Gaussian Sum Filter
GVM	Gauss Von-Mises
HBR	Hard Body Radius
ISS	International Space Station
JSpOC	Joint Space Operations Center
LEO	Low Earth Orbit
MC	Monte Carlo
ML	Machine Learning
NASA	National Aeronautics and Space Administration
OE	Orbital Elements
Pc	Probability of Collision
PDF	Probability Density Function
SST	Space Surveillance and Tracking
STT	State Transition Tensor
TCA	Time of Closest Approach
UT	Unscented Transform
WSPRT	Wald Sequential Probability Ratio Test

List of Symbols

$\mathbf{0}$	Null matrix
Az	Azimuth angle
$\boldsymbol{A}$	Gradient (Jacobian) of $\boldsymbol{f}$
$\boldsymbol{\mathfrak{A}}$	Integral of $\boldsymbol{A}$
a	Semi-major axis of an orbit
$\boldsymbol{\alpha}$	Spacecraft orbital elements state vector
$\boldsymbol{a}$	3-dimensional perturbative acceleration
α	confidence value
$\boldsymbol{b}$	3-dimensional, scaled, non-dimensional acceleration
$\boldsymbol{C}$	Spacecraft covariance matrix
$\delta\boldsymbol{\alpha}$	Orbital elements difference state vector
$\delta(\cdot)$	Order function $\cdot$
$\delta\cdot$	Error differential of $\cdot$
E	Eccentric anomaly
El	Elevation angle
e	Eccentricity
ϵ	Generic small parameter (non-dimensional)
$\mathbb{E}$	Elliptic integral of second kind
$\mathbb{F}$	Elliptic integral of first kind
f	True anomaly
$\boldsymbol{f}$	Gauss' Planetary Equations with E as independent parameter
$\boldsymbol{f}_{\boldsymbol{b}}^{1}$	Short notation for the multiplication result of $\boldsymbol{f}^1$ and $\boldsymbol{b}$
$\mathfrak{f}$	Integral of $\boldsymbol{f}$
Φ	Generic flow equation
$g(\cdot)$, $\boldsymbol{g}(\cdot)$	Generic function (vector function)
h^0	Scalar Auxiliary symbol for the time equation
$\boldsymbol{h}^1$	Vectorial Auxiliary symbol for the time equation
$\mathfrak{h}$	Integral of $\boldsymbol{h}$
$\mathcal{I}$	Interval on the set of real numbers

$\boldsymbol{I}$	Identity matrix
$I_{\cdot}$	Short notation for an integral, $(\cdot)$ distinguish the definition
i	Inclination
L, k	Arbitrary positive constant
$\boldsymbol{\mu}$	Generic mean vector
μ	Earth planetary constant
k, m	Auxiliary constants in elliptic integrals argument
n	Mean motion
$\boldsymbol{n}$	Orbital angular momentum vector (normal)
N	Number of samples
$\mathcal{O}(\cdot)$	Quantity in the order of $\cdot$
ω	Argument of pericenter
Ω	Argument of ascending node
$\mathcal{P}$	Probability (density) distribution function
$\boldsymbol{\Psi}$	Gauss' Planetary Equations with t as independent parameter
P (P_c)	Generic probability (probability of collision)
$\mathbb{\Pi}$	Elliptic integral of the third
$\boldsymbol{r}$	Spacecraft Cartesian position
R-T-N	Radial-Tarnsversal-Normal frame of reference
R_{hbr}	Hard Body Radius
ρ ($\boldsymbol{\rho}$)	Relative position magnitude (vector)
$\mathbb{R}$	Set of real numbers
$\boldsymbol{R}_{\cdot}^{*}$	Rotation Matrix to be left-multiplied, passive rotation, transform a vector written in $\cdot$ to a vector written in $*$.
$\boldsymbol{s}$	Spacecraft Cartesian state vector
$\boldsymbol{\mathcal{S}}$	Spacecraft augmented (Cartesian) state vector
$\boldsymbol{S}$	Generic sample covariance matrix
$\boldsymbol{\Sigma}$	Generic covariance matrix
σ	Scalar Standard Deviation
T	Time period
$\boldsymbol{t}$	Traverse direction vector (bi-normal)
t	Time
$\boldsymbol{\theta}$	Generic auxiliary vector
$\boldsymbol{U}$	Generic non-singular matrix

$\boldsymbol{\mathcal{U}}$	Near-identity transformation
$\boldsymbol{u}$	Periodic part of the near-identity
$\boldsymbol{v}$	Spacecraft velocity position
$\nu, \boldsymbol{\nu}$	Relative velocity magnitude (vector)
V	Generic integration volume
W	Generic weight scalar
$\boldsymbol{x}$	Generic state vector
$\mathbf{x}$	x-axis of a reference frame
$\mathbf{y}$	y-axis of a reference frame
$\mathbf{z}$	z-axis of a reference frame
$\boldsymbol{y}, \boldsymbol{z}$	Averaged versions of $\boldsymbol{x}$

Accents, superscripts and subscripts

$\bar{\cdot}$	Sample average or averaged version of $\cdot$
$\hat{\cdot}$	Unitary vector of $\cdot$
$\breve{\cdot}$	desired maximal value for the quantity $\cdot$
$*$	Perturbed version of a quantity, e.g. $\boldsymbol{\rho}^*$
$\star$	Variant meaning of a quantity, e.g. $\boldsymbol{\mathcal{S}}^\star$
$\tilde{\cdot}$	Non-dimensional quantity of $\cdot$
r	Reduced version of a quantity, first five components of a vector or upper-left 5×5 block of a matrix, e.g. $\boldsymbol{f}_r$
c	Used to refer to a quantity evaluated at the chief or reference orbit, e.g. $\boldsymbol{\alpha}_c$
0	Used to refer to the initial value of a quantity, e.g. $\boldsymbol{x}_0$
$\cdot^i$	With a function $\cdot$ and $i \in \mathbb{N}$, i is the expansion order of the function in a Taylor series
d	With $d \in \mathbb{N}$, is the dimension of a space
$\mathfrak{t}$	Used as subscript or superscript to refer to the "target"
$\mathfrak{c}$	Used as subscript or superscript to refer to the "chaser"
$\mathfrak{b}$	Used as subscript or superscript to refer to the "b-plane" (projected)
$\mathfrak{e}$	Used as subscript or superscript to refer to the "encounter frame of reference"
l	Used as subscript to indicate logarithmic quantity
η	Used as subscript to refer to the normal component in the normal-tangential-binormal
τ	Used as subscript to refer to the tangential component in the normal-tangential-binormal

n	Used as subscript to refer to the binormal component in the normal-tangential-binormal, i.e. angular momentum direction

Operators

$\dot{(\cdot)}$	Total derivative of $(\cdot)$ equivalent to $\frac{d\cdot}{d*}$
$Pr(\{\cdot\})$	Probability of the event $\{\cdot\}$
$tr(\cdot)$	Trace of a matrix
$det(\cdot)$	determinant of a matrix
$\lvert\cdot\rvert$	absolute value if $\cdot$ is a scalar, determinant if $\cdot$ is a matrix
$\otimes$	Kronecker product
$vec(\cdot)$	Vectorization operator
$\nabla_\cdot$	Gradient with respect to $\cdot$
$(\cdot)^T$	Transpose of a matrix
$[\cdot]^\times$	Cross-product matrix, e.g. $\boldsymbol{t} \times \boldsymbol{n} = [\boldsymbol{t}]^\times \boldsymbol{n}$

1

Introduction

Satellites have become fundamental for everyday life. Most of the services we use, from communications to surveillance and monitoring are gradually migrating towards space-based architectures. Primarily because of the global coverage that those services have to guarantee.

For instance, it may be fundamental for an end-user to access web services while traveling across the ocean where cellular network has no installation. In case the web services were provided through satellite link, the user location would not be a limitation, provided that some satellites are in view of the user itself.

In this introduction, we start by justifying the reason for constellations of satellite to exist, highlighting technical challenges. With this in mind, we then focus on a particular challenge becoming the research topic for this PhD dissertation.

1.1 Mega-constellations

A constellation of satellites can be defined as a set of more than two spacecraft flying in a coordinated manner to solve a given task.

If it is possible to give a definition of constellation, it is instead not straight forward to define a mega-constellation. In fact, by mega-constellation we mean a constellation having a large number of elements, although no commonly accepted quantification of "large number" exists.

Continuous coverage of ground surface areas or short revisit time are typical needs for an end-user application potentially justifying mega-constellations. Examples can be disaster monitoring, ship/aircraft tracking, atmosphere monitoring or web services.

1.1.1 New Space Economy

If, at the beginning of the space era, the access to space was exclusively owned by governance agencies, in the era of the New Space Economy access is mainly offered by private companies, or by a mixed collaboration between governance and private entities. This shift is motivated by mainly two facts: firstly, governmental agencies do not have anymore the strong impulse from politics, which was instead present during the second half of the 20th century. Secondly, venture capitalists started financing access to space in general.

This new framework is establishing a strongly competitive environment leading to an easier access to space. Combined with the growing real-time data delivery and global coverage needs, this is justifying technically and economically the existence of space-based solutions such as mega-constellations. Constellations of satellites appear in fact to be a solution raising a growing interest (Lal et al., 2017), (Curzi et al., 2020), (Kulu, 2021), (Miraux, 2022).

1.1.2 Challenges

Continuous deployment of spacecraft constellations will require a paradigm shift with respect to the way space missions are currently handled, with major challenges to be faced. It has been the focus of the first part of this PhD to locate those operational challenges for a successive extensive study (Curzi et al., 2020). The identified challenges were of three kinds:

1. Constellation Management: regards the handling of a single constellation by the owner.
   Clearly, the larger the constellation the larger the owner's effort is if they decide to manage each element of the constellation as a single satellite. Automation of spacecraft operations and telemetry monitoring (e.g. though

Artificial Intelligence) may help focusing efforts only on those elements that does need attention.

2. Communication Management: regards the handling of the owners/users communication with their satellites.
   Radio equipment and environmental limitations guide the owners to choose among very selected frequency channels. At the same time, the traffic data volume is foreseen to increase significantly because of the emerging constellations (operations and generated payload data). Then, it is easy to imagine a congestion of radio channels in the future so that protocol optimization, high frequency communication and infrastructure sharing are of key interest.

3. Space Traffic Management: consist of ensuring an adequate clearance between objects in space so that every spacecraft can accomplish its mission (Muelhaupt et al., 2019).
   The growing number of objects in space clearly leads to an increased probability of having collisions, which would likely destroy the colliding objects or cause mission failure. Also, the debris generated in those collisions may contribute to further collisions (Kessler syndrome).
   Although well-established surveillance tracking methods and collision avoidance procedures are available to spacecraft operators, both are not easily scalable to handle the needs of (large) constellations of satellite. From the tracking point of view, limits to scalability are imposed by the finite traffic volume capacity of current ground tracking systems. From the procedural point of view, limitations arise due to both the high workload needed to handle a single conjunction and the reliability (or conservativeness) of the risk assessment method being used.

Among the three wide areas above, the space traffic issue is arguably the most urgent because of the catastrophic consequences of space collisions. Such consequences are both in economic terms, because the colliding spacecraft are usually lost, and in terms of space sustainability, because a large amount of space debris may endanger any further space activity. Collision avoidance (COLA) operations are thus fundamental for the health of space environment and it has been chosen as the main topic of this PhD.

1.1.3 Ground-based versus spaceborne conjunction assessment

How much of the conjunction assessment shall be done on ground and how much shall or could be done onboard satellite is important for mega-constellations. Automation, cited as a key factor in the previous paragraph, could be implemented either on ground or on board. At the moment, a clear trend between the two is not defined. From one side, ground-based assessment allows for running complex and computationally expensive algorithms, while implying a heavier workload for the ground stations. On the other side, onboard automation alleviates the ground workload but the limited computational power constrains the complexity and performance of the algorithms that can be actually used.

Mega-constellations would certainly benefit from increasingly shifting towards onboard automation of COLA operations, as the rate of collision alerts is expected to become unacceptably high to be entirely managed from ground (Krage, 2020). On the other hand, such a shift would imply an unsupervised avoidance process which must be maintained safe enough and computationally efficient at the same time.

Historically, the conjunction assessment has been completely performed on ground, ESA's approach in using JSpOC's (Joint Space Operations Center) data is an example (Merz et al., 2017). However, the above cited need for automation hints for moving at least part of the COLA tasks onboard (Muelhaupt et al., 2019). Under this action line for instance, Serra et al. (2016) and Ding et al. (2019) propose very efficient, analytical methods for fast collision probability computation.

1.1.4 Possible lines of action

Concerning the trends in collision avoidance, we can highlight the following research topics:

1. Data-sharing: many active object are nowadays having onboard GNSS or are tracked with high precision for other purposes. It would be of great value for COLA the sharing of updated data on a common database. As a result, the database reflecting space situational awareness would be updated more frequently and be inherently more precise.

2. Low-cost measurement systems: a common problem is the availability of

fresh and accurate tracking data for orbit determination. At the moment this service is only available under purchase option or because JSpOC has already detected a close approach. Having alternative, possibly low-cost, sources of tracking data would be highly beneficial.

3. Uncertainty propagation: this is an essential task in computing any collision risk metric (Krage, 2020). With the tendency of demanding onboard more computations, analytical solutions for onboard nonlinear uncertainty propagation can be valuable.

4. Risk classification: this is probably the most overlooked aspect of collision avoidance with operators heavily relying on classical metrics which are either inefficient, thereby leading to an excessive maneuver rate (confidence interval) or unsafe (i.e. subject to false confidence problem) (Hejduk, 2019). Searching for safer collision metrics would be interesting.

5. Maneuver planning and coordination: tools for computing collision avoidance maneuvers in a single conjunction are well established; a problem arising in case of mega-constellations is the coordination of multiple maneuvers when the number of warnings become too high to be handled by a manual procedure. Automation of COLA maneuvers coordination would be of great interests for operators. With the tendency of demanding those tasks in orbit, the efficiency of such maneuvers computation is of paramount importance.

   In this respect, a key aspect is the increasing consideration of low thrust, electric propulsion systems for COLA (e.g. Willis and D'Amico (2018)), which poses additional operational constraints compared to classic, chemical propulsion based, impulsive maneuvers.

1.2 Thesis focus

Being electric propulsion inherently a low thrust system, its application to COLA is not trivial, yet it is not sufficiently explored in the literature.

After the seminal work at the US air force in 1991 (Widhalm and Heise, 1991) showing the feasibility of low thrust, and the case study of CRYOSAT project in early 2000 (Graziano et al., 2001), only very recently the issue regained attention.

In their paper, Petit et al. (2019) confirmed that low thrust evasive maneuvers are possible and shall start between 4 and 8 orbital periods prior to closest approach. Hernando-Ayuso and Bombardelli (2021) study instead the optimality of low thrust COLA maneuvers in circular orbits. None of them however, addressed the problem of the uncertainties that those systems may introduce in the COLA process.

When computation and/or optimization of low thrust maneuvers is performed in the context of COLA operations, one shall consider that the ultimate goal is assessing the reduction in the risk of collision. As a result, the design of a specific maneuver computation tool shall be driven by accuracy requirements in terms of the employed collision risk index. With this in mind, the following research questions arise:

1. Which are the requirements for an orbit propagator under low thrust to be used for COLA operations?
2. Can we fulfil such requirements with an efficient analytic orbit propagator?

To answer, at least in part, those questions, this research studies the effects of low thrust engine characteristics when used in collision avoidance and propose an analytic model to propagate position (or uncertainty) in such situations. Being the model analytic, it is computationally light and opens the possibility to the implementation of a lighter, autonomous, onboard maneuver computation unit.

Although the motivating use case is that of spacecraft (mega-) constellations, the availability of computational efficient algorithms for maneuver computation may be beneficial to generic collision avoidance scenarios. Surely however, the biggest benefit will be drawn by large constellations because the proposed model is a step towards automation of the COLA process.

1.2.1 Document structure

The next chapter is dedicated to the collision avoidance process for an in-depth understanding of the problem mechanics.

The following chapter addresses research question 1, by elaborating orbit propagation requirements for COLA, and studying in detail the challenges arising from the use of low thrust.

The forth chapter addresses research question 2, by developing the theory and application of a high accuracy analytic orbit propagator for the orbital motion under low thrust, along with its performance assessment.
Conclusions highlight achievements and limitation of the present work as well as promising future research directions.
Finally notice that, auxiliary mathematical derivations are collected in dedicated chapter appendices.

2

Collision avoidance process

In this chapter an overview of the process and mathematics behind COLA is given. In doing so, we summarize the state of the art digging into mathematical details only in the aspects needed for this dissertation, e.g uncertainty propagation and the calculation of classical collision metrics.
We start with the definition of encounter and its geometry introducing then the COLA process.

2.1 Encounter definition

It is commonly defined (close) encounter or conjunction the situation in which two space objects are located at a relative distance below some threshold. The threshold is usually fixed following heuristic criteria which are however out of scope for this discussion, typically it is something in the order of few kilometers (Chan, 2008).

Let us define the *Cartesian State Vector* of a spacecraft the column vector made by position $\boldsymbol{r}$ in km and velocity $\boldsymbol{v}$ in km/s both written in some Earth Centered Inertial (ECI) frame of reference, mathematically:

$$\boldsymbol{s} = \begin{bmatrix} \boldsymbol{r} \\ \boldsymbol{v} \end{bmatrix}$$

Moreover, we call $\boldsymbol{\rho}$ and $\boldsymbol{\nu}$ the difference between Chaser's and Target's positions and velocities respectively.

For every encounter, it is possible to define a *Time of Closest Approach*, commonly indicated as t_{ca} or TCA, as the instant of time at which the minimum relative distance

$$\min_t(\|\boldsymbol{\rho}\|)$$

between the objects is reached.

The positions and velocities of target and chaser at TCA defines a relative geometry in which the so called encounter plane (or b-plane) can be located. The b-plane is that plane containing the relative distance $\boldsymbol{\rho}$ and orthogonal to the relative velocity $\boldsymbol{\nu}$.

Remark 2.1. Note that the orthogonality of $\boldsymbol{\rho}$ and $\boldsymbol{\nu}$ at TCA follow from the realization of $\min(\|\boldsymbol{\rho}\|)$. This can be easily shown considering the equality $\boldsymbol{\nu} = \dot{\rho}\hat{\boldsymbol{\rho}} + \rho\dot{\hat{\boldsymbol{\rho}}}$ with $\rho = \|\boldsymbol{\rho}\|$. △

The *encounter frame of reference* is defined by the orthonormal vectors $\hat{\mathbf{x}}_{\mathrm{t}}, \hat{\mathbf{y}}_{\mathrm{t}}$ belonging to the b-plane and $\hat{\mathbf{z}}_{\mathrm{t}}$ in the direction of relative velocity, that is:

$$\hat{\mathbf{x}}_{\mathrm{t}} = \frac{\boldsymbol{\rho}_{\mathrm{t}}}{\|\boldsymbol{\rho}_{\mathrm{t}}\|} \quad \hat{\mathbf{y}}_{\mathrm{t}} = \frac{\boldsymbol{\rho}_{\mathrm{t}} \times \boldsymbol{\nu}_{\mathrm{t}}}{\|\boldsymbol{\rho}_{\mathrm{t}} \times \boldsymbol{\nu}_{\mathrm{t}}\|} \quad \hat{\mathbf{z}}_{\mathrm{t}} = \hat{\mathbf{x}}_{\mathrm{t}} \times \hat{\mathbf{y}}_{\mathrm{t}}$$

The subscript t indicates that the vectors are written in the target's R-T-N frame. For a target's osculating state $\boldsymbol{s}$, we define R-T-N frame the reference system centered at the target's center of gravity and made by the vectors:

- $\hat{\boldsymbol{r}} = \frac{\boldsymbol{r}}{\|\boldsymbol{r}\|}$ the outgoing direction from the Earth's center of gravity to the spacecraft center of gravity.
- $\hat{\boldsymbol{n}} = \frac{\boldsymbol{r} \times \boldsymbol{v}}{\|\boldsymbol{r} \times \boldsymbol{v}\|}$ the angular momentum direction.
- $\hat{\boldsymbol{t}} = -\hat{\boldsymbol{r}} \times \hat{\boldsymbol{n}}$ the transverse direction.

Given the encounter frame definition above, it can be defined a rotation matrix between the target's R-T-N frame and the encounter frame, that is:

$$\boldsymbol{R}_{\mathrm{t}}^{\mathrm{e}} = \begin{bmatrix} \hat{\mathbf{x}}_{\mathrm{t}}^T \\ \hat{\mathbf{y}}_{\mathrm{t}}^T \\ \hat{\mathbf{z}}_{\mathrm{t}}^T \end{bmatrix}$$

Analogously one could define rotation matrices rotating the frame of reference from target's R-T-N ($\mathfrak{t}$) to chaser's one ($\mathfrak{c}$) and vice-versa, $\boldsymbol{R}_{\mathfrak{t}}^{\mathfrak{c}}$.
The usage of such matrix is intended passive, therefore for instance, the rotation matrix $\boldsymbol{R}_{\mathfrak{t}}^{\mathfrak{c}}$, if left-multiplied, writes a vector from the frame target's R-T-N into the chaser's R-T-N.

2.2 Process overview

The collision avoidance process can be divided into 4 consecutive segments:

1. Object tracking/measurement system: determination of the object position and uncertainty through measurements (radar, laser, GNSS, etc.).

2. Position and uncertainty propagation: object's ephemerides are propagated up to the time of closest approach where collision statistics has to be computed. Typically into this step, a fast heuristic scanning detects dangerous close approaches, for those only the uncertainty is then propagated to compute statistics.

3. Metric computation and event classification: once collision statistics are computed they need to be evaluated deciding whether to maneuver or not.

4. Maneuver computation/optimization: if needed and possible, dangerous close approaches are mitigated scheduling an evasive maneuver (CAM) to either colliding objects.

Although in principle these segments are distinct and consecutive, in practice they often end up into an iterative process. The reason for this can be located mainly into two factors:

1. As the closest approach becomes nearer in time, better collision statistics can be obtained because for instance the propagation model is more accurate for shorter periods or one can get better tracking measurement. Then, the risk metric can be updated and the maneuvering decision reconsidered.

2. The evasive maneuver significantly changes collision metric to mitigate the risk. Suppose the avoidance maneuver is performed with a system affected

by significant imperfect realization. The realization error affects the collision metric so that maneuver shall account for this to achieve the desired mitigation effect. As a result, the uncertainty propagation task merges with the maneuver computation one.

2.3 Measurement system

The process to calculate the trajectory of an unknown space object based on a set of observables is known as orbit determination. A variety of measurement systems can be used to provide the observables, an historical summary is given by Vetter (2007). The most classic techniques rely on:

- Radar systems (either passive or active)
- Optical or laser systems (they usually need reflectors onboard the target object)
- Radio-interferomety systems
- Global Navigation Satellite System - GNSS (in the last decades)

In the framework of collision avoidance, we have the need to be both precise and able to track passive objects. The systems giving this best compromise are radar systems. Within this view, the currently most advanced and accepted system for collision avoidance is the global network of radars provided by the US army. Data from those radars are processed and dispatched by JSpOC (Joint Space Operation Center), alias the 18-th US squadron.

In the last years however, also the European Space Agency is building his own tracking network within its Space Surveillance and Tracking (SST) program.

Private owners as well are emerging to offer tracking services, e.g. LeoLabs Inc.

Like any measurement system, radar systems are affected by unavoidable uncertainties. Typical uncertainties for those systems are given in terms of standard deviation which ranges around 10-100 meters (Vetter, 2007) depending on the quality.

Passive radar systems (the most common) typically provides observables in range, elevation and azimuth angles (and range rate if doppler feature is used). For

Table 2.1: Radar measurement error standard deviations (courtesy of Goff et al. (2015))

$Radar$	$\sigma_\rho(m)$	$\sigma_{Az}(deg)$	$\sigma_{El}(deg)$	$\sigma_{\dot{\rho}}(m/s)$
good	5	0.01	0.01	0.05
average	25	0.03	0.03	0.2
poor	100	0.05	0.05	10

these type of observables, a realistic uncertainty estimate is given by Goff et al. (2015) which we report in the Table 2.1.

For cooperative objects, more precise tracking may be available as we can take advantage of GNSS or laser ranging. For instance, a satellite having access to GNSS signal can determine its own orbit with position accuracy in the order of 1-10 meters, depending on the kind of dynamic model implemented onboard. Alternatively, having surface reflectors allow for laser tracking (e.g. LARES); in this case the achievable accuracy can be less than 1 m.

2.4 Uncertainty description and propagation

The output of an orbit determination process provides the spacecraft state and its uncertainty at a given epoch within the measurement window. However, to compute collision metric we need such information around the time of closest approach. As a result, one needs to propagate forward in time the state vector uncertainty with some method. Among all the methods, in this section we review the most common ones digging into the details only for the Unscented Transform method, which will be later used in Chapter 4.

2.4.1 Types of uncertainties

Uncertainty quantification is the process of determining the error sources and their characterization.
There are different error sources causing uncertainty in collision avoidance, Luo and Yang (2017) gives an overview reporting among others:

- Navigation error (the most obvious), e.g. orbit determination error, attitude determination errors

- Modelling error, e.g. Earth gravity model truncation, atmospheric density truncation
- Actuation error, e.g. thrust vector misalignment

The uncertainty associated to such sources (real random phenomenons) can be described through probability density functions which, in turn, are uniquely determined by their *moments*. The concept of *uncertainty realism* mentioned by Poore et al. (2016) is based on these moments and links the mathematical description of uncertainty to the real phenomenon. It can be stated as follows:

Definition 2.1. *Given a random variable modelling a real probabilistic phenomenon, consider the real probabilistic central moments of the phenomenon (mean, covariance, skewness, etc.). Uncertainty realism is the property of the random variable (i.e. its PDF) to have the same (theoretically infinite) moments of the real phenomenon.*

Any collision metric is affected by uncertainty realism, as mentioned by Poore et al. (2016). Either due to measurement or propagation mismodelling, if uncertainty does not reflect reality, the estimated collision metric is going to be an approximation.

Realistic error (or uncertainty) models could be potentially obtained for all the above mentioned error sources and included in the propagation. However, this is a formidably complex task and, typically, only the most important error sources are retained, i.e. orbit determination and actuation errors (Yang et al., 2019), with possibly simplified modelling. Furthermore, although there are methods, such as Monte Carlo simulations, to propagate the uncertainty with high realism, these are computationally very intensive, so that approximate methods are adopted. As we shall see for instance, the Unscented Transform method is an approximation that allows to retain good realism up to the second moment, e.g. covariance realism.

In case the uncertainty distribution can be considered Gaussian during the complete propagation, than the description using the first two moments only is correct.

Typically, the error distribution of a space object's state at measurement times can be considered Gaussian. Given the non linearity of the orbital dynamics however, the gaussianity is hardly preserved in propagation, for instance after a few orbits in LEO (Kyle and PARK, 2016). The literature offers a variety of statistical tests to quantify the "gaussianity" of a probability density function. Two widespread examples are the Cramer-Von Mises and Kolmogorov-Smirnov tests (Poore et al., 2016), which differ mainly on the level of severity. Despite the concerns raised by the need for covariance realism, it is still customary in COLA to adopt only the first two central moments for the PDF description. This is, indeed, the most straightforward approach, which also proved to be effective in practical applications.

When referring to uncertainty, a distinction shall also be made regarding its nature, that can be classified as epistemic or aleatory.

Definition 2.2. *The epistemic (or systematic) uncertainty is related to the "known-unknown" for which an experiment prediction results to be wrong because a parameter cannot be determined accurately enough, although it would be theoretically possible. It reflects the lack of knowledge of the operator, originating an error on a modelling parameter which could be accessible but practically is not.*

Definition 2.3. *The aleatory (or stochastic) uncertainty is related to the "unknown-unknown" for which an experiment cannot be determined accurately enough because some modelling parameter are missing and are not accessible to the operator. Each time the same experiment is done a slightly different random result is obtained.*

Let us give a couple of intuitive examples for both types of uncertainties in a general scenario. Suppose we want to measure the free-fall time for a tennis ball from a fixed height, measuring *only* its height from ground. The height measurement error can be regarded as an epistemic uncertainty because we know that the measurement error has a detrimental effect on the prediction, we don't know its exact value but is theoretically accessible (one could measure the height as accurately as possible). The effect of the wind on the tennis ball cause instead an error to be regarded as aleatory uncertainty because it cause slightly different result each time we run the experiment and the operator has no access to wind measurement.

As the reader may understand, giving a taxonomy of errors usually depends on the degree to which we are willing to consider the parameter to be known or accessible (Kiureghian and Ditlevsen, 2009), (Fox and Ülkümen, 2011).

In collision avoidance for instance, Luo and Yang (2017) classifies the orbit de-

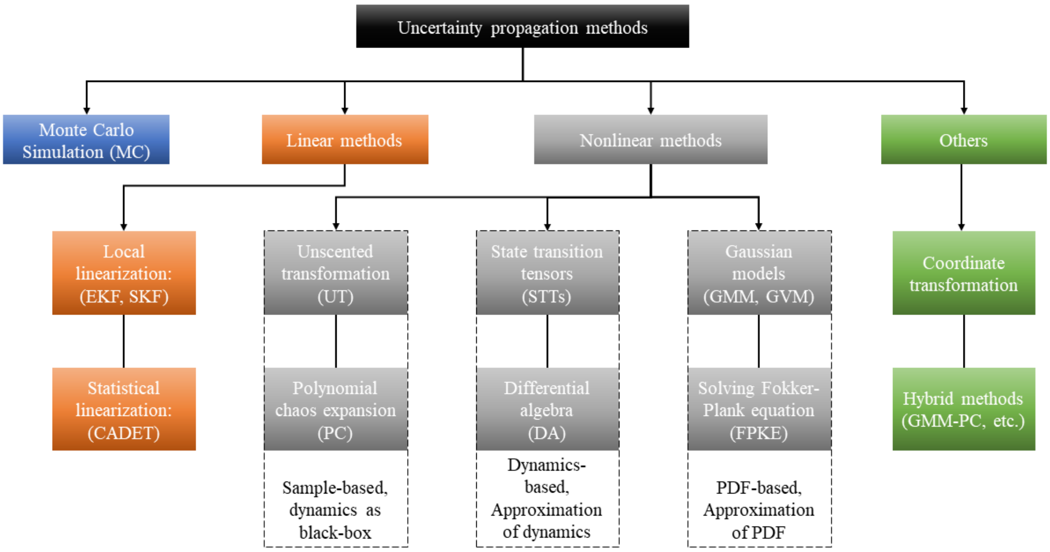

Figure 2.1: Schematic taxonomy of uncertainty propagation methods (reviewed version from Luo and Yang (2017))

termination (navigation) error as aleatory uncertainty, while dynamic modeling errors are classified as epistemic.

The distinction between epistemic and aleatory uncertainty can be significant because it may i) change the outcome of the decision (Kiureghian and Ditlevsen, 2009), ii) open the possibility of applications of new techniques. For instance, the Dempster-Shafer theory of evidence by Shafer (1976) is a new tool in the so-called imprecise probability theory able to deal explicitly with epistemic uncertainty.

2.4.2 Propagation methods

As explained by Luo and Yang (2017), and by Poore et al. (2016) there are currently many methods for propagating uncertainty. We recall the most used briefly here, whereas a graphic summary is given in the Figure 2.1.

1. Linear Covariance methods (EKF, Second Order EKF): very simple, computationally efficient methods, however, due to linearization, they are suitable for short term propagation only.

2. Unscented transform (non-linear method): propagates second and first or-

der moments of PDF non-linearly using sigma-points. As a result, it achieves a good mean and covariance realism (Wan and Merwe, 2000).

3. Polinomial Cahos (PC, non-linear method): describes a density function $f(\xi)$ using a set of orthogonal functions $\Psi(\xi)$, where ξ is a random input. Once the expansion of $f(\xi)$ is found (PCE, Polynomial Chaos Expansion), the PDF moments of $f(\xi)$ can be analytically evaluated or fund by random evaluation of PCE (Jones and Doostan, 2013). The biggest disadvantage of this method is the suffering of course of dimensionality.

4. State Transition Tensors (STT, non-linear): it is basically a covariance analysis method through taylor expansion. Still suffers computational complexity when high order expansion and needs differentiable equations (Poore et al., 2016).

5. Differential Algebra (DA, non-linear): usually used as the base for Taylor expansion or Monte Carlo analysis, allows fast propagation (Poore et al., 2016). Loosely speaking, the DA consist in a calculator storing a function as its Taylor expansion (analogously to normal algebra with the calculator storing floating point representation of real numbers). Using this representation, the DA allows fast operations between functions.

6. Solving Fokker-Plank-Kolmogorv equation(FPKE, non-linear): the FPKE is the basic equation describing a random variable propagation through its PDF. All other methods can be thought as approximating the solution of the FPKE. Numerical solutions of this equation are available only in simplified cases, and researchers are actively working on its solution, e.g. (Acciarini et al., 2020).

7. Gaussian Sum Filter or Gaussian Mixture Model (GSF, non-linear): it breaks the initial uncertainty into a sum of Gaussian PDFs with their own mean value and covariance. Propagating non-linearly the means and covariances a more realistic PDF is achieved. This is an approximation that suffers from curse of dimensionality, e.g. the more "Gaussian bits" the better, but this increases the computational cost (Kumar Vishwajeet and Puneet Singla, 2018).

8. Particle filter or Monte Carlo method (MC, non-linear): it is a brute force approach consisting of propagating many realizations of the initial measurement. From the propagated cloud of points one can infer statistical moments of the PDF. It is clearly the most reliable method and is used usually as a test bench for other methods. The main disadvantage is that in conjunction assessment, most of the events are characterized by low probability, meaning that a large number of samples are usually needed (Jones and Doostan, 2013).

9. Coordinate transformation (auxiliary method): used in coordination with one of the above methods, it can improve the validity of the prediction. In fact, it is empirically shown that the use of orbital elements is to be preferred to that of Cartesian coordinates for uncertainty propagation. Meaning that the Orbital element (OE) frame aids to keep the uncertainty distribution approximately Gaussian for longer time, thus increasing the time validity of the prediction. (Horwood et al., 2016).

2.4.3 Unscented Transform method

Suppose we are given the flow equation $\Phi(\boldsymbol{x}_0, t) : \mathbb{R}^d \times \mathbb{R} \rightarrow \mathbb{R}^d$ of a system propagating an initial state $\boldsymbol{x}_0$ to some final time t. Assume moreover $\boldsymbol{x}_0$ be distributed with some probability density function $\mathcal{P}$, where the initial average state is $\boldsymbol{\mu}_0$ and the $d \times d$ (non singular) initial covariance matrix is $\boldsymbol{\Sigma}_0$.
This method consists in propagating with the full flow equation only few selected points, called *sigma-points*. Then compute a weighted sample mean and covariance from those ones only.

There are different methods to obtain such sigma-points, here we use the ones proposed by Wan and Merwe (2000). In such approach there are exactly $N = 2d + 1$ points which at the initial time are taken to be:

$$\begin{aligned} \boldsymbol{x}_{00} &= \boldsymbol{\mu}_0 \\ \boldsymbol{x}_{0i} &= \boldsymbol{\mu}_0 + \left(\sqrt{(d+l)\boldsymbol{\Sigma}_0}\right)_i \quad for\ i = 1, ..., d \\ \boldsymbol{x}_{0i} &= \boldsymbol{\mu}_0 + \left(\sqrt{(d+l)\boldsymbol{\Sigma}_0}\right)_{i-d} \quad for\ i = d+1, ..., 2d \end{aligned} \tag{2.1}$$

where $l = \mathsf{a}^2(d+\kappa) - d$, with a an heuristic parameter determining the spread of the points around the true mean (usually $\mathtt{a}$ =1e-3), whereas κ is a similar scaling parameter of lower importance which we set to null. The notation $(\cdot)_i$ indicates the i-th column of the matrix.

Remark 2.2. In our specific application, the initial covariance may be small with respect to position magnitude (e.g. in ECI frame). Such small $\mathtt{a}$ may produce sigma-points too close to the starting position, triggering significant numerical errors. A larger $\mathtt{a}$ around 1e-1 is therefore a better choice. △

The sample mean and covariance at any time is given by a weighted average with coefficients:

$$\begin{aligned} W_0^m &= l/(d+l) \\ W_0^c &= l/(d+l) + 1 - \mathtt{a}^2 + \mathtt{b} \\ W_i^m &= W_i^c = 1/(2(d+l)) \end{aligned} \tag{2.2}$$

Where $\mathtt{b}$ reflects the knowledge of the modeling distribution. In our case, we are mainly concerned with distribution resembling gaussians, so we set $\mathtt{b} = 2$, the value for gaussian distributions.
Call $\boldsymbol{x}_i = \Phi(\boldsymbol{x}_{0i}, t)$, the first and second statistical moments are given by

$$\begin{aligned} \bar{\boldsymbol{x}} &= \sum_{i=0}^{N} W_i^m \boldsymbol{x}_i \\ \boldsymbol{S} &= \sum_{i=0}^{N} W_i^c (\boldsymbol{x}_i - \bar{\boldsymbol{x}})(\boldsymbol{x}_i - \bar{\boldsymbol{x}})^T \end{aligned} \tag{2.3}$$

It is possible to show that these formulas are exact for Gaussian distributions however, they are precise up to third order for any nonlinear flow Φ (Wan and Merwe, 2000). By order, we mean here the order of Taylor expansion of the mean and covariance around the true values.

As we shall see, in collision avoidance we are usually allowed to neglect the velocity uncertainty while retaining the position one. This means that out of the 6 dimensions of the state vector $\boldsymbol{x}_0$ only 3 components are uncertain.
In such case, one shall apply Eqs. 2.2 and 2.3 only to the position subset of the state vector, and treat the velocity components as deterministic, i.e. keeping the same initial velocity value for every initial position sigma-point.

2.4.4 Use of covariance

Suppose we have propagated uncertainties and we are given one covariance for the target ${}^{\mathfrak{t}}\boldsymbol{C}$ and one for the chaser ${}^{\mathfrak{c}}\boldsymbol{C}$ which can be regarded as independent.

Remark 2.3. Independence is in general not strictly true in orbital dynamics, in fact, significant correlation may be introduced by atmospheric drag. The ratio being that spacecraft undergoes similar atmospheric conditions because is depending on the same Sun activity (Matney et al., 2004). △

Covariance matrices are usually given in the R-T-N frame of the respective objects, e.g. ${}^{\mathfrak{t}}\boldsymbol{C}_{\mathfrak{t}}$ and ${}^{\mathfrak{c}}\boldsymbol{C}_{\mathfrak{c}}$, so that a rotation is needed to sum them.
Using rotation matrix defined in Section 2.1, it is possible to write the chaser's covariance ${}^{\mathfrak{c}}\boldsymbol{C}_{\mathfrak{c}}$ into its R-T-N frame by ${}^{\mathfrak{c}}\boldsymbol{C}_{\mathfrak{t}} = \boldsymbol{R}_{\mathfrak{t}}^{\mathfrak{c}\,T}\,{}^{\mathfrak{c}}\boldsymbol{C}_{\mathfrak{c}}\boldsymbol{R}_{\mathfrak{t}}^{\mathfrak{c}}$. Then, the combined covariance can be written as $\boldsymbol{C}_{\mathfrak{t}} = {}^{\mathfrak{t}}\boldsymbol{C}_{\mathfrak{t}} + {}^{\mathfrak{c}}\boldsymbol{C}_{\mathfrak{t}}$.

As we shall see in the following, the combined covariance is usually written in the b-plane, i.e. projected. To do so, the passive rotation matrix $\boldsymbol{R}_{\mathfrak{t}}^{\mathfrak{e}}$ is used to bring the covarince matrix written into the encounter frame of reference.
Then, the projection is obtained cancelling the third row and column of the matrix to obtain $\boldsymbol{C}_{\mathfrak{b}}$, i.e.

$$\boldsymbol{C}_{\mathfrak{b}} = \boldsymbol{R}_{\mathfrak{t}}^{\mathfrak{b}}\boldsymbol{C}_{\mathfrak{t}}\boldsymbol{R}_{\mathfrak{t}}^{\mathfrak{b}\,T},$$

where:

$$\boldsymbol{R}_{\mathfrak{t}}^{\mathfrak{b}} = \begin{bmatrix} 1 & 0 & 0 \\ 0 & 1 & 0 \end{bmatrix} \boldsymbol{R}_{\mathfrak{t}}^{\mathfrak{e}}$$

2.5 Collision metrics

The most common collision metrics are probability of collision and Mahalanobis distance (Hejduk, 2019). In this section, we shall examine in details only the former, since it will be the one used in the rest of the work.
They together, represent the roots of state-of-the-art, in the sense that many variants of them are proposed in the literature using correction systems or combination of these with other quantities. None of these hybrid metrics will be however examined in this dissertation because out of scope.

2.5.1 Mahalanobis distance

The Mahalanobis distance is commonly defined as the Cartesian distance between two objects scaled with the inverse positional covariance. Computation of this metric is straightforward and efficient for gaussian random variables. It is usually used as conservative detection metric.
Problem arises in generalizing it for non-gaussian distribution, however one interesting possibility is given by Poore et al. (2016).

2.5.2 Probability of collision

Probability of collision, commonly intended as non-survival probability, is a probabilistic measure of the event that two colliding objects are found at a distance so that their physical volumes interfere (given a time window of interest). Calling *Hard Body Radius* (HBR) the collision distance, the formal definition of collision event is the following (Coppola, 2012).

Definition 2.4. *Let t_0 be some initial time of interest, $R_{hbr} > 0$ the HBR and t_f a maximum time of interest. Two objects (target and chaser) are said to collide in the time of interest $[t_0, t_f]$ if*

$$\exists t \in [t_0, t_f] \quad \text{such that} \quad \|\boldsymbol{\rho}(t)\| \leq R_{hbr}$$

This definition is substantially different from the one used to compute the *instantaneous* probability of collision which is merely the probability of two spacecraft to be located within collision distance at a specific time. A hint to the formal use of Definition 2.4 can be given as follows.
Call $\boldsymbol{\mathcal{S}}_0 = [\boldsymbol{r}_0, \boldsymbol{v}_0, \boldsymbol{\rho}_0, \boldsymbol{\nu}_0]^T$ the augmented spacecraft state at the initial time t_0, where $\boldsymbol{r}_0$ and $\boldsymbol{v}_0$ are the initial position and velocity of the target in the ECI frame. Call moreover $\mathcal{P}_0(\boldsymbol{\mathcal{S}}_0, t_0)$ the generic Probability Density Function (PDF) at that instant.
The 12-dimensional state fully describes the configuration of the objects and it is defined on a 12-dimensional space that here is called $\{\boldsymbol{\mathcal{S}}_0\}$-set. Physically this set is a double copy of the same 6-dimensional space (one for the target and one for the chaser's relative position).
Then, the probability of collision is the integral of $\mathcal{P}_0$ on a hyper-volume V such

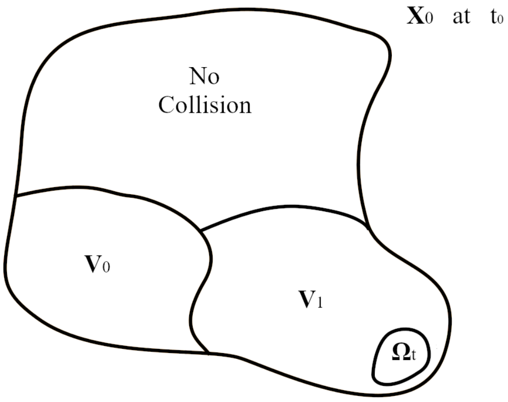

Figure 2.2: Illustration scheme of the 12-dimensional $\boldsymbol{\mathcal{S}}_0$ set partition for PDF integration in Coppola's formalism for Pc

that the collision definition above is fulfilled, mathematically:

$$P_c = \int_{\mathsf{V}} \mathcal{P}_0(\boldsymbol{\mathcal{S}}_0, t_0) d\boldsymbol{\mathcal{S}}_0 \tag{2.4}$$

Figure 2.2 provide a graphical attempt to visualize the integration set $\mathsf{V} = \mathsf{V}_0 \bigcup \mathsf{V}_1$. V_0 is the hyper-volume of initial states that collides at t_0, whereas V_1 is the hypervolume of the initial states that will collide in the time window $(t_0, t_f]$. Notice that to obtain the *instantaneous* probability of collision, for instance at t_0, one would integrate just on V_0.

The 12-dimensional integral in Eq. 2.4 is cumbersome to solve, however there are methods using heuristic hypothesis and simplifications that approximate the value. Such methods have been studied since 90's to achieve collision assessment for the ISS (Alfriend et al., 1999).

The applicability of the proposed methods varies from short-term, high velocity encounters (Patera, 2001), (Patera, 2003) (Linear and nonlinear) to long term encounters (Schaeffer et al., 2018) such as the ones in GEO orbits, e.g. encounters happening at very slow relative velocity. In the remaining part of the dissertation, we will refer to probability of collision according to Foster's method for high-velocity encounters, which is one of the most widespread approaches.

2.5.3 Foster's method

By adopting the following simplifying assumptions, the so-called Foster's integral is valid (Chan, 2008) for estimating Pc:

1. The two objects are spherical, with radii summing to R_{hbr}
2. The encounter is of the type *short-term*, meaning that
    - the relative motion can be consider linear
    - the uncertainty distribution is constant during the encounter
    - the target's ECI position (assumed as reference for the encounter frame) is essentially constant during the encounter.
3. The objects uncertainty in the velocity is negligible, i.e. velocity is deterministic
4. The position uncertainties of the objects are Gaussian and independent with mean ${}^{i}\boldsymbol{\mu}$ and covariance ${}^{i}\boldsymbol{C}$ (with $i = \mathfrak{t}, \mathfrak{c}$).

Using these heuristic assumptions, the Foster's method reduces the PDF integral in Eq. 2.4 from a 12-dimensional problem into a 3-dimensional problem and further into a bi-dimensional problem (the b-plane defined earlier) involving relative position, mean relative position and combined covarinace only, i.e. $\boldsymbol{\rho}$, $\boldsymbol{\mu}$ and $\boldsymbol{C}$.

Remark 2.4. Using the second and the third hypothesis above, the PDF can be though as the 3-dimensional distribution of the relative position centered at the mean relative position and solidal to it, while the encounter is evolving. Whereas V is a sphere centered in the origin. △

To state the formal expression for Pc with an intuitive justification, let us consider the encounter coordinate system where $\hat{\mathrm{z}}$ is the axis along the relative motion direction, i.e. $-\boldsymbol{\nu}$, and $\hat{\mathrm{x}}$, $\hat{\mathrm{y}}$ are axis in the b-plane. Using the reciprocal principle, we can swap the view in Remark 2.4 and imagine V_0 at the relative position and moving on a straight line along z-axis, while the PDF $\mathcal{P}_0$ is centered

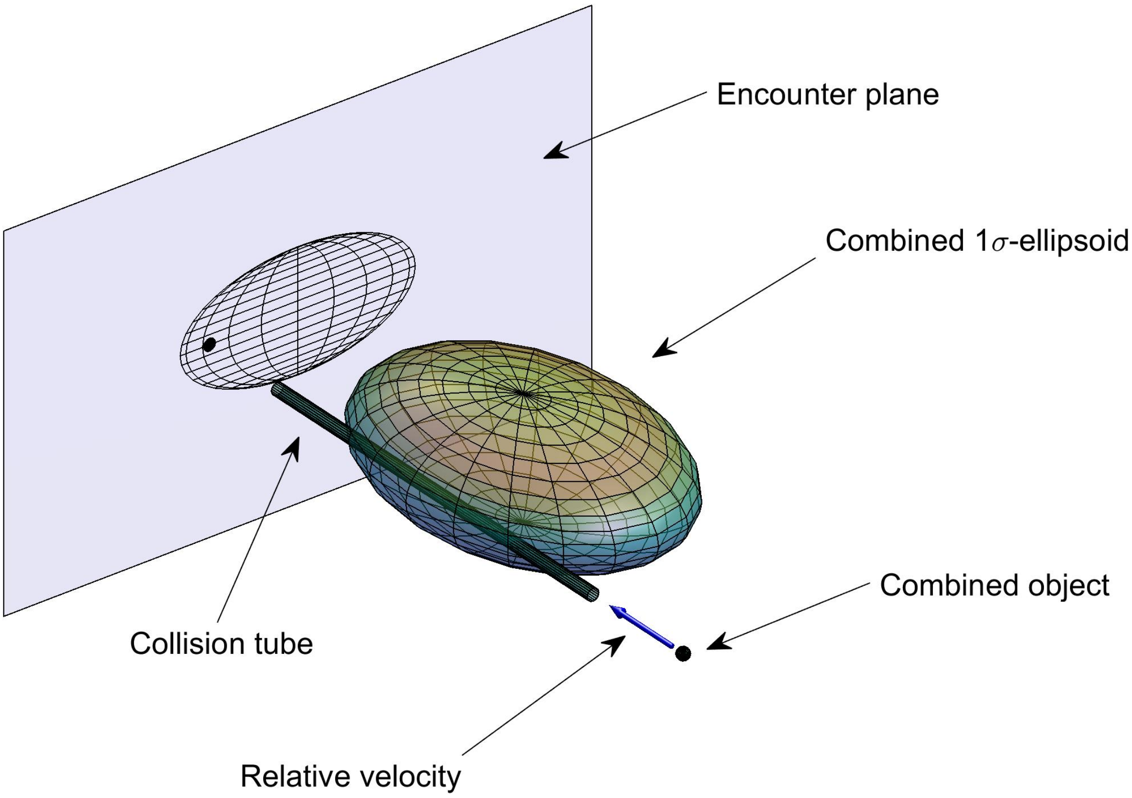

Figure 2.3: Illustration of the volume swapped by the hard-body radius going trough the covariance ellipsoid in the relative coordinate frame and their projection on the encounter plane (translated from the origin for illustration purposes).

on the origin and steady.

It is easy to imagine that the volume V_0 is spanning a cylinder along the relative trajectory and parallel to the z axis (see Figure 2.3). Considering an arbitrarily large time window of interest, the cylinder is arbitrarily long and the integration on such volume is effectively a marginalization of the PDF (assumed Gaussian).

This intuitively justifies the projection mechanism anticipated heuristically by Foster, yielding the integration on the 2-dimensional b-plane. Mathematically:

$$Pc = \frac{1}{(2\pi)\sqrt{|\boldsymbol{C}_{\mathfrak{b}}|}} \int_{-\sqrt{R_{hbr}^2 - x^2}}^{-\sqrt{R_{hbr}^2 - x^2}} \int_{-R_{hbr}}^{R_{hbr}} e^{\frac{1}{2}(\boldsymbol{\rho}_{\mathfrak{b}} - \boldsymbol{\mu}_{\mathfrak{b}})^T \boldsymbol{C}_{\mathfrak{b}}^{-1} (\boldsymbol{\rho}_{\mathfrak{b}} - \boldsymbol{\mu}_{\mathfrak{b}})} dx\, dy, \tag{2.5}$$

where the b subscripts means the projection on the b-plane of respectively: $\boldsymbol{\rho}$ the relative position, $\boldsymbol{\mu}$ the mean relative position and $\boldsymbol{C}$ the combined covariance.

2.5.4 Collision detection

Once the collision metric is available, there must be a mean to take a decision whether to maneuver or not. To this end, mainly three approaches have been found in the literature:

- Probability of collision threshold
- Maneuver as a detection problem (probability ratios)
- Distance threshold (Mahalanobis)

The first approach is the straightest and consist of placing a collision probability threshold, above which the satellite is maneuvered. The Pc threshold is usually around 1e-4 but depends on a compromise between what is the achievable global risk reduction and the desired rate of maneuvering (see current ESA's policy in Merz et al. (2017)). However, doubts on the correct use of Pc in this sense are arisen by Carpenter et al. (2017).
Another major problem of using Pc as collision metric is its inherent *False Confidence* (Balch et al., 2019).
False confidence is the phenomenon by which a decrease in the quality of measurements causes a decrease in the Pc metric. This makes the operator feel more confident that the collision is not going to happen, but this is false because the actual trajectory (so the future minimum distance) is always the same. Its just the measurement system providing bad quality data which shall be therefore not trusted. Practically this occurs when the covariance is too large with respect to the closest distance (Hejduk, 2019).

The second alternative is to take a decision formulating the problem as a detection problem, so that performances are enforced directly on the false-alarm and miss-detection. The Wald Sequential Probability Ratio Test (WSPRT) appears to be the most suitable to the problem (Carpenter et al., 2012). In this approach, probability of collision does not enter directly in the decision, instead its observables with uncertainty does, e.g. relative position and covariance.

The last, widely used, alternative consists of putting a threshold on the minimum distance. The threshold can be set on the physical distance but it is typically used on the Mahalanobis distance.

This method is usually adopted in the preliminary detection phase only as it is very conservative (Hejduk, 2019).

Automating collision detection to face the increasing workload due to upcoming constellations is a very challenging task. The sensitive point is to do that in a safe manner whiteout human supervision.
In light of the considerations of Carpenter et al. (2017), false confidence is for instance a major problem for the widely used probability of collision, making collision detection the ”art” of mixing classical indicators to avoid miss-detections and false alarms, (Balch, 2016) and (Carpenter and Markley, 2014) are examples. Although using the Mahalanobis distance metric would not be affected by false confidence (Balch et al., 2019), it would lead to an unacceptable rate of maneuvers (Hejduk, 2019).

A very promising and straightforward technique seems to be Machine Learning or AI in general (Sanchez et al., 2019), (Fernández-Mellado and Vasile, 2021), (Pinto et al., 2020). One of the fundamental problems to be faced is that ML architectures are typically “black box” once trained. This means that the agent will take a decision based on its training, but with no indication on how much the inference on the input was consistent with the training. Such a drawback was effectively circumvented by (Fernández-Mellado and Vasile, 2021) combining Dempster-Shafer theory of evidence with ML trained on a synthetic data set. The evidential approach confers transparency to the classification while ML is increasing the classification efficiency. In support to the applicability of such theory, a work by Denoeux (2019) shows that for classification tasks, Dempster-Shafer theory (or in general evidential classifiers) may help to make ML “self-explainable” in general.

2.6 Avoidance maneuver design

Once a threat is identified, the maneuver planning task tries to make the optimal evasive maneuver. Optimality can be interpreted in different ways, most straight-forward being minimum fuel cost or minimum impact on satellite operations.
The path planning problem has been considered for instance by Gremyachikh et al. (2020) and Richardson-Little et al. (2019). The former performs an integra-

tion of multi-objective optimization making use of reinforcement learning (AI). It trains an agent with a reward function based on optimality parameters such as fuel cost, collision probability threshold, maneuver restrictions, etc. The latter instead, designs a similar optimization tool without using AI. The tool is a multi-purpose optimizer that given a collision event and maneuver constraints, offers a series of optimal alternative maneuvers that the operator has to choose from.

The work of Chen et al. (2019) rather optimizes the maneuver to have the *maximum collision probability* below a given threshold.

Another example is the work from Bombardelli and Hernando-Ayuso (2014) where the optimization problem of minimizing the collision probability and impulsive maneuver cost is formulated and solved analytically. It uses the Keplerian dynamics and Gaussian assumptions to find out that if the maneuver is performed more than 1 orbit in advance, minimizing the collision probability tend to be equivalent to maximizing the miss-distance.

Uncertain maneuvering may have an effect on the overall position uncertainty which is also worth to be analyzed. In fact, the effectiveness of the maneuver to lower the probability depends on the position uncertainty after the maneuver. Zhang and Geng (2018) for example, address this problem finding an optimal thrust direction for an uncertain thrust direction. The optimality criterion minimizes position uncertainty after maneuvering.

Yang et al. (2019) instead uses a hybrid propagation model (STT-GMM) to propagate uncertainty in the presence of non-ideal maneuver sequences.

3

Low thrust modelling in Collision Avoidance

There is in principle a neat advantage in using low thrust for COLA through electric propulsion, given by the higher specific impulse of those engines. Despite negligible gravity losses in fact, examining the rocket equation it is easy to conclude that the same spacecraft equipped with more efficient engine reach the same orbital energy with less fuel.
In COLA scenario however, the long-lasting maneuver acts on the propagated uncertainty (i.e. collision metrics) and the use of those engines may not give the expected mitigation effects.

We shall see in Section 3.2 that low thrust presence and thruster's uncertainties may affect non-negligibly positional uncertainty at closest approach, which in turn increases the required maneuver magnitude to achieve the same safety threshold.
To analyze this aspect, we need first of all to understand what is the allowable propagation error for COLA applications. For this reason, the first section of this chapter is dedicated to obtain an estimate of those allowable errors.

Lastly, we shall comment modelling errors in low thrust presence which have a detrimental effect similar to thruster's uncertainty. In fact, to compute or optimize low thrust COLA maneuvers, a model for trajectory propagation must be used. Such model will be used for both (average) state and state uncertainty propagation, so that each of them result affected by a modeling error. These errors impact the computed collision index and therefore the quality of the maneuver.

3.1 Trajectory propagation requirements

Most widely used approaches in collision avoidance takes as main collision index the *probability of collision* (see Section 2.5). A good propagation for COLA operations shall therefore limit the computation error of this index.

Considering that the probability of collision (P_c) is typically a very low number, it is customary to consider its base-10 logarithm (P_{lc}), ranging between -5 and -30. Within this view, we can consider a relative error on P_{lc} defined as:

$$\delta P_{lc} = \left| \frac{P_{lc}^{*} - P_{lc}}{P_{lc}} \right|$$

We assume, as it is typically done in COLA (Chan, 2008), that the hypotheses to apply the Foster's integral are fulfilled (see Section 2.5.3). Using Foster's method, once the problem is formulated in the b-plane, P_c error arises from two possible sources: a positional error or a positional covariance error.

In the following, we obtain approximate bounds on such quantities starting from a desired maximum error on P_{lc}, i.e. $\delta \breve{P}_{lc}$.

In a quest for an analytical treatment, we approximate the Foster's integral using the PDF central value only:

$$P_c = \frac{\pi R_{hbr}^2}{2\pi\sqrt{|\boldsymbol{C}_\mathfrak{b}|}} e^{-\frac{\boldsymbol{\rho}_\mathfrak{b}^T \boldsymbol{C}_\mathfrak{b}^{-1} \boldsymbol{\rho}_\mathfrak{b}}{2}},$$

where $\boldsymbol{\rho}_\mathfrak{b}$ is the position of the secondary object in the b-plane, and $\boldsymbol{C}_\mathfrak{b}$ the projection on the b-plane of the combined covariance matrix (positional covariance only).

3.1.1 Position error requirements

Consider the encounter in the 2-dimensional b-plane with a perfect knowledge of the covariance matrix, whereas position is affected by error. Let us assume that the position error on $\boldsymbol{\rho}_{\mathfrak{b}}$ is small with respect to its norm $\|\delta\boldsymbol{\rho}_{\mathfrak{b}}\|/\|\boldsymbol{\rho}_{\mathfrak{b}}\| << 1$ and that the Probability of Collision is nearby its maximum value i.e. $\frac{\boldsymbol{\rho}_{\mathfrak{b}}^T \boldsymbol{C}_{\mathfrak{b}}^{-1} \boldsymbol{\rho}_{\mathfrak{b}}}{2} \approx 1$ (Alfriend et al., 1999). Notice also that both $\boldsymbol{\rho}_{\mathfrak{b}}$ and $\delta\boldsymbol{\rho}_{\mathfrak{b}}$ are 2-dimensional vectors with one (the same) null component, thanks to the encounter frame definition. We can use taylor expansion around the true P_c to obtain the erroneous P_c^*:

$$P_c^* = P_c - \frac{\pi R_{hbr}^2}{2\pi\sqrt{|\boldsymbol{C}_{\mathfrak{b}}|}} e^{-\frac{\boldsymbol{\rho}_{\mathfrak{b}}^T \boldsymbol{C}_{\mathfrak{b}}^{-1} \boldsymbol{\rho}_{\mathfrak{b}}}{2}} (\boldsymbol{C}_{\mathfrak{b}}^{-1}\boldsymbol{\rho}_{\mathfrak{b}})^T \delta\boldsymbol{\rho}_{\mathfrak{b}} = P_c(1 - \boldsymbol{\rho}_{\mathfrak{b}}^T \boldsymbol{C}_{\mathfrak{b}}^{-1} \delta\boldsymbol{\rho}_{\mathfrak{b}})$$

Then we have:

$$\delta P_{lc} = \left| \frac{\log(1 - \boldsymbol{\rho}_{\mathfrak{b}}^T \boldsymbol{C}_{\mathfrak{b}}^{-1} \delta\boldsymbol{\rho}_{\mathfrak{b}})}{P_{lc}} \right|$$

Explicitly noticing that the two assumptions above implies $\|\boldsymbol{\rho}_{\mathfrak{b}}^T \boldsymbol{C}_{\mathfrak{b}}^{-1} \delta\boldsymbol{\rho}_{\mathfrak{b}}\| << 2$, then we can further expand the logarithm function around 1 obtaining:

$$\delta P_{lc} = \frac{|\boldsymbol{\rho}_{\mathfrak{b}}^T \boldsymbol{C}_{\mathfrak{b}}^{-1} \delta\boldsymbol{\rho}_{\mathfrak{b}}|}{P_{lc}}$$

Let now $\delta\breve{P}_{lc}$ be the desired upper bound of the probability error, we have that the limit $\delta\boldsymbol{\rho}_{\mathfrak{b}}$ shall fulfill:

$$|\boldsymbol{\rho}_{\mathfrak{b}}^T \boldsymbol{C}_{\mathfrak{b}}^{-1} \delta\boldsymbol{\rho}_{\mathfrak{b}}| = P_{lc}\delta\breve{P}_{lc}$$

Using the sub-multiplicative property of the matrix norm we finally have the $\delta\boldsymbol{\rho}_{\mathfrak{b}}$ bound:

$$\|\delta\boldsymbol{\rho}_{\mathfrak{b}}\| \leq \frac{P_{lc}\delta\breve{P}_{lc}}{\|\boldsymbol{\rho}_{\mathfrak{b}}^T \boldsymbol{C}_{\mathfrak{b}}^{-1}\|} \tag{3.1}$$

Notice that the obtained threshold for $\delta\boldsymbol{\rho}_{\mathfrak{b}}$ is problem dependent. This means that fixing a desired maximum error on the probability of collision, the allowed position error depends on the encounter geometry (through $\boldsymbol{\rho}_{\mathfrak{b}}$ and $\boldsymbol{C}_{\mathfrak{b}}$).

The above derivation was performed implicitly considering positional errors in the b-plane only. If one wishes to account for position errors in the full Cartesian space $\|\delta\boldsymbol{\rho}_{\mathfrak{t}}\|$ as well as a velocity error $\delta\boldsymbol{\nu}_{\mathfrak{t}}$, the main effect is that the b-plane itself now differs from the true one. However, it is easy to prove (see Chapter Appendix) that at first order $\|\delta\boldsymbol{\rho}_\mathfrak{b}\| \leq \|\delta\boldsymbol{\rho}_\mathfrak{t}\|$. Therefore, if one wishes to use Eq. 3.1 as requirement, a natural extension for the bound computed above holds, meaning that one can replace $\|\delta\boldsymbol{\rho}_\mathfrak{b}\|$ with $\|\delta\boldsymbol{\rho}_\mathfrak{t}\|$ producing a conservative requirement estimate.

3.1.2 Covariance error requirements

Consider again the encounter in the 2-dimensional b-plane. Let us now address the problem of a small error affecting the covariance while knowing exactly the positions, that is:

$$\boldsymbol{C}_\mathfrak{b}^* = \boldsymbol{C}_\mathfrak{b} + \delta\boldsymbol{C}_\mathfrak{b} \quad with \quad \|\boldsymbol{C}_\mathfrak{b}^{-1}\delta\boldsymbol{C}_\mathfrak{b}\| \leq \|\boldsymbol{C}_\mathfrak{b}^{-1}\|\|\delta\boldsymbol{C}_\mathfrak{b}\| << 1$$

Additionally, suppose again that the probability of collision is nearby its maximum value i.e. $\frac{\boldsymbol{\rho}_\mathfrak{b}^T\boldsymbol{C}_\mathfrak{b}^{-1}\boldsymbol{\rho}_\mathfrak{b}}{2} \approx 1$ (Alfriend et al., 1999). We start rewriting the probability of collision as:

$$P_c = \frac{R_{hbr}^2}{2}\sqrt{|\boldsymbol{C}_\mathfrak{b}^{-1}|}e^{-\frac{\boldsymbol{\rho}_\mathfrak{b}^T\boldsymbol{C}_\mathfrak{b}^{-1}\boldsymbol{\rho}_\mathfrak{b}}{2}}$$

Then like the positional error case, we adopt a linearization of P_c^* around the true probability P_c. So, we need to compute the gradient of P_c with respect to the matrix $\boldsymbol{C}_\mathfrak{b}^{-1}$, which results to be:

$$\frac{\partial P_c}{\partial \boldsymbol{C}_\mathfrak{b}^{-1}} = \frac{R_{hbr}^2}{2}\left[\frac{\sqrt{|\boldsymbol{C}_\mathfrak{b}^{-1}|}}{2}\boldsymbol{C}_\mathfrak{b}^T e^{-\frac{\boldsymbol{\rho}_\mathfrak{b}^T\boldsymbol{C}_\mathfrak{b}^{-1}\boldsymbol{\rho}_\mathfrak{b}}{2}} - \sqrt{|\boldsymbol{C}_\mathfrak{b}^{-1}|}2e^{-\frac{\boldsymbol{\rho}_\mathfrak{b}^T\boldsymbol{C}_\mathfrak{b}^{-1}\boldsymbol{\rho}_\mathfrak{b}}{2}}\boldsymbol{\rho}_\mathfrak{b}\boldsymbol{\rho}_\mathfrak{b}^T\right],$$

where we have used the differential identities:

$$\frac{\partial|\boldsymbol{C}_\mathfrak{b}^{-1}|}{\partial \boldsymbol{C}_\mathfrak{b}^{-1}} = |\boldsymbol{C}_\mathfrak{b}^{-1}|\boldsymbol{C}_\mathfrak{b}^T \quad and \quad \frac{\boldsymbol{\rho}_\mathfrak{b}^T\boldsymbol{C}_\mathfrak{b}^{-1}\boldsymbol{\rho}_\mathfrak{b}}{\partial \boldsymbol{C}_\mathfrak{b}^{-1}} = \boldsymbol{\rho}_\mathfrak{b}\boldsymbol{\rho}_\mathfrak{b}^T$$

The above expression simplifies when plugged into the linear expansion of P_c^* to obtain:

$$P_c^* = P_c\left(1 - \frac{1}{2}tr\left((-\boldsymbol{C}_\mathfrak{b} + \boldsymbol{\rho}_\mathfrak{b}\boldsymbol{\rho}_\mathfrak{b}^T)\delta\boldsymbol{C}_\mathfrak{b}^{-1}\right)\right) \tag{3.2}$$

Remark 3.1. Notice that i) this expansion holds in force of the starting hypotheses because we can write $\|(-\boldsymbol{C}_\mathfrak{b} + \boldsymbol{\rho}_\mathfrak{b}\boldsymbol{\rho}_\mathfrak{b}^T)\delta\boldsymbol{C}_\mathfrak{b}^{-1}\| << 1$, this will be shown shortly; ii) we have used the symmetry of $\boldsymbol{C}_\mathfrak{b}$ to replace $\boldsymbol{C}_\mathfrak{b}^T$ △

It is now possible to notice that the expansion is function of the small error $\delta \boldsymbol{C}_{\mathfrak{b}}^{-1}$ whereas we would it to be a function of $\delta \boldsymbol{C}_{\mathfrak{b}}$. To this aim, consider the first order Neumann expansion of $\boldsymbol{C}_{\mathfrak{b}}^{*-1}$ in force of $\|\boldsymbol{C}_{\mathfrak{b}}^{-1}\delta \boldsymbol{C}_{\mathfrak{b}}\| << 1$ so that we can write:

$$\delta \boldsymbol{C}_{\mathfrak{b}}^{-1} = (\boldsymbol{C}_{\mathfrak{b}} + \delta \boldsymbol{C}_{\mathfrak{b}})^{-1} - \boldsymbol{C}_{\mathfrak{b}}^{-1} = -\boldsymbol{C}_{\mathfrak{b}}^{-1}\delta \boldsymbol{C}_{\mathfrak{b}}\boldsymbol{C}_{\mathfrak{b}}^{-1}$$

Remark 3.2. The starting Taylor expansion used for Eq. 3.2 is valid for $\|\delta \boldsymbol{C}_{\mathfrak{b}}^{-1}\|/\|\boldsymbol{C}_{\mathfrak{b}}^{-1}\| << 1$. Thanks to the above Neumann expansion we have $\|\boldsymbol{C}_{\mathfrak{b}}^{-1}\delta \boldsymbol{C}_{\mathfrak{b}}\boldsymbol{C}_{\mathfrak{b}}^{-1}\|/\|\boldsymbol{C}_{\mathfrak{b}}^{-1}\| \leq \|\boldsymbol{C}_{\mathfrak{b}}^{-1}\delta \boldsymbol{C}_{\mathfrak{b}}\| << 1$, which agrees with the original hypothesis. △

Substituting into the P_c^* expression, and using the cyclic property of the trace of product, one has:

$$P_c^* = P_c\left(1 + \frac{1}{2}tr\left((-\boldsymbol{C}_{\mathfrak{b}}^{-1} + \boldsymbol{C}_{\mathfrak{b}}^{-1}\boldsymbol{\rho}_{\mathfrak{b}}\boldsymbol{\rho}_{\mathfrak{b}}^T\boldsymbol{C}_{\mathfrak{b}}^{-1})\delta \boldsymbol{C}_{\mathfrak{b}}\right)\right) \tag{3.3}$$

We are now in the position of showing that the Taylor expansion holds and further obtain an expression for the log-probability error. Consider that:

$$\|(-\boldsymbol{C}_{\mathfrak{b}} + \boldsymbol{\rho}_{\mathfrak{b}}\boldsymbol{\rho}_{\mathfrak{b}}^T)\delta \boldsymbol{C}_{\mathfrak{b}}^{-1}\| \approx \|(-\boldsymbol{C}_{\mathfrak{b}}^{-1} + \boldsymbol{C}_{\mathfrak{b}}^{-1}\boldsymbol{\rho}_{\mathfrak{b}}\boldsymbol{\rho}_{\mathfrak{b}}^T\boldsymbol{C}_{\mathfrak{b}}^{-1})\delta \boldsymbol{C}_{\mathfrak{b}}\|$$

Then using the matrix square root decomposition $\boldsymbol{C}_{\mathfrak{b}}^{-1} = \boldsymbol{C}_{\mathfrak{b}}^{-1/2}\boldsymbol{C}_{\mathfrak{b}}^{-1/2}$, the left hand side is up-bounded by:

$$\|\boldsymbol{C}_{\mathfrak{b}}^{-1}\delta \boldsymbol{C}_{\mathfrak{b}}\| + \|\boldsymbol{C}_{\mathfrak{b}}^{-1/2}\|\|\boldsymbol{C}_{\mathfrak{b}}^{-1/2}\boldsymbol{\rho}_{\mathfrak{b}}\|^2\|\boldsymbol{C}_{\mathfrak{b}}^{-1/2}\|\|\delta \boldsymbol{C}_{\mathfrak{b}}\| << 1$$

where the inequality holds thanks to the starting assumptions: $\|\boldsymbol{C}_{\mathfrak{b}}^{-1}\delta \boldsymbol{C}_{\mathfrak{b}}\| \leq \|\boldsymbol{C}_{\mathfrak{b}}^{-1}\|\|\delta \boldsymbol{C}_{\mathfrak{b}}\| << 1$ and $\frac{\boldsymbol{\rho}_{\mathfrak{b}}^T\boldsymbol{C}_{\mathfrak{b}}^{-1}\boldsymbol{\rho}_{\mathfrak{b}}}{2} \approx 1$. This also implies we can linearize the logarithm of Eq. 3.3 around 1 and obtain:

$$\delta P_{lc} = \frac{1}{2P_{lc}}\left|tr\left(\left(-\boldsymbol{C}_{\mathfrak{b}}^{-1} + \boldsymbol{C}_{\mathfrak{b}}^{-1}\boldsymbol{\rho}_{\mathfrak{b}}\boldsymbol{\rho}_{\mathfrak{b}}^T\boldsymbol{C}_{\mathfrak{b}}^{-1}\right)\delta \boldsymbol{C}_{\mathfrak{b}}\right)\right|$$

Using now the property of the trace of product in term of vectorized matrices $tr(A^TB) = vec(A)^Tvec(B)$ one can write

$$|vec(-\boldsymbol{C}_{\mathfrak{b}}^{-1} + \boldsymbol{C}_{\mathfrak{b}}^{-1}\boldsymbol{\rho}_{\mathfrak{b}}\boldsymbol{\rho}_{\mathfrak{b}}^T\boldsymbol{C}_{\mathfrak{b}}^{-1})^Tvec(\delta \boldsymbol{C}_{\mathfrak{b}})| = 2P_{lc}\delta P_{lc}$$

Let $\delta\breve{P}_{lc}$ be the desired upper bound of the probability error and use the sub-multiplicative property of the matrix norm, one obtains:

$$\|vec(\delta\boldsymbol{C}_{\mathfrak{b}})\| \leq \frac{2P_{lc}\delta P_{lc}}{\|vec(-\boldsymbol{C}_{\mathfrak{b}}^{-1}+\boldsymbol{C}_{\mathfrak{b}}^{-1}\boldsymbol{\rho}_{\mathfrak{b}}\boldsymbol{\rho}_{\mathfrak{b}}^{T}\boldsymbol{C}_{\mathfrak{b}}^{-1})^{T}\|} \tag{3.4}$$

Or, in terms of Frobenious norm of matrices:

$$\|\delta\boldsymbol{C}_{\mathfrak{b}}\|_F \leq \frac{2P_{lc}\delta P_{lc}}{\|\boldsymbol{C}_{\mathfrak{b}}^{-1}(-I+\boldsymbol{\rho}_{\mathfrak{b}}\boldsymbol{\rho}_{\mathfrak{b}}^{T}\boldsymbol{C}_{\mathfrak{b}}^{-1})\|_F}$$

Again similarly to the position error threshold, the obtained bound is problem dependent.

Furthermore, also in this case, we have to generalize the bound on the projected matrix $\boldsymbol{C}_{\mathfrak{b}}$ to the general 3D covariance matrix $\boldsymbol{C}$. This time however, as we were supposing the position to be exact, the b-plane coincides with the true one, which makes the derivation straightforward:

$$\delta\boldsymbol{C}_{\mathfrak{b}} = \boldsymbol{C}_{\mathfrak{b}}^{*} - \boldsymbol{C}_{\mathfrak{b}} = \boldsymbol{R}_{\mathfrak{b}}^{\mathfrak{t}\,T}(\boldsymbol{C}+\delta\boldsymbol{C})\boldsymbol{R}_{\mathfrak{b}}^{\mathfrak{t}} - \boldsymbol{R}_{\mathfrak{b}}^{\mathfrak{t}\,T}\boldsymbol{C}\boldsymbol{R}_{\mathfrak{b}}^{\mathfrak{t}}$$

Which, thanks to sub-multiplicative property of matrices yields $\|\boldsymbol{C}_{\mathfrak{b}}\|_F \leq \|\boldsymbol{C}\|_F$ (recall that $\boldsymbol{R}_{\mathfrak{b}}^{\mathfrak{t}}$ is 2×3). Finally, we can say that also in this case, the norm bound obtained on the b-plane can be considered a norm requirement in the 3D space.

3.1.3 Error bounds validation

Both the error bounds obtained in the previews sections hold with approximations and, more importantly, depends on the specific encounter geometry. In this section, we first validate the obtained bounds, proving that they can be considered statistically reliable, i.e. perform well on typical encounters.

Then, we try to obtain an overall positional and covariance requirements valid for most practical situations, which will be used as the main requirement for the analytic trajectory propagator discussed in the next Chapter.

To validate the bounds we need a benchmark of random encounter geometries. To this end, we profiled the collision avoidance challenge database provided by ESA (2019) fitting kernel probability distributions on:

- Relative velocity components

- Relative position components on the b-plane
- Eigenvalues of the covariance matrices (both target and chaser)
- Euler angles of the diagonalizing matrix for the covariance matrices (both target and chaser)

As a result, 17 experimental PDFs are obtained from which random independent realization can be drawn. This procedure however, loses dataset correlation, for instance between relative velocity and covariance orientation. The result is a random dataset with a higher number of low-probability events ($P_{lc} \leq -30$) with respect to the original database. Still, by discarding those events, we can obtain a statistically meaningful dataset if the remaining ones are enough.

With such a set of probability distributions, the random set of encounters are generated firstly by randomly generating 1000 LEO target orbits and relative encounter geometries from the profiled dataset. Figure 3.1 depicts the P_{lc} histogram of an example realization of such procedure where, discarding the events with log probabilities of collision $P_{lc} \leq -30$, a set of 153 random encounters is obtained.

To test the relative position norm bound, we set a desired log-probability error threshold, say $\delta \breve{P}_{lc} = 0.1$. Then, for each random encounter, we require the right-hand-side of Eq. 3.1 to be the norm of a sphere (limiting $\|\delta \boldsymbol{\rho}_{\mathrm{t}}\|$), rather than a circle (limiting $\|\delta \boldsymbol{\rho}_{\mathfrak{b}}\|$). Meaning that, when $\|\delta \boldsymbol{\rho}_{\mathrm{t}}\|$ is projected onto the b-plane Eq. 3.1 is fulfilled.

For each case, we create a grid of evaluation points on such a sphere (1250 points equally spaced in the angular positions). We can thus evaluate the actual probability of collision error (using Foster's method) when the perturbed distance at TCA lies on the obtained bounding surface. If there is any point on such a surface originating an error probability $\delta P_{lc} > \delta \breve{P}_{lc}$, we say that the bound has failed. Counting the success rate on all the random encounters gives an indication on how good Eq. 3.1 is on typical encounters.

Testing the combined covariance norm bound follows the same line, so we require the 2-dimensional covariance bound to be that of the full 3-dimensional one. Then, the further complication is that the grid points now lie on a 5D hypersphere (12000 points grid used). In fact, having fixed the Frobenious norm of a 3D covariance matrix we can consider one of its three eigenvalues constrained.

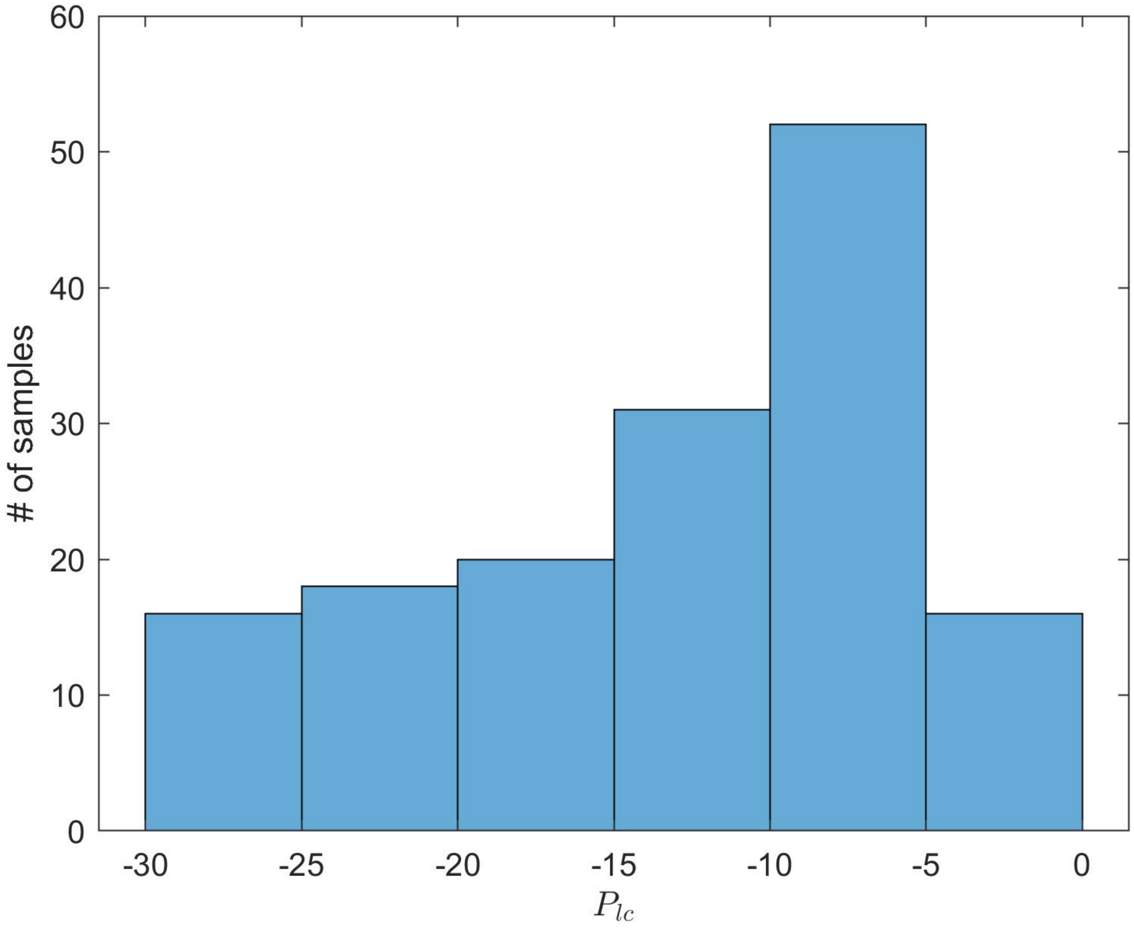

Figure 3.1: Log-probabilities of collision histogram obtained from a set of 1000 randomly generated encounters (probabilities lower than -30 where neglected, yielding 153 encounters)

We are then left with five free parameters, namely the other two eigenvalues and the three possible rotation angles for the diagonalizing (unitary) matrices.
The three eigenvalues are evenly spaced on a sphere with 12-point grid, while the rotation angles of the diagonalizing matrix are evenly spaced on a 3-dimensional cube with edge length 2π.

Let us formalize the above experiment in a statistical framework to get confidence interval on the outcome, showing that the 153 samples produce statistically significant result.
The proposed experiment is a Bernoulli process where a sequence of $N = 153$ independent trials is realized. Each trial may result in either a success (with probability p) or a failure (with probability 1-p). Then, the number of successes in this experiment is a random variable following the Binomial distribution.
We want to estimate the rate of success p with a 95% confidence interval, so that p represents reliably the probability that our statistic threshold is respected in an operative scenario.
The p-parameter of a Binomial distribution can be estimated with its maximum likelihood estimator, i.e. number of successes in the experiment divided by 153. Then, it is possible to show that a confidence interval for such estimator can be obtained approximating the number of successes distribution as a normal distribution (Brown et al., 2001). Thus for a 95% confidence interval the bounds are given by:

$$CI = \pm 1.96\sqrt{\frac{\hat{p}(1-\hat{p})}{N}},$$

with $\hat{p}$ the experimental ratio between the number of successes in the experiment and N, the number of trials.

Remark 3.3. This approximation of the CI is subjected to the requirement $Np > 5$ to be reliable. This requirement is actually met with 153 samples for the most interesting studied cases of $\delta\breve{P}_{lc}$. △

The success rates clearly depends on the log-error threshold. The larger the threshold the larger the bounds degrading the linear approximations, i.e. degrading the assumptions $\|\boldsymbol{C}_{\mathfrak{b}}^{-1}\delta\boldsymbol{C}_{\mathfrak{b}}\| << 1$ and $\|\delta\boldsymbol{\rho}_{\mathfrak{t}}\|/\|\boldsymbol{\rho}_{\mathfrak{t}}\| << 1$. Table 3.1 reports the success rates as function of the chosen $\delta\breve{P}_{lc}$. We can take those values as confidence on the obtained bound given some desired $\delta\breve{P}_{lc}$.
Then, we can heuristically conclude that the obtained bounds in Eqs. 3.1 and

Table 3.1: Success rates of the bounds in % as function of $\delta\breve{P}_{lc}$, 95% confidence interval in parenthesis.

$\delta\breve{P}_{lc}$	0.001	0.01	0.1	0.5
$\lVert\delta\boldsymbol{\rho}_{\mathrm{t}}\rVert$	$97(\pm3)$	$95(\pm3)$	$92(\pm4)$	$82(\pm6)$
$\lVert\delta\boldsymbol{C}\rVert$	$100(\pm NA)$	$98(\pm2)$	$90(\pm5)$	$82(\pm6)$

3.4 are usable as requirements for requested log-probability error thresholds $\delta\breve{P}_{lc} \leq 0.1$, i.e. 10%.

We shall now link the desired log-probability error $\delta\breve{P}_{lc}$ to some overall position and covariance error bounds, eliminating the dependency on the specific encounter of Eqs. 3.1 and 3.4. To this end, the original (not the profiled one) collision avoidance competition data set was employed.
For each event in the dataset, we took the CDMs issued at most 1 day prior to TCA (5000 CDMs). For each CDM, the position and covariance error bounds were computed for a log-probability error threshold of 10%. We then visualized the obtained bounds in a CDF-like fashion (see Figure 3.2), i.e. displaying the number of occurrences where the obtained bounds were greater than a given value.
By tracing an horizontal line at the desired percentage (say 95%, 2σ), we find the overall bound which in the 95% of real cases assures a log-probability error to be less than 10%. This follows simply from the fact that those 95% of situations would have a bound equal or larger than the overall one.

The outcome of this approach allows concluding that, for a propagation to comply with $\delta\breve{P}_{lc} = 0.1$ at 2σ or 1σ level on real scenarios, it has to provide:

- 10m (2σ) or 204m (1σ) accuracy in the relative position at TCA ($\lVert\boldsymbol{\rho}_{\mathrm{t}}\rVert$)
- 5m (2σ) or 155m (1σ) accuracy in the combined covariance at TCA ($\sqrt{\lVert\delta\boldsymbol{C}\rVert_F}$)

Notice that those are errors built up from two parts: the chaser and the target propagation. This means that, assuming their state vector have been measured at the same accuracy level and undergoes similar propagation conditions, the single satellite propagation shall fulfill half that accuracy. Meaning that that the sum of the errors (chaser and target), made either in relative position or combined covariance shall be within the bounds. If the requirements above are not fulfilled, we shall consider the propagation error significant. A remediation ac-

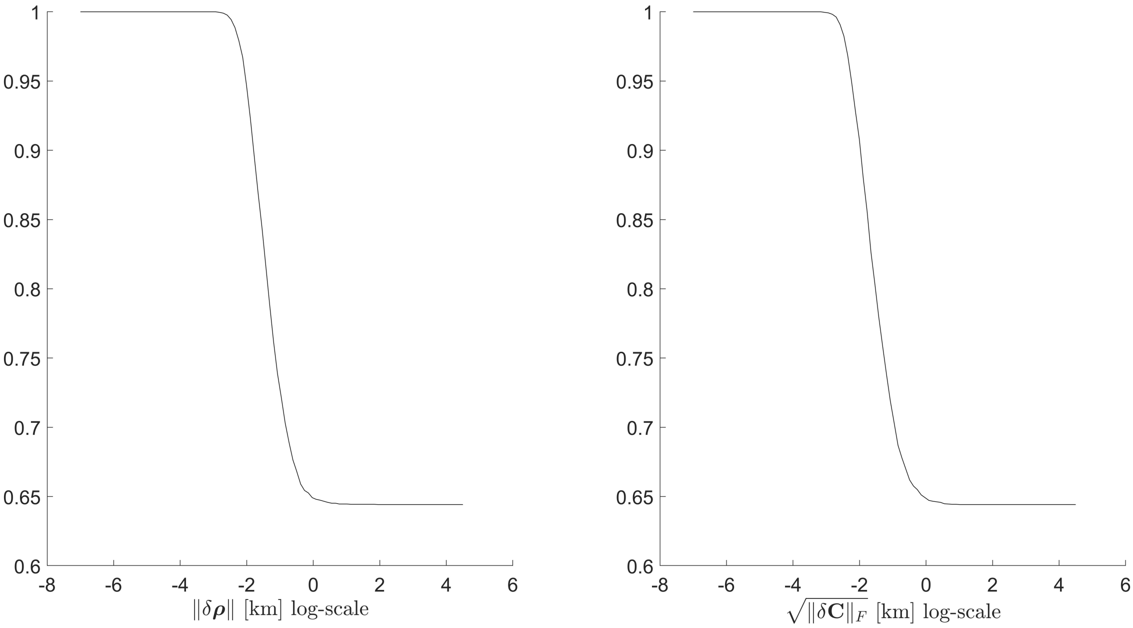

Figure 3.2: CDF of the computed thresholds for 5000 real encounters assuming $\delta\breve{P}_{lc} = 0.1$

tion would then be to properly inflate the covariance, adding to the measurement uncertainty the expected propagation uncertainty. Under the reasonable assumption that those uncertainties are independent.

3.2 Impact of low thrust maneuvers on uncertainty propagation

Low-thrust maneuvers affect the propagation of an initial state uncertainty under two aspects:

- as a result of the modified system dynamics;
- due to possible uncertainties in the thrust itself.

To highlight the relative importance between these effects, we make use of simulations on two baseline scenarios, defined in Table 3.2.
The spacecraft on such orbits, referred to as the target, is supposed to be at the pericenter at the initial time $t_0 = 0$.

Table 3.2: Benchmark orbits for the target spacecraft

case	altitude [km]	eccentricity	inclination [°]
1	713	0.001	98.2
2	1422	0.1	40

3.2.1 Low thrust presence

Examine as first case, the one where low-thrust is deterministic, i.e. there are no uncertainties on it. Consider moreover, the case where the low thrust is the only perturbing force and we use a propagation model able to exactly propagate the uncertainty, i.e. numerical model with Monte Carlo.

Being the thrust very small by assumption, one might be tempted to conclude that the initial uncertainty propagated with a keplerian model or a perturbed model are very similar. There would be therefore no need to take low thrust into account when propagating uncertainty.

To have an idea of the error committed in the latter case, a Monte Carlo simulation has been performed for the two benchmark cases of Table 3.2. To this aim, we do not need the complete conjunction scenario, we just need the maneuvering target spacecraft and its initial covariance. Therefore we assume a (typical) initial covariance matrix in local R-T-N coordinates (Vetter, 2007):

$$ {}^{\mathrm{t}}\boldsymbol{C}_{\mathrm{t}0} = \begin{bmatrix} .025^2 & 0 & 0 \\ 0 & .2^2 & 0 \\ 0 & 0 & .025^2 \end{bmatrix} [km^2] \tag{3.5} $$

We propagated some initial samples for 5 orbits under two conditions: no-thrust and 1e-7km/s^2 tangential acceleration. With a trial and error approach, an initial gaussian population of 3.5 million samples was found to provide stable results.

Results show that the standard deviations of the cartesian position slowly diverge apart (Figure 3.3), around 1% to 10% of the initial deviation prescribed in Eq. 3.5. Considering a spacecraft in orbit with case 1 and case 2 of Table 3.2, no noteworthy difference appears in the Cartesian covariance. Being the period of case 1 smaller, also the standard deviations are shrinked (roughly) proportionally.

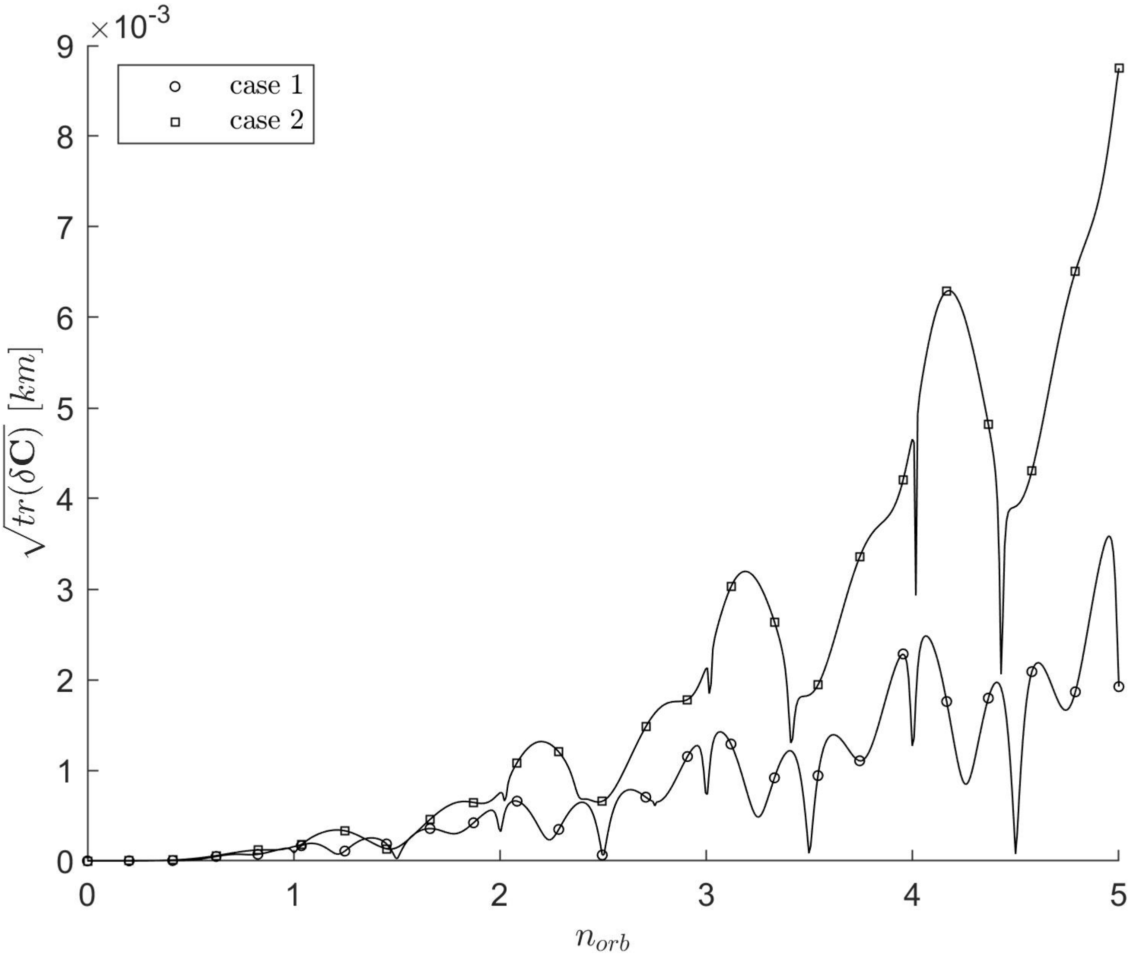

Figure 3.3: Norm of the Cartesian R-T-N difference between the covariance diagonals as a function of propagation time in reference case 2, between unperturbed and perturbed motion.

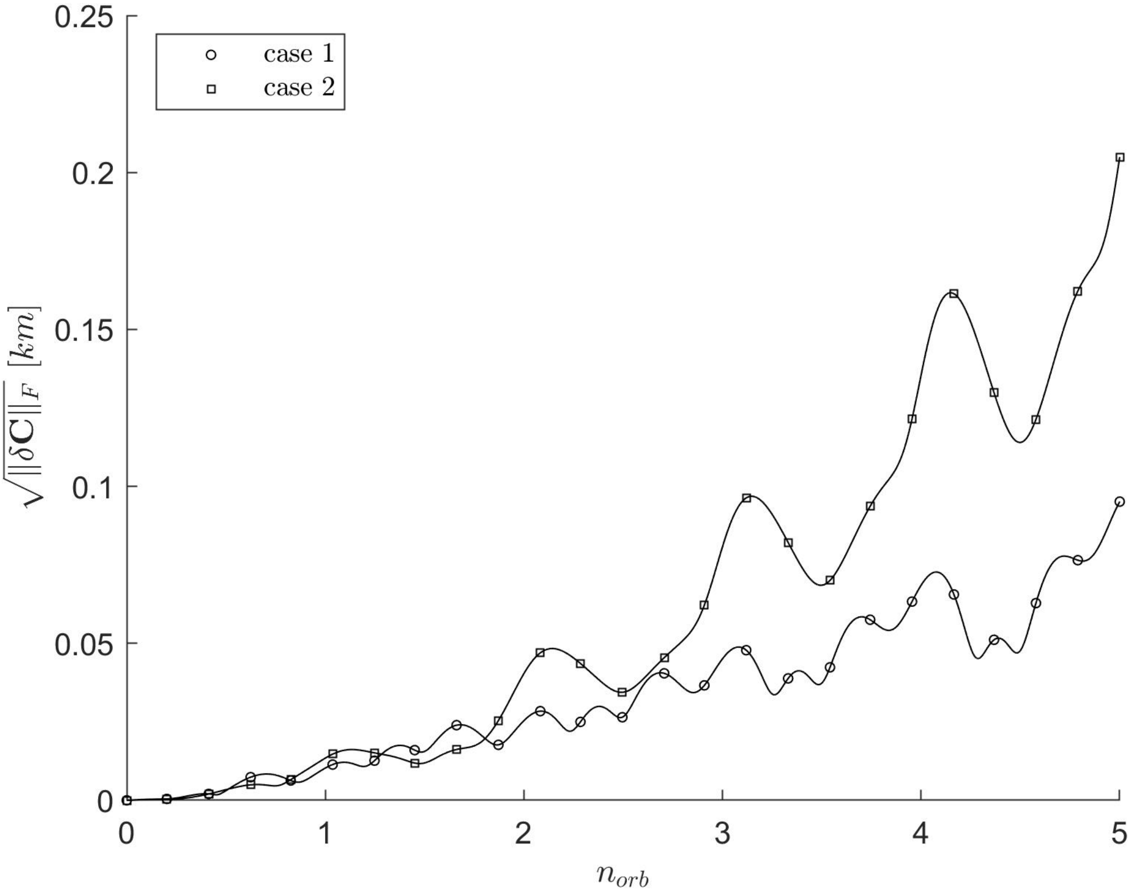

Figure 3.4: Covariance error metric as a function of propagation time in reference case 2, between covariance propagated under perturbed motion and Keplerian motion

Next, to include also the out-of-diagonal covariance matrix elements in the analysis, we report the error metric defined in Section 3.1.2 as a function of the propagation time, see Figure 3.4.

To analyse Figure 3.4, consider for simplicity, the case where the chaser's uncertainty is propagated exactly as well. Since the target's uncertainty are propagated exactly in both cases Keplerian and perturbed, the only error we can commit in the combined propagated uncertainty is in considering or not the perturbation, i.e. low thrust presence. Then, the full bound obtained in Section 3.1.3 is at disposal to depreciate the propagation error made on the target (when neglecting thrust presence). Given the bounds, from Figure 3.4 we can be confident at 1σ that the presence of the tangential perturbation in case 2 can cause a Pc error within 10% for about 4 orbital periods propagation. Much less than one orbit instead if one wants a 2σ confidence.

Although this result is restricted to benchmark cases, we can reasonably extend the conclusion saying that at 1σ, one can reasonably neglect the perturbation presence when propagating the covariance for few orbital periods. Conversely, requiring a 2σ confidence in a 10% Pc error requirement, the perturbation presence must be taken into account or the estimate of the final covariance is too rough.

3.2.2 Low thrust systems uncertainties

From the BepiColombo experience (see references Section IV.G of (Clark et al., 2019) and Section V/VI of (Castellini et al., 2020)), when applying low-thrust we have at least two uncertainties:

- An uncertainty on the stabilized value of the thrust: 0.1% - 2%
- An uncertainty on the instantaneous thrust: 0.1% - 0.2% (4 minutes averaging window)

Additionally, one can add a third uncertainty on the thrust direction given by some inaccuracies in the spacecraft attitude or manufacturing issues (Bruijn et al., 2017), however this effect is smaller than the one due to magnitude variation.

The origin of the stabilized thrust error (first in the list) is located in the difficulty of estimating the real engine performance characteristics. In fact, the onboard computer can compute only an approximation of the applied thrust, as long as a direct measure is not available.

Although one could estimate the actual thrust in post-processing by precise orbit determination from ground, the estimate would be subjected anyhow to some residual uncertainty in the order of 0.5% (Castellini et al., 2020). Although small, 0.5% uncertainty is still significant in a low-thrust scenario as explained by Bruijn et al. (2017) and expanded hereafter.

The origin of the second (random) error in the list, expressed in terms of thrust stability, is aleatory.

Remark 3.4. In the simulations below, we need a statistical representation of engine stability. Characterizing statistically the aleatory uncertainty for a low thrust engine is not an easy task. This is why errors are verified in terms of stability of the thrust, i.e. thrust remaining within some bounds when averaging for given time, see Clark et al. (2019). In Chapter Appendix an empirical method is outlined to convert the stability characteristic into a statistical one. △

Using a simple Monte Carlo simulation with cases of Table 3.2 we obtain propagation errors for both the listed uncertainties.
The idea is the following: assume a target and chaser has some expected mitigated probability of collision P_c (maneuver being performed). Assume moreover that the initial target's state vector is perfectly known while the chaser has some initial uncertainty. Then, if the target's perform a perfect avoidance maneuver, its uncertainty at mitigated TCA is null and the mitigated probability of collision would be given by the chaser's uncertainty only. If instead, the target has uncertainties on the thrust, its uncertainty at TCA is not null and, summed to the chaser's one, causes the actual mitigated probability of collision to be some $P_c^* \neq P_c$. In case engine's uncertainties are insignificant one would expect a negligible difference between P_c^* and P_c, meaning the the target's position and covariance at TCA shall be within the bounds stated in Section 3.1.3.
With this idea, the simulations considered the evolution of the target only. Using the starting condition of null initial uncertainty, some realizations are propagated varying the perturbing acceleration around a mean value of 5e-8 km/s^2 (e.g. to reflect a 300 kg S/C subjected to 0.015 N thrust). In one case adding a random realization bias to the average thrust and, in the other case, adding a white noise to the thrust. Then, we considered a 5 orbit propagation (less then 1 day) and measured how large was the final covariance.
With a trial and error process we established that respectively 10000 and 100 samples produced acceptably stable results respectively in "realization bias" and "white noise" simulations.
The outcome shows that:

- A 1% gaussian uncertainty (i.e. $5\mathrm{e}{-10} km/s^2$ standard deviation) on the stabilized value of the acceleration caused about 500 m standard deviation in the traverse direction and 1m in the radial direction for case 1, and about 900 m and 30m for case 2 respectively. Notably these values resulted to be about 1% of the cartesian position change with respect to Keplerian case (great linearity between thrust error and position difference).

- A 0.17% uncertainty (on 4 minutes averaging window), equivalent to $N_s =$

$1.32\text{e}{-9}km/s^{3/2}$, for the instantaneous acceleration caused few meters standard deviation in the traverse direction, and few centimeter in the radial direction.

Coherently with the references above, the error coming from the stabilized thrust creates errors in the order of kilometers (in the tangential direction). On the other hands, the instantaneous thrust variability still has a growing behavior but significantly smaller by orders of magnitude in the propagation period of interest. Intuitively, this is due to the fact that, with randomized thrust in time, the thrust error somehow averages out, in the thrust-biased case instead the error accumulates.

To draw conclusions about the significance of such uncertainties we take the usual Frobenious norm parameter of the final target's covariance. Similarly to Section 3.2.1, we consider the situation in which the model can perfectly propagate the trajectories and the thrust is the only perturbation, so that bounds in Section 3.1 are fully available for error depreciation.
From Figures 3.5 and 3.6, it is clear that the covariance error committed by neglecting the biased thrust is out of the allowed bounds (both 1σ or 2σ) soon after a couple of orbits, in both the test cases. It is therefore fundamental to convert the stabilized thrust into a contribution of positional uncertainty.
Stochastic uncertainty is instead well below the 1σ bound, hinting to the possibility of neglecting this contribution in short propagation.

It is finally possible to rank the low thrust effects to be accounted when performing COLA with such a system. From the largest to the smallest one has:

1. Stabilized thrust uncertainty
2. Low thrust presence
3. Random thrust uncertainty

3.3 Trajectory modelling error

Independently on whether the low thrust execution is perfect or not, when performing propagation of either average state or state uncertainty under perturbed

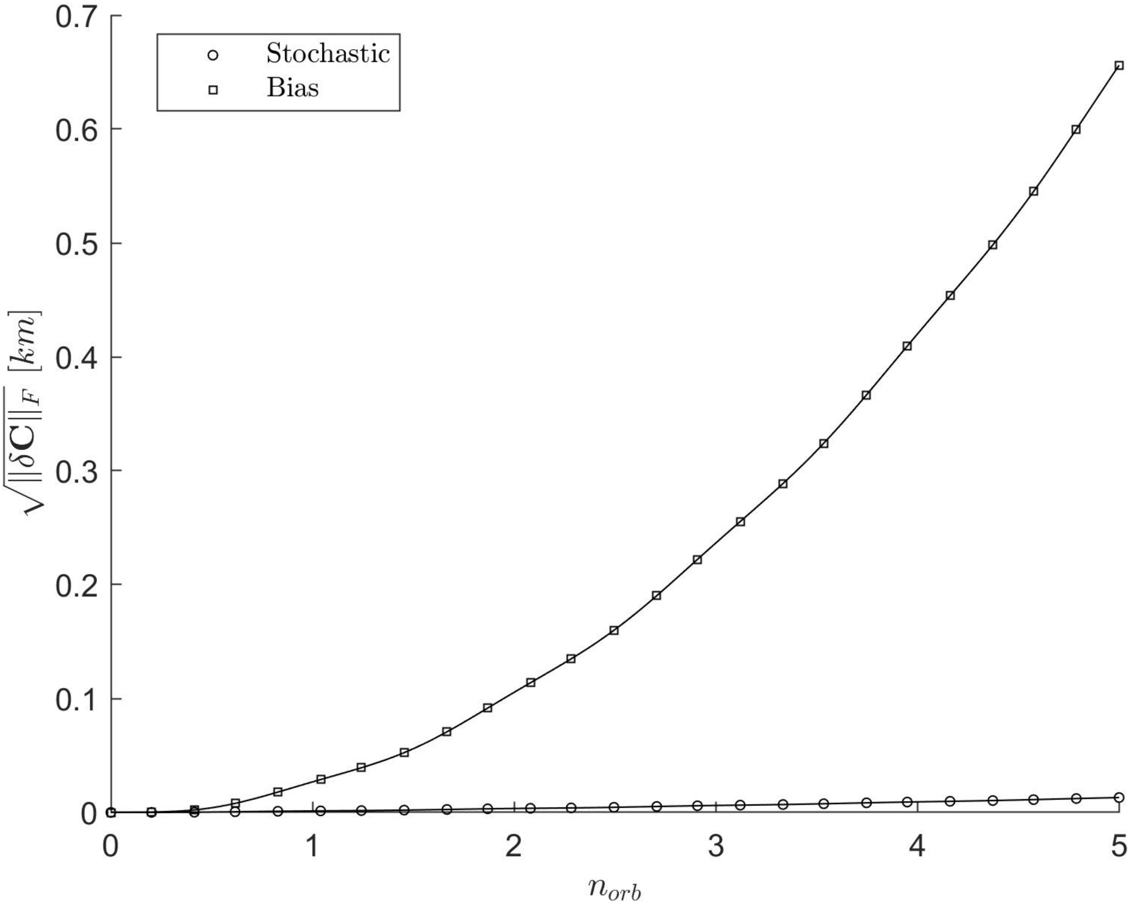

Figure 3.5: Covariance error metric as a function of propagation time in reference case 1. Two cases are shown: the thrust affected by a random bias and thrust affected by white noise.

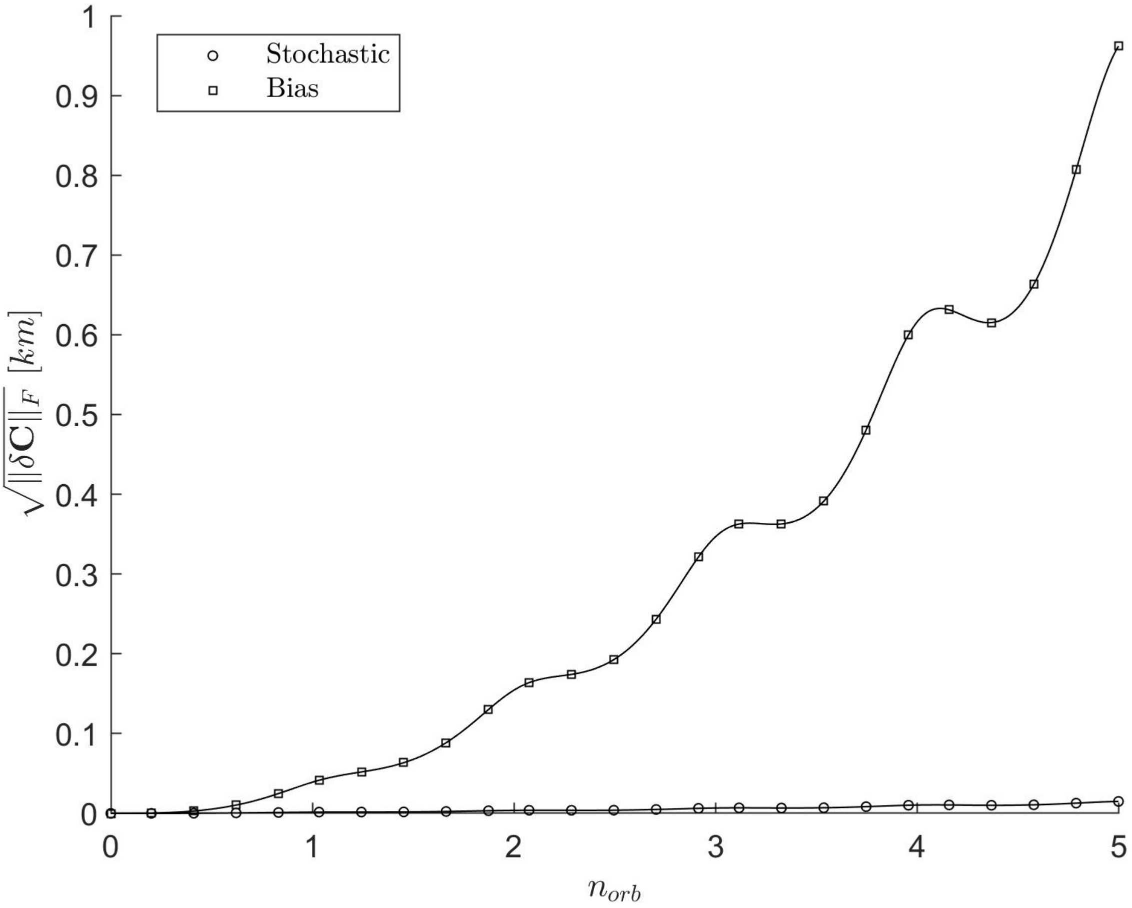

Figure 3.6: Covariance error metric as a function of propagation time in reference case 2. Two cases are shown: the thrust affected by a random bias and thrust affected by white noise.

dynamics, the modelling error is something always present. Although potentially controllable at the desired level of accuracy, often mathematical complexity and finite computational precision poses a limit.

The error committed, although systematic, is unpredictable, rising an uncertainty often referred to in the literature as *epistemic*.

The model error affects the computed risk index, e.g. probability of collision, thus the reliability of any CAM computation. As a result, the modelling error shall be subjected to the same propagation requirements outlined in Section 3.1. If these requirements are not met, inflation of the uncertainty coming from measurements shall be considered. Estimating such inflation is however not trivial because of the non-aleatory nature of the error.

Although for Keplerian dynamics and some conservative perturbations a full analytic solution is possible, this is not the case for a general low thrust. There are therefore different attempts to solve the full perturbed propagation problem, having different assumptions and accuracy.

In the subsections below, we review the state of the art models suitable for propagation of low thrust maneuvering spacecraft. As we are proposing in this dissertation an alternative propagation model, we report where possible the declared accuracy of the methods.

Lastly, we close with a subsection summarizing the current applications of such models in a COLA framework.

3.3.1 Perturbed modeling State of the art

With reference to (Curzi and Modenini, 2022), we examine what is the current state of the art for spacecraft trajectory propagation under a generic perturbation. In doing this, we will make stand out analytical models.

Optimization of maneuvers is the main line of application using perturbed modelling. Currently, the established techniques for low thrust optimization involves mainly numerical solutions (direct or indirect methods) of the perturbed orbital models (Morante et al., 2021). Instead, we would prefer an analytic solution for both computational efficiency and problem insight.

Generally speaking there are (semi) analytical studies providing models for perturbed orbital motion, at least for deterministic-assumed perturbations. SGP4 model is a typical example of semi-analytical model that can account for natural orbit perturbations such as atmospheric drag and simplified gravity potential. It cannot however model "custom" low thrust profiles, in this sense valuable efforts have been put towards analytic models.

Relevant to this work, several authors developed analytical solutions for the orbital motion under low thrust, most important of which are: Yang (2007), Bombardelli et al. (2011), Zuiani et al. (2012), Di Carlo et al. (2021) and Gonzalo and Colombo (2021). Although with different approximations, the approaches differ substantially only for the time element of the orbital element vector, undergoing ad-hoc treatment.

Yang (2007) provided approximate solutions using classical orbital elements for computing near-optimal low-thrust Earth orbit transfers. In doing so, he assumed three different thrust profile directions: tangential, inertial or piecewise constant out-of-plane thrust, including also the effect of J2.

He integrated the Gauss planetary equations along the fast angular variable (eccentric anomaly) for the first five orbital elements. The time law was instead approximated as purely Keplerian, i.e. neglecting the small perturbation presence.

Bombardelli et al. (2011) developed an analytical solution under the assumption of a small constant tangential thrust integrating the orbital dynamics along the sole fast variable, i.e. the angular position. They adopted a set of three generalized non-singular orbital parameters and introduced a Sundman transformation for the time equation. The time-of-flight instead, is integrated using a full first-order solution in the perturbing acceleration.

The accuracy of the model is measured in a Geosynchronous transfer orbit framework yielding about 1e-3% error for the position in a short term propagation, with a tangential acceleration of 1e-7km/s^2. Similarly, Zuiani et al. (2012) performed the same kind of integration but removing the tangentiality assumption of the thrust.

Di Carlo et al. (2021) lately extended the work of Zuiani et al. (2012) to include atmospheric perturbation, solar radiation pressure, third body and higher order harmonics. In both works the time equation was first reduced to its Keplerian version, and then integrated assuming first order variations in the remaining orbital elements.

Gonzalo and Colombo (2021) in a followup of their work (Gonzalo et al., 2019), adopted a similar approach for solving the time equation, by incorporating vari-

ations of the semi-major axis and eccentricity into the time equation expanded at first order in thrust. The resulting integral has been solved further adopting the analytical expansions of semi-major axis and eccentricity solutions to 4th order for small eccentricities. Authors also proposed to correct the outcome computed through the integration of Kepler's equation by adding the rotation of the line of apses, i.e. $\delta\omega$.
The reported relative accuracy for the orbital elements is between 1e-3% and 1e-4% in a short term propagation, with a tangential acceleration of 1e-7km/s^2.

Remark 3.5. To further improve accuracy, Bombardelli et al. (2011) proposed an update policy of the integration process, lately recalled by Gonzalo et al. (2019). Following this policy, at each orbital period the reference orbit is updated for the next integration in the fast variable. Potentially, this method is applicable to any of the above and the update can be made as frequent as we wish up to the point where the problem is essentially solved numerically (by small steps in time). On the other hand, it has to be noticed that this policy destroys the analytic nature of the model. △

A common point in the cited methods is that the integration of the equations of motion is carried out assuming constant all orbital elements. Exception made for the "fast" time element in some works. In the long-time horizon, this is a crude approximation especially for the semi-major axis whose real value slowly drifts away from the analytical solution. This negatively affects especially the time law in which the semi major axis variation plays a crucial role, as recognized for instance by Gonzalo and Colombo (2021).

3.3.2 Model applications to optimal evasive maneuvers

One of the firsts application examples of such models in a CAM scenario is given by Gonzalo et al. (2020). Considering a tangential thrust constraint, they adopted the eccentric anomaly as independent angular variable and built an analysis tool for collision avoidance considering the possibility of a low thrust. Specifically, they made use of analytic solution for the five orbital elements, but integrated the time equation numerically, since the resulting accuracy was not sufficient for COLA purposes.

Hernando-Ayuso and Bombardelli (2021) appears to be the first addressing fully analytically the optimization of low thrust CAM. They specifically described a formulation of the problem using the model in (Bombardelli et al., 2011) to obtain a solution in the circular orbit case. Thanks to the analytic form of the solution for the case of tangential thrust, they showed that this direction is the global optimal if some phasing conditions are met.

Remark 3.6. It is natural to adduce that the tangential direction may be in general a nearly optimal solution. The work by Bombardelli and Hernando-Ayuso (2014) corroborate this conclusion for impulsive thrust cases. They numerically show that a tangential maneuver tends to be the optimal thrust direction as the impulsive maneuver is applied earlier in time. The simplified study-cases made under tangential thrust have therefore a solid reason to be made. △

One last comment about the applications above is that none of them take into account the uncertainty in thrust realization. Instead, we have seen in the previous sections that thrust uncertainties may play significant role in propagation for COLA applications and therefore in CAM optimization.

3.4 Chapter Appendix

3.4.1 From 3-dimensional positional error to b-plane bound

With the aim of an approximated derivation at first order, consider the erroneous vectors at TCA in the 3D space:

$$\boldsymbol{\rho}_{\mathrm{t}}^{*} = \boldsymbol{\rho}_{\mathrm{t}} + \delta\boldsymbol{\rho}_{\mathrm{t}} \quad \mathit{and} \quad \boldsymbol{\nu}_{\mathrm{t}}^{*} = \boldsymbol{\nu}_{\mathrm{t}} + \delta\boldsymbol{\nu}_{\mathrm{t}}$$

where $\|\delta\boldsymbol{\rho}_{\mathrm{t}}\|/\|\boldsymbol{\rho}_{\mathrm{t}}\| << 1$ and $\|\delta\boldsymbol{\nu}_{\mathrm{t}}\|/\|\boldsymbol{\nu}_{\mathrm{t}}\| << 1$. The b-plane can deffer from the truth by means of both a position error and a velocity error, as the b-plane versors are defined as:

$$\hat{\boldsymbol{x}}_{\mathrm{t}} = \boldsymbol{\rho}_{\mathrm{t}}/\|\boldsymbol{\rho}_{\mathrm{t}}\| \quad \mathit{and} \quad \hat{\boldsymbol{y}}_{\mathrm{t}} = \hat{\boldsymbol{x}}_{\mathrm{t}} \times \boldsymbol{\nu}_{\mathrm{t}}/\|\boldsymbol{\nu}_{\mathrm{t}}\|$$

with the rotation matrix describing the b-plane given by

$$\boldsymbol{R}_{\mathrm{t}}^{\mathrm{b}} = \begin{bmatrix} \hat{\boldsymbol{x}}_{\mathrm{t}}^{T} \\ \hat{\boldsymbol{y}}_{\mathrm{t}}^{T} \end{bmatrix}$$

Remark 3.7. Notice that we are interested only in the first two rows of the matrix because we consider the projection on the b-plane. △

Then, the erroneous b-plane versors are:

$$\hat{\boldsymbol{x}^*}_{\mathrm{t}} = \hat{\boldsymbol{x}}_{\mathrm{t}} + \frac{\partial \hat{\boldsymbol{x}}_{\mathrm{t}}}{\partial \boldsymbol{\rho}_{\mathrm{t}}} \delta\boldsymbol{\rho}_{\mathrm{t}} = \hat{\boldsymbol{x}}_{\mathrm{t}} + (I - \frac{\boldsymbol{\rho}_{\mathrm{t}}\boldsymbol{\rho}_{\mathrm{t}}^T}{\|\boldsymbol{\rho}_{\mathrm{t}}\|^2}) \frac{\delta\boldsymbol{\rho}_{\mathrm{t}}}{\|\boldsymbol{\rho}_{\mathrm{t}}\|}$$

$$\hat{\boldsymbol{y}^*}_{\mathrm{t}} = \hat{\boldsymbol{y}}_{\mathrm{t}} + \frac{\partial \hat{\boldsymbol{y}}_{\mathrm{t}}}{\partial \boldsymbol{\rho}_{\mathrm{t}}} \delta\boldsymbol{\rho}_{\mathrm{t}} + \frac{\partial \hat{\boldsymbol{y}}_{\mathrm{t}}}{\partial \boldsymbol{\nu}_{\mathrm{t}}} \delta\boldsymbol{\nu}_{\mathrm{t}} = \hat{\boldsymbol{y}}_{\mathrm{t}} - [\hat{\boldsymbol{\nu}}_{\mathrm{t}}]^{\times}(I - \frac{\boldsymbol{\rho}_{\mathrm{t}}\boldsymbol{\rho}_{\mathrm{t}}^T}{\|\boldsymbol{\rho}_{\mathrm{t}}\|^2}) \frac{\delta\boldsymbol{\rho}_{\mathrm{t}}}{\|\boldsymbol{\rho}_{\mathrm{t}}\|} + \frac{[\boldsymbol{\rho}_{\mathrm{t}}]^{\times}}{\|\boldsymbol{\rho}_{\mathrm{t}}\|}(I - \frac{\boldsymbol{\nu}_{\mathrm{t}}\boldsymbol{\nu}_{\mathrm{t}}^T}{\|\boldsymbol{\nu}_{\mathrm{t}}\|^2}) \frac{\delta\boldsymbol{\nu}_{\mathrm{t}}}{\|\boldsymbol{\nu}_{\mathrm{t}}\|}$$

The error we would commit with such wrong b-plane in computing Pc is caused by the wrong relative position $\boldsymbol{\rho}^*{}_{\mathrm{t}}$. In fact, $\boldsymbol{\nu}$ is not entering the Foster's integral and the covairiance is assumed perfectly known. Then, the error in relative position on the b-plane is given by

$$\delta\boldsymbol{\rho}_{\mathfrak{b}} = \boldsymbol{\rho}_{\mathfrak{b}}^* - \boldsymbol{\rho}_{\mathfrak{b}} = \boldsymbol{R}^{*\mathfrak{b}}_{\mathrm{t}}(\boldsymbol{\rho}_{\mathrm{t}} + \delta\boldsymbol{\rho}_{\mathrm{t}}) - \boldsymbol{R}_{\mathrm{t}}^{\mathfrak{b}}\boldsymbol{\rho}_{\mathrm{t}}$$

However, we can now make use of the hypothesis that $\|\delta\boldsymbol{\rho}_{\mathrm{t}}\|/\|\boldsymbol{\rho}_{\mathrm{t}}\| << 1$ and $\|\delta\boldsymbol{\nu}_0\|/\|\boldsymbol{\nu}_{\mathrm{t}}\| << 1$.

Simplifying and neglecting second order terms in the relative position error we arrive at:

$$\delta\boldsymbol{\rho}_{\mathfrak{b}} = \boldsymbol{R}_{\mathrm{t}}^{\mathfrak{b}}\delta\boldsymbol{\rho}_{\mathrm{t}} + \begin{bmatrix} \frac{\delta\boldsymbol{\rho}_{\mathrm{t}}^T}{\|\boldsymbol{\rho}_{\mathrm{t}}\|}(I - \frac{\boldsymbol{\rho}_{\mathrm{t}}\boldsymbol{\rho}_{\mathrm{t}}^T}{\|\boldsymbol{\rho}_{\mathrm{t}}\|^2})\boldsymbol{\rho}_{\mathrm{t}} \\ \frac{\delta\boldsymbol{\rho}_{\mathrm{t}}^T}{\|\boldsymbol{\rho}_{\mathrm{t}}\|}(I - \frac{\boldsymbol{\rho}_{\mathrm{t}}\boldsymbol{\rho}_{\mathrm{t}}^T}{\|\boldsymbol{\rho}_{\mathrm{t}}\|^2})[\hat{\boldsymbol{\nu}}_{\mathrm{t}}]^{\times}\boldsymbol{\rho}_{\mathrm{t}} - \delta\boldsymbol{\nu}_{\mathrm{t}}^T(I - \frac{\boldsymbol{\nu}_{\mathrm{t}}\boldsymbol{\nu}_{\mathrm{t}}^T}{\|\boldsymbol{\nu}_{\mathrm{t}}\|^2})\frac{[\boldsymbol{\rho}_{\mathrm{t}}]^{\times}}{\|\boldsymbol{\rho}_{\mathrm{t}}\|}\boldsymbol{\rho}_{\mathrm{t}} \end{bmatrix}$$

This further simplifies noticing that $[\boldsymbol{\rho}_{\mathrm{t}}]^{\times}\boldsymbol{\rho}_{\mathrm{t}} = \mathbf{0}$ and $\boldsymbol{\rho}_{\mathrm{t}}^T\boldsymbol{\rho}_{\mathrm{t}} = \|\boldsymbol{\rho}_{\mathrm{t}}\|^2$. Notice that, as the rightmost matrix is a column vector, it is possible to take the transpose of each entry so that $\delta\boldsymbol{\rho}_{\mathrm{t}}$ is a common multiplier at the right, yielding:

$$\delta\boldsymbol{\rho}_{\mathfrak{b}} = (\boldsymbol{R}_{\mathrm{t}}^{\mathfrak{b}} + \begin{bmatrix} \mathbf{0}_{1\times 3} \\ \hat{\boldsymbol{\nu}}_{\mathrm{t}}^T[\boldsymbol{\rho}_{\mathrm{t}}]^{\times}/\|\boldsymbol{\rho}_{\mathrm{t}}\| \end{bmatrix})\delta\boldsymbol{\rho}_{\mathrm{t}}$$

We shall now notice that the second row coincides with $-\hat{\boldsymbol{y}}_{\mathfrak{b}}^T$ meaning that at first order

$$\delta\boldsymbol{\rho}_{\mathfrak{b}} = \begin{bmatrix} \hat{\boldsymbol{x}}_{\mathrm{t}}^T \\ \mathbf{0}_{1\times 3} \end{bmatrix} \delta\boldsymbol{\rho}_{\mathrm{t}}$$

Remark 3.8. This is actually to be expected as the b-plane is defined with the x-axis pointing to the secondary object. we will not commit any error perpendicular to that direction as, by construction, we always obtain a null y-component on the b-plane. △

Thanks to the sub-multiplicative property of matrix norm we then have $\|\delta\boldsymbol{\rho}_{\mathfrak{b}}\| \leq \|\delta\boldsymbol{\rho}_{\mathfrak{t}}\|$.

3.4.2 Translation of signal stability to noise power density

Clark et al. (2019) report a thrust stability for Bepicolombo thrusters of ± 0.5mN in a 4-minutes averaging window. Meaning that averaging the noisy signal over 4 minutes the resulting running average has oscillations at most of ± 0.5mN. When working with 154mN nominal thrust this resulted in a 0.35% bound.
We empirically interpret the stability as the condition when a thrust error remain constant to a value within the bounds for the 4 minutes, before changing to another random value (always within the bounds) and so on. From this interpretation, one can guess a reasonable white noise intensity as follows. Suppose the ± 0.5mN bound is a 2-sigma bound, reflecting the 95% confidence (fearly high) to fall within the bounds. This is to say that the random extractions (at 4 minutes intervals) has ± 0.25mN standard deviation (0.175%).

In Section 3.2.2, we work with a nominal acceleration of 5e-8 km/s^2 so that the random extractions shall have a standard deviation 0.175% of 5e-8 km/s^2. The white noise intensity (N_s) generating such condition is given by solving:

$$8.5\text{e}{-11} = \frac{N_s}{\sqrt{4 \cdot 60}}$$

Then, one can generate the white noise as $N_s\,\xi/\sqrt{dt}$, where dt is the desired time step of the stochastic simulation and $\xi \sim N(0, 1)$ a realization from a a standard-normal distribution. Notice that the extraction variance for the 4-minutes averaging window is fulfilled when $dt = 4min$.

4

Analytic propagation model

In this chapter, a novel analytical propagation model is presented for spacecraft subjected to small accelerations. Although the solution is explicitly obtained under the restriction of tangential perturbations, we shall see that the implicit model solution is valid for any small periodic acceleration.

Finally, some use-cases of the explicit solution will be shown concerning both position and uncertainty propagation. In doing so, we shall also compare the performance with state of the art methods.

4.1 Physics preliminary

The Gauss Planetary Equations (GPE) offer a mathematically exact way of describing the orbital dynamics of a spacecraft subjected to perturbing acceleration.

GPE assume a different form depending on the adopted state vector, i.e. orbital elements. In this derivation, we use the set of classical (Keplerian) orbital elements indicated with $\boldsymbol{\alpha} \in \mathbb{R}^6$ and made by:

$$[a, e, i, \Omega, \omega, t]^T = [\boldsymbol{\alpha}_r^T, t]^T,$$

where a is the semi-major axis, e the eccentricity, Ω the argument of ascending node, ω the argument of pericenter and t the time. The choice of time as sixth orbital element reflects the fact that the final form of the GPE to be solved shall adopt an angular anomaly as the independent variable.
The subscript "r", standing for reduced, is in general adopted in the following to indicate the first 5 orbital elements of a vector.

Battin (1999) offers few GPE variants with classical orbital elements, here we are particularly interested into ones in the form:

$$\frac{d\boldsymbol{\alpha}^\star}{dt} = \boldsymbol{\Psi}(t, \boldsymbol{\alpha}^\star, \boldsymbol{a}_p),$$

where we temporarily adopted $\boldsymbol{\alpha}^\star = [\boldsymbol{\alpha}_r^T, E]^T$, and $\boldsymbol{a}_p \in \mathbb{R}^3$ is the 3D perturbing acceleration. $\boldsymbol{\Psi}$ is the form of GPE where $\boldsymbol{a}_p$ appears in the normal-tangential-binormal $(\eta,\ \tau,\ n)$ frame of reference.
Notice that the t-dependency is put for sake of generality and symmetry. In fact, if only external acceleration acts on the spacecraft, $\boldsymbol{\Psi}$ can depend on time only through $\boldsymbol{a}_p$ or $\boldsymbol{\alpha}^\star$. To give a counter example, this may not be the case if we had to consider the orbital elements variation in a two body problem with variable masses.

Due to the fact that $E(t)$ appears explicitly in GPE, rather than t, the system of equation can be more easily integrated if in the form:

$$\frac{d\boldsymbol{\alpha}}{dE} = \boldsymbol{f}(E, \boldsymbol{\alpha}, \boldsymbol{a}_p) \tag{4.1}$$

This can be obtained by simply letting:

$$\boldsymbol{f}(E, \boldsymbol{\alpha}, \boldsymbol{a}_p) = \begin{bmatrix} \boldsymbol{\Psi}_r(t, \boldsymbol{\alpha}^\star, \boldsymbol{a}_p)(\frac{dE}{dt})^{-1} \\ \frac{dt}{dE} \end{bmatrix}$$

The expression for $\frac{dE}{dt}$ is given again in Battin (1999) at page 489.

4.1.1 Non-dimensional form of GPE

The analytical expressions are simplified if we regard the non dimensional form of the GPE. With this aim, we define the non-dimensional semi-major axis and time respectively as:

$$\tilde{a} = \frac{a}{a_c}, \quad \tilde{t} = n_c t,$$

where a_c is the chief semi-major axis and $n_c = \sqrt{\mu/a_c^3}$ the chief mean motion. With the term *chief* we refer to a reference orbit whose orbital elements, in this work, are taken coincident with the initial orbital elements.
In the reaming of the manuscript we will refer to $\boldsymbol{\alpha}$ as its non dimensional form, i.e. $\boldsymbol{\alpha} = [\tilde{a}, e, i, \Omega, \omega, \tilde{t}]$. The non-dimensional form of the GPE can be found explicitly in Chapter Appendix 4.6.1.

4.2 Averaging theory preliminary

In averaging applications we are concerned with the solution of a differential equation of the type:

$$\dot{\boldsymbol{x}} = \boldsymbol{g}(\boldsymbol{x}, t, \epsilon) \quad with \quad \boldsymbol{x}(0) = \boldsymbol{x}_0 \tag{4.2}$$

with $\boldsymbol{x}, \boldsymbol{x}_0 \in \mathbb{R}^d$, $\epsilon \in \mathbb{R}$ arbitrarily small and $\boldsymbol{g} : \mathbb{R}^d \to \mathbb{R}^d$ a generic function.
Averaging theory seeks to adopt an averaged version of the problem and quantify how much close its solution is to the actual one.
In the following we shall restrict to the case where $\epsilon \in \mathbb{R}^+ \cup \{0\}$. As ϵ usually account for magnitude of some perturbation, this restriction is not a big limitation in practical applications.
First of all, let us recall some basic definitions from Sanders et al. (2000) that help defining the mathematical meaning of "close" solutions.

Definition 4.1. *Let $\breve{\epsilon} \in \mathbb{R}^+$, a function $\delta(\epsilon) : \mathbb{R} \to \mathbb{R}$ is called order function if:*

- *$\delta(\epsilon)$ is continuous and positive in some interval $(0, \breve{\epsilon}]$*
- *$\lim_{\epsilon \to 0^+} \delta(\epsilon)$ exists*

Definition 4.2. *Let $\phi(t, \epsilon)$ be a real or vector-valued function defined for $\epsilon \geq 0$ and for $t \in \mathcal{I}_\epsilon$, where $\mathcal{I}_\epsilon$ is an interval that may be ϵ-dependent.*
The expression "for $\epsilon \to 0^+$" means that there exist an $\breve{\epsilon} > 0$ such that the preceding statement holds for all $(0, \breve{\epsilon}]$.
Then, we say that $\phi(t, \epsilon) = \mathcal{O}(\delta(\epsilon))$ for $\epsilon \to 0^+$ and we read it as "$\phi(t, \epsilon)$ is of the order

of $\delta(\epsilon)$*", if:*
there exits a constant $\breve{\epsilon} > 0$ *and* $k > 0$ *such that* $\|\phi(t,\epsilon)\| \leq k|\delta(\epsilon)|$ *for all* $t \in \mathcal{I}_\epsilon$ *and* $\epsilon \in (0, \breve{\epsilon}]$.

When $\phi(t,\epsilon)$ is taken to be the difference between two solutions (e.g. the real and the averaged one), the definition above states the meaning of closeness. Notice that the closeness does not constrain the maximum error, rather its trend when the perturbation is scaled.

Definition 4.3. *Let* L *be a positive constant independent of* ϵ. *We say that* $\phi(t,\epsilon) = \mathcal{O}(\delta(\epsilon))$ *for* $\epsilon \to 0^+$ *on the time scale* $\delta(\epsilon)^{-1}$ *if the statement holds for* $0 \leq \delta(\epsilon)t \leq L$. *Or equivalently* $\mathcal{I}_\epsilon = [0, L\delta(\epsilon)^{-1}]$.

$\boldsymbol{g}(\cdot)$ in Eq. 4.2 can be in general a nonlinear function of the perturbation ϵ. As we assume $\epsilon \in (0, \breve{\epsilon}]$, if $\boldsymbol{g}$ is differentiable in ϵ an expansion in terms of Taylor series around $\epsilon = 0$ does make sense.

$$\boldsymbol{g}(\boldsymbol{x}, t, \epsilon) = \boldsymbol{g}^0(\boldsymbol{x}, t) + \epsilon \boldsymbol{g}^1(\boldsymbol{x}, t) + \ldots + \epsilon^r \boldsymbol{g}^r(\boldsymbol{x}, t) + \ldots ,$$

where $\boldsymbol{g}^r(\boldsymbol{x}, t) = D^r_\epsilon \boldsymbol{g}(\boldsymbol{x}, t, 0)$ and the superscript of $\boldsymbol{g}$ means clearly the power of ϵ to which it is referred.
This takes the name of asymptotic expansion when ϵ^r gets smaller and smaller as $r \to \infty$ and $\epsilon \to 0^+$.

Remark 4.1. Notice that $\boldsymbol{g}^0(\boldsymbol{x}, t)$ reflects the so-called unperturbed problem. If one further collects a leading ϵ, the following form is obtained:

$$\boldsymbol{g}(\boldsymbol{x}, t, \epsilon) = \boldsymbol{g}^0(\boldsymbol{x}, t) + \epsilon \boldsymbol{g}^{[1]}(\boldsymbol{x}, t, \epsilon)$$

Note that the $\boldsymbol{g}$'s first-order exponent is now in square brackets because including also higher order terms. △

It is customary to call *standard form* of a perturbation problem the one in the form:

$$\dot{\boldsymbol{x}} = \epsilon \boldsymbol{g}^{[1]}(\boldsymbol{x}, t, \epsilon) \quad with \quad \boldsymbol{x}(0) = \boldsymbol{x}_0 \tag{4.3}$$

Within this manuscript, we shall be concerned only with this kind of problems.

4.2.1 Periodic Averaging

We have a periodic averaging problem if $\boldsymbol{g}^1(\boldsymbol{x}, t, \epsilon)$ and $\boldsymbol{g}^{[2]}(\boldsymbol{x}, t, \epsilon)$ are periodic in t with some period T. We define averaged system associated to the original system:

$$\dot{\boldsymbol{z}} = \bar{g}^1(\boldsymbol{z}, \epsilon) \quad with \quad \boldsymbol{z}(0) = \boldsymbol{z}_0,$$

where $\bar{\boldsymbol{g}}^1(\boldsymbol{x}, \epsilon) = \frac{1}{T}\int_0^T \boldsymbol{g}^1(\boldsymbol{x}, s, \epsilon)ds$ and the integration is performed keeping $\boldsymbol{x}$ constant. Note that thanks to periodicity, $\bar{\boldsymbol{g}}^1(\boldsymbol{x}, \epsilon)$ does not explicitly depend on t.

Remark 4.2. The initial conditions may not be necessarily the same as the original system, e.g. $\boldsymbol{z}_0 \neq \boldsymbol{x}_0$. △

The usefulness of this auxiliary system is stated by the following theorem (Sanders et al., 2000):

Theorem 4.1. *Let* $\boldsymbol{g}^{[1]}(\boldsymbol{x}, t, \epsilon) : \mathbb{R}^d \times \mathbb{R} \times \mathbb{R}^+ \rightarrow \mathbb{R}^d$ *such that* $\boldsymbol{g}^1(\boldsymbol{x}, t, \epsilon)$ *is lipschitz-continuous and* $\boldsymbol{g}^{[2]}(\boldsymbol{x}, t, \epsilon)$ *is continuous. Let moreover be* $\breve{\epsilon} \in \mathbb{R}^+$*,* $D \subset \mathbb{R}^d$ *and* $L \in \mathbb{R}$*. Then, there exist* $k > 0$ *(of Definition 4.2) such that:*

$$\|\boldsymbol{x}(t, \epsilon) - \boldsymbol{z}(t, \epsilon)\| = \mathcal{O}(\epsilon)$$

on the time scale $\mathcal{O}(1/\epsilon)$*.*

Practically, the theorem is saying that for "small" ϵ the averaged solution has an error with respect to the true solution that is proportional to ϵ itself. Moreover, this conclusion is valid on a "time-scale" proportional to $1/\epsilon$ (not necessarily with the same constant of proportionality), i.e. the order function is $\delta(\epsilon) = \epsilon$. That is, the smaller the perturbation the longer the validity of the averaged solution, which is intuitively reasonable.

If the average solution is not accurate enough, one can aim at lowering the error magnitude by adding a "short-period" perturbation. This can be formalized adopting a higher-order averaging, which is possible for periodic systems (see p.40 of Sanders et al. (2000)) or using the so called *improved first approximation*. In this work we adopted the second strategy because is less numerically cumbersome while achieving good performance.
Let us start by defining the *near-identity transformation*, fundamental to the *improved first approximation*.

Definition 4.4. *Let* $\boldsymbol{x}(t,\epsilon)$ *be the solution to the original periodic system. Let moreover* $\boldsymbol{y}(t,\epsilon)$ *be the solution to the associated fully averaged equation* $\dot{\boldsymbol{y}} = \epsilon\bar{\boldsymbol{g}}^1(\boldsymbol{y}) + \epsilon^2\bar{\boldsymbol{g}}^{[2]}(\boldsymbol{y},\epsilon)$*. We call near-identity transformation a function*

$$\boldsymbol{x} = \boldsymbol{\mathcal{U}}(\boldsymbol{y},t,\epsilon) = \boldsymbol{y} + \epsilon\boldsymbol{u}^{[1]}(\boldsymbol{y},t,\epsilon) \tag{4.4}$$

where $\boldsymbol{u}^{[1]}(\boldsymbol{y},t,\epsilon)$ *is a periodic function with period* T*.*

The existence of such mapping, which is proven by Sanders et al. (2000), ensures that the solution to a periodic system can always be decomposed into an average solution plus a periodic perturbation. Note that in general $\boldsymbol{y} \neq \boldsymbol{z}$ as it is the solution of the fully averaged equation (notice the square brackets).

The *improved first approximation* consists of forcing $\boldsymbol{y} = \boldsymbol{z}$. Then, by differentiation of 4.4 an approximate first order short-period term can be obtained by integrating:

$$\frac{\partial\boldsymbol{u}^1}{\partial t} = \boldsymbol{g}^1(\boldsymbol{z},t) - \bar{\boldsymbol{g}}^1(\boldsymbol{z})$$

Remark 4.3. Notice that i) a partial derivative is involved, so the integration can be carried out considering $\boldsymbol{z}$ as a constant, and ii) the resulting $\boldsymbol{u}^1$ is only the first periodic contribution to $\boldsymbol{u}^{[1]}$. △

Eventually, the *improved first approximation* can be expressed as:

$$\boldsymbol{x} \approx \boldsymbol{z} + \epsilon\boldsymbol{u}^1(\boldsymbol{z},t), \tag{4.5}$$

which is still correct to first order only, i.e. error scales proportionally with ϵ.

4.2.2 Non-Periodic Averaging

If the system is not periodic, e.g. $\boldsymbol{g}^1(\boldsymbol{x},t,\epsilon)$ is not periodic, standard averaging theory poses other restrictions on the dynamical system for formal error estimates to be obtained. Here instead, we will restrict ourselves to a special class of non-periodic systems of interest, for which the periodic and non-periodic state components can be separated, with the governing equation depending only on the periodic part. Specifically, denoted with subscripts p and np the periodic and non periodic parts respectively, such system can be written as in:

$$\dot{\boldsymbol{x}} = \begin{bmatrix} \dot{\boldsymbol{x}}_p \\ \dot{\boldsymbol{x}}_{np} \end{bmatrix} = \epsilon \begin{bmatrix} \boldsymbol{g}_p^1(\boldsymbol{x}_p, t, \epsilon) \\ \boldsymbol{g}_{np}^1(\boldsymbol{x}_p, t, \epsilon) \end{bmatrix} \tag{4.6}$$

Note that Gauss Planetary Equations can fall in this class, with $\boldsymbol{x}_p$ being the first five orbital elements, and $\boldsymbol{x}_{np}$ the sixth element (time). In fact, in case the perturbing acceleration does not depend explicitly on time, also GPE in the form of Eq. 4.1 do not depend explicitly on time.
In this case, the average solution to the periodic part can be found solving $\dot{\boldsymbol{z}} = \epsilon \bar{\boldsymbol{g}}_p^1(\boldsymbol{z}, t, \epsilon)$. Then, similarly to the *improved first approximation* approach, we can approximate the non-periodic differential equation by:

$$\dot{\boldsymbol{x}}_{np} \approx \epsilon \boldsymbol{g}_{np}^1(\boldsymbol{z}, t, \epsilon)$$

So that the right hand side reduces to a function of time only to be integrated.

Properties on the error introduced by such approximation cannot be drawn in general. Nevertheless, some error estimate can be obtained restricting to the case of a linear time-variant, non-periodic part, e.g. when

$$\dot{\boldsymbol{x}}_{np} = \epsilon(\boldsymbol{q}_{np}(t) + \boldsymbol{Q}_{np}(t)\boldsymbol{x}_p)$$

With $\boldsymbol{q}_{np}$ and $\boldsymbol{Q}_{np}$ generic non-periodic vectorial and matrix functions respectively.
Suppose the average solution to the periodic part is still some $\boldsymbol{z}(t)$. Then the error committed using the approach described above in the interval of validity $\mathcal{I}_\epsilon = [0, L/\epsilon]$ is:

$$\|\delta \boldsymbol{x}_{np}\| = \|\epsilon \int_{\mathcal{I}_\epsilon} \boldsymbol{g}_{np}^1(\boldsymbol{x}_p, t, \epsilon) - \boldsymbol{g}_{np}^1(\boldsymbol{z}, t, \epsilon) dt\| = \|\epsilon \int_{\mathcal{I}_\epsilon} \boldsymbol{Q}_{np}(t)(\boldsymbol{x}_p - \boldsymbol{z}) dt\|$$

Using standard inequality identities one can obtain:

$$\|\epsilon \int_{\mathcal{I}_\epsilon} \boldsymbol{Q}_{np}(t)(\boldsymbol{x}_p - \boldsymbol{z}) dt\| \leq \epsilon \int_{\mathcal{I}_\epsilon} \|\boldsymbol{Q}_{np}(t)\| \|\boldsymbol{x}_p - \boldsymbol{z}\| dt$$

The right hand side can be further up-bounded in the interval $\mathcal{I}_\epsilon$ by considering:

- The supreme of $\|\boldsymbol{Q}_{np}(t)\|$ in the interval, i.e.

$$\sup_{t\in\mathcal{I}_\epsilon} \|\boldsymbol{Q}_{np}(t)\|$$

- The order ϵ of $\boldsymbol{x}_p - \boldsymbol{z}$ in the interval, i.e. $\boldsymbol{x}_p - \boldsymbol{z} = \mathcal{O}(\epsilon)$ with a constant $k > 0$

Then we obtain:

$$\|\delta\boldsymbol{x}_{np}\| \leq \epsilon \sup_{t\in\mathcal{I}_\epsilon} \|\boldsymbol{Q}_{np}(t)\| k\epsilon \frac{L}{\epsilon} = k'\epsilon \sup_{t\in\mathcal{I}_\epsilon} \|\boldsymbol{Q}_{np}(t)\|$$

By definition of order of a function, this means that the obtained solution $\boldsymbol{x}^*_{np}$ is an approximation of order $\epsilon \sup_{t\in\mathcal{I}_\epsilon} \|\boldsymbol{Q}_{np}(t)\|$ of the real solution $\boldsymbol{x}_{np}$ in the time interval $[0, L/\epsilon]$.

Loosely speaking, in case of a linear state dependence, the proposed approach obtains a solution of the non-periodic part which is "quasi-ϵ" order. The quality of this solution thus depends on the behavior of $\|\boldsymbol{Q}_{np}(t)\|$, it gets worse as $\|\boldsymbol{Q}_{np}(t)\|$ maximum value gets higher on the interval of validity.

4.3 Model derivation

The proposed model leverages the fact that most perturbations of interest for GPE are small. Consequently, also the variations of orbital elements are small (with respect to unperturbed case). As a result, we can effectively linearize the equations of motion with respect to both the perturbation ϵ and the state vector $\boldsymbol{\alpha}$. We refer to this process as a *double stage expansion* around a null perturbative acceleration and a chief (osculating) orbital elements vector $\boldsymbol{\alpha}_c$.

As anticipated in Section 4.2.2, the model is conveniently solvable using averaging theory only under the hypothesis that the "time" orbital element does not appear explicitly in the perturbation (so that Eq. 4.6 is enforced). This is, however, a minor limitation as long as most perturbations can be described through explicit dependence on angular anomalies rather than time.

4.3.1 First-order perturbation expansion

By "small" perturbations, we mean that the acceleration to which the spacecraft is subjected is much smaller than the local gravity, i.e.

$$\frac{\boldsymbol{a}_p}{\mu/a_c^2} = \tilde{\boldsymbol{a}}_p(E, \boldsymbol{\alpha}, \epsilon)$$

Where a_c is the semi major axis of the chief orbit, ϵ a small positive constant and $\|\tilde{\boldsymbol{a}}_p\| << 1$.

Without loss of generality, we can rewrite the right hand side of the above equation as:

$$\tilde{\boldsymbol{a}}_p(E, \boldsymbol{\alpha}, \epsilon) = \epsilon \boldsymbol{b}(E, \boldsymbol{\alpha})$$

Where $\boldsymbol{b}$ is a function of order 1 (with the meaning given in Section 4.2), i.e. it does not depend on the scaling parameter ϵ.

Remark 4.4. Notice that the requirement $\|\tilde{\boldsymbol{a}}_p\| << 1$ becomes $\|\boldsymbol{b}(E, \boldsymbol{\alpha})\| << 1/\epsilon$ $\triangle$

Then, a first order expansion of Eq. 4.1 around $\tilde{\boldsymbol{a}}_p = 0$ is obtained as:

$$\frac{d\boldsymbol{\alpha}}{dE} \approx \boldsymbol{f}^0(E, \boldsymbol{\alpha}) + \boldsymbol{f}^1(E, \boldsymbol{\alpha})\boldsymbol{b}(E, \boldsymbol{\alpha})\epsilon, \tag{4.7}$$

where $\boldsymbol{f}^0(E, \boldsymbol{\alpha})$ is $\boldsymbol{f}$ evaluated at $\tilde{\boldsymbol{a}}_p = 0$, i.e the GPE for a keplerian orbit:

$$\left.\frac{d\boldsymbol{\alpha}}{dE}\right|_{\epsilon=0} = \begin{bmatrix} \boldsymbol{0}_{5\times 1} \\ \tilde{a}^{3/2}(1 - e\cos E) \end{bmatrix},$$

whereas $\boldsymbol{f}^1(E, \boldsymbol{\alpha})$ is the gradient of $\boldsymbol{f}$ with respect to $\tilde{\boldsymbol{a}}_p$ and evaluated at $\tilde{\boldsymbol{a}}_p = \boldsymbol{0}$, i.e. a 6×3 matrix. Using the non-dimensional formula given in the Chapter Appendix 4.6.1, the explicit expressions for $\boldsymbol{f}^1(E, \boldsymbol{\alpha})$ are given in the Chapter Appendix 4.6.2.

4.3.2 First-order orbit state expansion

With reference to the first-stage GPE linearization in Eq. 4.7, we can distinguish between fast and slow variables. Specifically we can label "slow" the $\boldsymbol{\alpha}_r$ orbital elements because their derivatives are proportional to the small perturbation ac-

celeration. The time variable instead, has to be regarded as "fast" because the Keplerian part of the derivative is not proportional to the perturbation.
A common strategy used to find approximate solution for the slow-variables consists of integrating the right hand side of Eq. 4.7 keeping the orbital elements constant at their initial value, i.e. $\boldsymbol{\alpha} = \boldsymbol{\alpha}_c$ (see e.g. (Gonzalo et al., 2019), (Di Carlo et al., 2021)). Here instead, we will attempt to obtain a more accurate approximation by allowing first-order variations of $\boldsymbol{\alpha}$ about $\boldsymbol{\alpha}_c$, i.e. by linearizing further Eq. 4.7 with respect to the state vector, as in:

$$\frac{d\boldsymbol{\alpha}}{dE} \approx \boldsymbol{f}^0(E, \boldsymbol{\alpha}_c) + \nabla_{\boldsymbol{\alpha}} \boldsymbol{f}^0(E, \boldsymbol{\alpha}_c)\delta\boldsymbol{\alpha} + \left(\boldsymbol{f}^1_{\boldsymbol{b}}(E, \boldsymbol{\alpha}_c) + \nabla_{\boldsymbol{\alpha}} \boldsymbol{f}^1_{\boldsymbol{b}}(E, \boldsymbol{\alpha}_c)\delta\boldsymbol{\alpha}\right)\epsilon,$$

where the notation $\boldsymbol{f}^1_{\boldsymbol{b}}$ indicates the multiplication $\boldsymbol{f}^1(E, \boldsymbol{\alpha})\boldsymbol{b}(E, \boldsymbol{\alpha})$ and $\delta\boldsymbol{\alpha} = \boldsymbol{\alpha} - \boldsymbol{\alpha}_c$ is the orbital elements variation.
It is convenient to directly solve for the variation $\delta\boldsymbol{\alpha}$, since its dynamics is simpler:

$$\frac{d\delta\boldsymbol{\alpha}}{dE} \approx \nabla_{\boldsymbol{\alpha}} \boldsymbol{f}^0(E, \boldsymbol{\alpha}_c)\delta\boldsymbol{\alpha} + \left(\boldsymbol{f}^1_{\boldsymbol{b}}(E, \boldsymbol{\alpha}_c) + \nabla_{\boldsymbol{\alpha}} \boldsymbol{f}^1_{\boldsymbol{b}}(E, \boldsymbol{\alpha}_c)\delta\boldsymbol{\alpha}\right)\epsilon$$

For notation simplicity, we introduce the symbols $\boldsymbol{A}^0(E) = \nabla_{\boldsymbol{\alpha}} \boldsymbol{f}^0(E, \boldsymbol{\alpha}_c)$, $\boldsymbol{A}^1(E) = \nabla_{\boldsymbol{\alpha}} \boldsymbol{f}^1_{\boldsymbol{b}}(E, \boldsymbol{\alpha}_c)$, so that the resulting equation is:

$$\frac{d\delta\boldsymbol{\alpha}}{dE} \approx \epsilon \boldsymbol{f}^1_b(E) + \left(\boldsymbol{A}^0(E) + \epsilon \boldsymbol{A}^1(E)\right)\delta\boldsymbol{\alpha} \tag{4.8}$$

The terms $\boldsymbol{f}^1_b$ and $\boldsymbol{A}^1$ are clearly perturbation-dependent through $\boldsymbol{b}$. An expression will be provided in the next section when specializing the model for the case of a constant tangential acceleration.
$\boldsymbol{A}^0$ is instead a simple block matrix in the form:

$$\boldsymbol{A}^0 = \begin{bmatrix} & \boldsymbol{0}_{5\times 6} & \\ \frac{3\tilde{a}^{1/2}(1 - e\cos E)}{2} & \tilde{a}^{3/2}\cos E & \boldsymbol{0}_{1\times 4} \end{bmatrix} \tag{4.9}$$

As only the last row contains non-null entries, it provides the sensitivity of the time element to variations of the osculating orbit.

The final form of the double stage linearization (Eq. 4.8) is a linear first-order non-homogeneous ordinary differential equation for $\delta\boldsymbol{\alpha}$. The general solution to this final form does exist in terms of state transition matrix. The latter however is difficult to obtain as in our case the system is time variant. The next section is dedicated to approximate analytically such solution using averaging theory.

4.4 Model solution

To apply averaging theory to the problem in Eq. 4.8, we need to reduce the equation to its standard averaging form. This, in turn, can be obtained by applying the variation of constants methods (Sanders et al., 2000). Consider then the associated unperturbed problem, that is:

$$\frac{d\boldsymbol{\theta}}{dE} = \boldsymbol{A}^0(E)\boldsymbol{\theta},$$

where we used $\boldsymbol{\theta}$ in place of $\delta\boldsymbol{\alpha}$ just to distinguish between the unperturbed and perturbed solutions. The solution to this system is readily available thanks to the particular form of $\boldsymbol{A}^0$ (see Eq.4.9). Considering $\boldsymbol{\vartheta} \in \mathbb{R}^6$ the vector of integration constants, we have:

$$\boldsymbol{\theta} = \left(I + \mathfrak{A}^0(E)\right)\boldsymbol{\vartheta}, \tag{4.10}$$

where $\mathfrak{A}^0(E) = \int \boldsymbol{A}^0(E')dE'$.
In force of the variation of constants method, we assume $\boldsymbol{\vartheta} = \boldsymbol{\vartheta}(E)$ and set $\delta\boldsymbol{\alpha} = \boldsymbol{\theta}(\boldsymbol{\vartheta}(E), E)$. Then recalling Eq. 4.8, we have:

$$\frac{\partial\boldsymbol{\theta}}{\partial E} + \nabla_{\vartheta}\boldsymbol{\theta}\frac{d\boldsymbol{\vartheta}}{dE} = \boldsymbol{A}^0(E)\boldsymbol{\theta} + \epsilon\left(\boldsymbol{f}_b^1(E) + \boldsymbol{A}^1(E)\boldsymbol{\theta}\right)$$

In this expression, the leftmost terms of both sides simplify as $\boldsymbol{\theta}$ is the solution of the unperturbed problem. Furthermore, using Eq. 4.10, we obtain a differential equation for $\boldsymbol{\vartheta}$:

$$\frac{d\boldsymbol{\vartheta}}{dE} = \epsilon\left(I + \mathfrak{A}^0(E)\right)^{-1}\left[\boldsymbol{f}_b^1(E) + \boldsymbol{A}^1(E)\left(I + \mathfrak{A}^0(E)\right)\boldsymbol{\vartheta}\right] \tag{4.11}$$

First observe that this system is in the standard form of averaging. Then observe that thanks to the special form of $\boldsymbol{A}^0$, we have $(1 + \mathfrak{A}^0(E))^{-1} = 1 - \mathfrak{A}^0(E)$. Lastly, observe that $\mathfrak{A}^0(E)$ is a non-periodic function; also $\boldsymbol{b}(E, \boldsymbol{\alpha})$ may not be periodic in general.

At this stage, we introduce two restrictions to recover the periodic part decoupling and use periodic averaging:

- $\boldsymbol{b}(E,\boldsymbol{\alpha})$ is periodic in E.
- the perturbing acceleration does not depend explicitly on the time t, i.e. $\frac{\partial \boldsymbol{b}(E,\boldsymbol{\alpha})}{\partial \tilde{t}} = 0$

The second point implies that the last column of $\boldsymbol{A}^1$ will be null and $\boldsymbol{A}^1(E)\mathfrak{A}^0(E) = \mathbf{0}$. Therefore, the system in Eq. 4.11 becomes:

$$\frac{d\boldsymbol{\vartheta}}{dE} = \epsilon\left(I - \mathfrak{A}^0(E)\right)\left[\boldsymbol{f}_b^1(E) + \boldsymbol{A}^1(E)\boldsymbol{\vartheta}\right] \tag{4.12}$$

The standard system in Eq. 4.12 is not fully periodic in E due to $\mathfrak{A}^0(E)$ which, however, affects only the time equation. Then, thanks to the second assumption there is a complete decoupling between the slow orbital elements and the fast time element.

Furthermore, thanks to the first hypothesis, the differential equations describing the slow orbital elements dynamics is 2π-periodic in E. As a result, system is of the form 4.6, therefore can be solved separately using periodic averaging.

Remark 4.5. Notice that Eq 4.12 offers the solution of $\boldsymbol{\vartheta}$ so, to recover $\delta\boldsymbol{\alpha}$, Eq. 4.10 shall be used. Incidentally, for slow orbital elements $\delta\boldsymbol{\alpha}_r$, one has $\delta\boldsymbol{\alpha}_r = \boldsymbol{\vartheta}_r$. △

4.4.1 Slow elements solution

For slow orbital elements we apply Section 4.2.1 which requires the solution of:

$$\begin{aligned} \frac{d\delta\bar{\boldsymbol{\alpha}}_r}{dE} &= \epsilon\left(\bar{\boldsymbol{f}}_{br}^1 + \boldsymbol{B}_r^1\delta\bar{\boldsymbol{\alpha}}_r\right) \\ \frac{\partial\delta\boldsymbol{\alpha}_r^{sp}}{\partial E} &= \epsilon\left(\boldsymbol{f}_{br}^1(E) - \bar{\boldsymbol{f}}_{br}^1\right) + \epsilon\left(\boldsymbol{A}^1(E) - \boldsymbol{B}_r^1\right)\delta\bar{\boldsymbol{\alpha}}_r \\ with \quad i.c. \quad & \delta\bar{\boldsymbol{\alpha}}_{r0} = -\delta\boldsymbol{\alpha}_r^{sp}(0) \end{aligned} \tag{4.13}$$

where $\bar{\boldsymbol{f}}_{br}^1$ represents the first five components of $\frac{1}{2\pi}\int_0^{2\pi}\boldsymbol{f}_b^1(E')dE'$, whereas $\boldsymbol{B}_r^1$ represents the upper-left 5×5 block matrix of $\frac{1}{2\pi}\int_0^{2\pi}\boldsymbol{A}^1(E')dE'$

The first of Eqs. 4.13 is a linear time invariant system, amenable of analytic solution. Care however, must be taken, as $\boldsymbol{B}_r^1$ can be in general singular.

A general solution can be outlined in terms of Jordan block decomposition. Using this decomposition $\boldsymbol{B}_r^1 = \boldsymbol{U}\boldsymbol{W}\boldsymbol{U}^{-1}$, where $\boldsymbol{U}$ is a non-singular matrix and $\boldsymbol{W}$ is a block diagonal matrix in the form:

$$\boldsymbol{W} = \begin{bmatrix} 0 & 0 \\ 0 & \boldsymbol{W}_r \end{bmatrix}$$

Then, using the fact that $e^{\boldsymbol{U}\boldsymbol{W}\boldsymbol{U}^{-1}} = \boldsymbol{U}e^{\boldsymbol{W}}\boldsymbol{U}^{-1}$, the solution to the differential equation is given by:

$$\delta\bar{\boldsymbol{\alpha}}_r = e^{\boldsymbol{B}_r^1 \epsilon E}\left(\delta\bar{\boldsymbol{\alpha}}_{r0} + \epsilon\boldsymbol{U}\int_0^E e^{-\boldsymbol{W}\epsilon E'}\,dE'\boldsymbol{U}^{-1}\bar{\boldsymbol{f}}_{br}^1\right), \tag{4.14}$$

leading to:

$$\delta\bar{\boldsymbol{\alpha}}_r = e^{\boldsymbol{B}_r^1 \epsilon E}\left(\delta\bar{\boldsymbol{\alpha}}_{r0} + \epsilon\boldsymbol{U}\begin{bmatrix} E\boldsymbol{I} & 0 \\ 0 & (\epsilon\boldsymbol{W}_r)^{-1}(\boldsymbol{I} - e^{-\boldsymbol{W}_r\epsilon E}) \end{bmatrix}\boldsymbol{U}^{-1}\bar{\boldsymbol{f}}_{br}^1\right)$$

The solution for the second of Eqs. 4.13 can be obtained taking advantage of the fact that we can integrate keeping $\delta\bar{\boldsymbol{\alpha}}_r$ constant (see Section 4.2.1):

$$\begin{aligned} \delta\boldsymbol{\alpha}_r^{sp} = {} & \epsilon\left(\mathfrak{f}_{br}^1(E) - \bar{\boldsymbol{f}}_{br}^1 E + \left(\mathfrak{A}_r^1(E) - \boldsymbol{B}_r^1 E\right)\delta\bar{\boldsymbol{\alpha}}_r\right) + \\ & - \frac{\epsilon}{2\pi}\int_0^{2\pi}\left(\mathfrak{f}_{br}^1(s) - \bar{\boldsymbol{f}}_{br}^1 s + \left(\mathfrak{A}_r^1(s) - \boldsymbol{B}_r^1 s\right)\delta\bar{\boldsymbol{\alpha}}_r\right)ds, \end{aligned} \tag{4.15}$$

where $\mathfrak{f}_{br}^1(E) = \int \boldsymbol{f}_{br}^1(s)ds$, $\mathfrak{A}_r^1(E) = \int \boldsymbol{A}_r^1(s)ds$ and the rightmost integral constant is included to ensure a null-average of the short-period.

The indefinite integrals used above depend clearly on the perturbing acceleration $\boldsymbol{b}(E, \boldsymbol{\alpha})$, so that a general expression is again not possible. For the existence of an analytical form, we have to consider the functions $\boldsymbol{b}(E, \boldsymbol{\alpha})$ such that $\boldsymbol{f}_{br}^1$ and $\boldsymbol{A}^1$ can be integrated analytically.

4.4.2 Fast element solution

For the fast orbital element we can apply Section 4.2.2. In fact, because of the separation between fast and slow variables we are provided with an average solution $\delta\bar{\alpha}_r = \bar{\boldsymbol{\vartheta}}_r$ (see previous section), which can be used to approximate the dynamics of the last row in Eq 4.12, by replacing $\boldsymbol{\vartheta}$ with $\bar{\boldsymbol{\vartheta}}$. That is:

$$\frac{d\vartheta_6}{dE} = \epsilon \begin{bmatrix} -\mathfrak{A}^0_{61} & -\mathfrak{A}^0_{62} & \dots & 1 \end{bmatrix} \left(\boldsymbol{f}^1_b(E) + \boldsymbol{A}^1(E) \begin{bmatrix} \delta\bar{\boldsymbol{\alpha}}_r(E) \\ 0 \end{bmatrix} \right)$$

Or, by using the symbols h^0 and $\boldsymbol{h}^1$ for the sake of brevity:

$$\frac{d\vartheta_6}{dE} = \epsilon \left(h^0(E) + \boldsymbol{h}^1(E)\delta\bar{\boldsymbol{\alpha}}_r(E) \right)$$

The solution is simply:

$$\vartheta_6 = \epsilon \left(\int h^0(s)ds + \int \boldsymbol{h}^1(s)\delta\bar{\boldsymbol{\alpha}}_r(s)ds \right) + const, \tag{4.16}$$

Then the time element is recovered by applying the former change of variable that is:

$$\delta\tilde{t} = \begin{bmatrix} -\mathfrak{A}^0_{61} & -\mathfrak{A}^0_{62} & \dots & 1 \end{bmatrix} \boldsymbol{\vartheta}$$

Integrating Eq. 4.16 is actually not easy because $\delta\bar{\boldsymbol{\alpha}}_r(s)$ is an exponential function multiplying a non-periodic function. Such integration can be however approximated leveraging the small parameter ϵ.

To this end, we integrate by parts the rightmost term of Eq. 4.16 using $\mathfrak{h}^0 = \int h^0(s)ds$ and $\boldsymbol{\mathfrak{h}}^1 = \int \boldsymbol{h}^1(s)ds$ to obtain:

$$\begin{aligned} \vartheta_6 = {} & \epsilon \left(\mathfrak{h}^0(E) + \left(\boldsymbol{\mathfrak{h}}^1(E) + c_h \right) \delta\bar{\boldsymbol{\alpha}}_r(E) \right) + \\ & - \epsilon \int \left(\boldsymbol{\mathfrak{h}}^1(s) + c_h \right) \delta\dot{\bar{\boldsymbol{\alpha}}}_r(s)ds + const, \end{aligned} \tag{4.17}$$

where by substituting the expression for $\delta\dot{\bar{\boldsymbol{\alpha}}}_r$

$$\begin{aligned} \vartheta_6 = {} & \epsilon \left(\mathfrak{h}^0(E) + \left(\boldsymbol{\mathfrak{h}}^1(E) + c_h \right) \delta\bar{\boldsymbol{\alpha}}_r(E) \right) + \\ & - \epsilon^2 \int \left(\boldsymbol{\mathfrak{h}}^1(s) + c_h \right) \left(\bar{\boldsymbol{f}}^1_r + \boldsymbol{B}^1_r \delta\bar{\boldsymbol{\alpha}}_r(s) \right) ds + const \end{aligned}$$

As we start from null initial condition of slow orbital elements, we have that $\delta\bar{\boldsymbol{\alpha}}_r(E))$ is of order ϵ. Then if we would like to retain up to second order in ϵ, the following approximation is obtained:

$$\vartheta_6 = \epsilon \left(\mathfrak{h}^0(E) + \boldsymbol{\mathfrak{h}}^1(E)\delta\bar{\boldsymbol{\alpha}}_r(E)\right) - \epsilon^2 \int \boldsymbol{\mathfrak{h}}^1(s)ds\bar{\boldsymbol{f}}^1_{br} + const$$

which is now more tractable, provided that the primitives $\mathfrak{h}^0(E)$, $\boldsymbol{\mathfrak{h}}^1(E)$, $\int \boldsymbol{\mathfrak{h}}^1(s)ds$ can be obtained. This will indeed be the case for the application scenario of a constant tangential acceleration.

Remark 4.6. Retaining higher order terms in ϵ here does not produce a higher order expansion of the averaging problem. Merely, the integral in Eq. 4.16 is computed with more precision. We decide to retain up to second order because such integral is itself an approximated solution of "quasi linear" order (see section 4.2.2), △

4.5 Application to constant tangential acceleration

In this section we apply the previous solution method to the case of a spacecraft subjected to a small constant tangential acceleration $\boldsymbol{b}(E, \boldsymbol{\alpha}) = [0\ 1\ 0]^T$. Notice that, mathematically this is a very special periodic perturbation independent of both E and $\boldsymbol{\alpha}$.

This case is of particular interest for spacecraft equipped with low thrust propulsion systems. In fact, as we have seen from literature in Section 3.3, the tangential maneuver is a nearly-optimal collision avoidance maneuver.

By applying to non-dimensional GPE the linearization methodology outlined in section 4.3, we obtain a first-stage linearization:

$$\frac{d\delta\boldsymbol{\alpha}}{dE} = \begin{bmatrix} 0 \\ 0 \\ 0 \\ 0 \\ 0 \\ a^{3/2}(1 - e\cos E) \end{bmatrix} + \epsilon \begin{bmatrix} 2\tilde{a}^3\sqrt{1 - e^2\cos^2 E} \\ 2\tilde{a}^2(1 - e^2)\sqrt{\frac{1 - e\cos E}{1 + e\cos E}}\cos E \\ 0 \\ 0 \\ 2\tilde{a}^2\frac{\sqrt{1-e^2}}{e}\sqrt{\frac{1 - e\cos E}{1 + e\cos E}}\sin E \\ \tilde{a}^{3/2}(1 - e\cos E)\beta(E) \end{bmatrix}, \tag{4.18}$$

where $\beta(E) = \frac{2\tilde{a}^2}{e}\sqrt{\frac{1 - e\cos E}{1 + e\cos E}}\sin E$.

It is possible to recognize the form in Eq. 4.7 by noticing that $\boldsymbol{f}^0(E, \boldsymbol{\alpha})$ is the first

addendum of the right hand side and $\boldsymbol{f}_b^1(E,\boldsymbol{\alpha})$ the second one.
To apply the second-stage linearization we need the gradient of both $\boldsymbol{f}^0(E,\boldsymbol{\alpha})$ and $\boldsymbol{f}_b^1(E,\boldsymbol{\alpha})$. The former was given in Eq. 4.9, whereas the second can be computed yielding:

$$\begin{gathered}
\frac{\partial \boldsymbol{f}_b^1}{\partial \tilde{a}} = \begin{bmatrix} 6\tilde{a}^2\sqrt{1-e^2\cos^2 E} \\ 4\tilde{a}(1-e^2)\sqrt{\frac{1-e\cos E}{1+e\cos E}}\cos E \\ 0 \\ 0 \\ \frac{4\tilde{a}\sqrt{1-e^2}}{e}\sqrt{\frac{1-e\cos E}{1+e\cos E}}\sin E \\ \frac{7\tilde{a}^{5/2}}{e}(1-e\cos E)\sqrt{\frac{1-e\cos E}{1+e\cos E}}\sin E \end{bmatrix} \\
\frac{\partial \boldsymbol{f}_b^1}{\partial e} = \begin{bmatrix} -2\tilde{a}^3\frac{e\cos^2 E}{\sqrt{1-e^2\cos^2 E}} \\ -2\tilde{a}^2\sqrt{\frac{1-e\cos E}{1+e\cos E}}\cos E\left[2e+(1-e^2)\frac{\cos E}{1-e^2\cos^2 E}\right] \\ 0 \\ 0 \\ -\frac{2\tilde{a}^2}{e\sqrt{1-e^2}}\sqrt{\frac{1-e\cos E}{1+e\cos E}}\sin E\left[\frac{1}{e}+\frac{\cos E}{1-e^2\cos^2 E}\right] \\ -\frac{2a^{7/2}}{e^2}\sqrt{\frac{1-e\cos E}{1+e\cos E}}\frac{1+2e\cos E}{1+e\cos E}\sin E \end{bmatrix}
\end{gathered} \tag{4.19}$$

The partial derivatives with respect to the remaining orbital elements are instead null given the tangential perturbation.
Notice also that when evaluated at chief orbit $\boldsymbol{\alpha}_c$, we have $\tilde{a}=1$.

Finally, to use the same notation as in section 4.3, we have

- $\boldsymbol{f}_b^1(E)$ given by the second column vector of $\boldsymbol{f}^1$ in Eq. 4.7 evaluated at $\boldsymbol{\alpha}_c$
- $\boldsymbol{A}^0(E)$ still given by Eq. 4.9 evaluated at $\boldsymbol{\alpha}_c$
- $\boldsymbol{A}^1(E)$ given by the column vectors in Eqs. 4.19 evaluated at $\boldsymbol{\alpha}_c$

To obtain the analytical approximation of the solution we need to compute the integrals outlined in section 4.4, that is:

$$\begin{aligned}
\mathfrak{f}_b^1 &= \int \boldsymbol{f}_b^1(E)dE \\
\mathfrak{A}^1 &= \int \boldsymbol{A}^1(E)dE \\
\mathfrak{h} &= \int h^0(E)dE \\
\boldsymbol{\mathfrak{h}}^1 &= \int \boldsymbol{h}^1(E)dE \\
&\int \boldsymbol{\mathfrak{h}}^1 dE
\end{aligned} \tag{4.20}$$

Furthermore, from the first two of the above one can easily compute the averaged counterparts $\bar{\boldsymbol{f}}_{br}^1$ and B_r^1, required for obtaining the average solution Eq. 4.14.

4.5.1 Partial indefinite integral of GPE

The analytic primitive $\mathfrak{f}_b^1 = [\delta\widetilde{a}^I, \delta e^I, \delta i^I, \delta\Omega^I, \delta\omega^I, \delta\widetilde{t}^I]$, read:

$$\begin{aligned}
\delta\widetilde{a}^I(E) &= 2\epsilon\sqrt{1-e_c^2}\,\mathbb{E}[E,\mathsf{k}] \\
\delta e^I(E) &= 2\epsilon\frac{1-e_c^2}{e_c}\left\{\frac{1}{2}ln\frac{\sqrt{1-e_c^2\cos^2 E}+e_c\sin E}{\sqrt{1-e_c^2\cos^2 E}-e_c\sin E}\right. \\
&\qquad\left.-\frac{1}{\sqrt{1-e_c^2}}\mathbb{F}\left[E,\mathsf{k}\right]+\sqrt{1-e_c^2}\,\mathbb{E}\left[E,\mathsf{k}\right]\right\} \\
\delta\omega^I(E) &= 2\epsilon\frac{\sqrt{1-e_c^2}}{e_c}\left(2\arcsin\sqrt{\frac{1-e_c\cos E}{2}}-\sqrt{1-e_c^2\cos^2 E}\right)\Bigg|_0^E \\
\delta\widetilde{t}^I(E) &= -\frac{\epsilon}{e_c^2}\left(\sqrt{\frac{1+e_c\cos E}{1-e_c\cos E}}\left(e_c^2\cos^2 E-5e_c\cos E+4\right)+\right. \\
&\qquad\left.-6\arcsin\sqrt{\frac{1-e\cos E}{2}}\right)\Bigg|_0^E,
\end{aligned} \tag{4.21}$$

where $\mathsf{k} = \frac{e_c^2}{(e_c^2-1)}$ and $\mathbb{F}$ and $\mathbb{E}$ are respectively the elliptic integrals of first and second kind. We skipped the equations for δi^I and $\delta\Omega^I$ because a tangential thrust has no effect on them. Note that the first three equations were first obtained by Gonzalo et al. (2019), whose work is highly acknowledged.

4.5.2 Partial indefinite integral of GPE gradient

The analytic primitive $\boldsymbol{A}^1(E)$ can be written as:

$$\mathfrak{A}^1 = \left[\int \left. \frac{\partial \boldsymbol{f}_b^1(\boldsymbol{\alpha},E)}{\partial \widetilde{a}} \right|_{\boldsymbol{\alpha}_c} dE \quad \int \left. \frac{\partial \boldsymbol{f}_b^1(\boldsymbol{\alpha},E)}{\partial e} \right|_{\boldsymbol{\alpha}_c} dE \quad \mathbf{0}_{6\times 4} \right]$$

The first term of the right hand side easily follows from partial indefinite integrals of GPE (Eq. 4.21), yielding:

$$\int \left. \frac{\partial \boldsymbol{f}\left(\boldsymbol{\alpha},E\right)}{\partial \widetilde{a}} \right|_{\boldsymbol{\alpha}_c} dE = \begin{bmatrix} 3\delta a^I\left(E\right) \\ 2\delta e^I\left(E\right) \\ 0 \\ 0 \\ 2\delta\omega^I\left(E\right) \\ \frac{3}{2}\left(E - e_c \sin\left(E\right)\right) + \frac{7}{2}\delta t^I\left(E\right) \end{bmatrix}$$

The second term of the right hand side is instead given below term by term:

$$\begin{aligned}
\mathfrak{A}^1_{12} &= -2e_c\epsilon\frac{\left(\mathbb{F}\left[E|\mathsf{k}\right] + \left(e_c^2-1\right)\mathbb{E}\left[E|\mathsf{k}\right]\right)}{e_c^2\sqrt{1-e_c^2}} \\
\mathfrak{A}^1_{22} &= -\frac{2e_c}{\left(1-e_c^2\right)}\delta e^I\left(E\right) + \\
&\qquad - 2\epsilon\left(1-e_c^2\right)\int\frac{\cos^2 E}{\sqrt{1-e_c^2\cos^2 E}\left(1+e_c\cos E\right)}dE \\
\mathfrak{A}^1_{32} &= \mathfrak{A}^1_{42} = 0 \\
\mathfrak{A}^1_{52} &= -\frac{2\epsilon}{e_c\sqrt{1-e_c^2}}\left(\frac{2\arcsin\sqrt{\frac{1-e_c\cos E}{2}} - \sqrt{1-e_c^2\cos^2 E}}{e_c^2} + \right. \\
&\qquad \left. -\frac{\arcsin\left(e_c\cos E\right) + \sqrt{\frac{1-e_c\cos E}{1+e_c\cos E}}}{e_c^2}\right) \\
\mathfrak{A}^1_{62} &= \frac{4\epsilon}{e_c^3}\left(\sqrt{\frac{1-e_c\cos E}{1+e_c\cos E}}\left(2+e_c\cos E\right) + \right. \\
&\qquad \left. 3\arcsin\sqrt{\frac{1-e_c\cos E}{2}}\right)
\end{aligned} \tag{4.22}$$

The integral in the equation for $\mathfrak{A}^1_{22}$ can be computed using the change of variable

$$H = 2\arctan\left(\sqrt{\frac{1-e_c}{1+e_c}}\tan\left(\frac{E}{2}\right)\right) \quad\rightarrow\quad \frac{dH}{dE} = \frac{\sqrt{1-e_c^2}}{1+e_c\cos E}$$

In fact, noticing that $\cos E = \frac{\cos H - e_c}{1-e_c\cos H}$, we can write:

$$\begin{aligned}\int \frac{\cos^2 E}{\sqrt{1-e_c^2\cos^2 E}\,(1+e_c\cos E)}dE = \\ \frac{1}{\sqrt{1-e_c^2}}\int\frac{(\cos H - e_c)^2}{(1-e_c\cos H)\sqrt{(1-e_c^4)\,(1-\mathsf{m}\cos H)}}dH,\end{aligned} \tag{4.23}$$

with $\mathsf{m} = \frac{2e_c}{1+e_c^2}$.
The right hand side is then the sum of:

$$\begin{aligned}&\frac{1}{\sqrt{1-e_c^4}}\int\frac{(1+e_c^2)/e_c^2}{(1-e_c\cos H)\sqrt{1-\mathsf{m}\cos H}}dH = \frac{(1+e_c^2)/e_c^2}{\sqrt{1-e_c^4}}\,2\,\frac{\mathbb{\Pi}\left[\frac{2e_c}{e_c-1};\frac{H}{2}\middle|\frac{2\mathsf{m}}{\mathsf{m}-1}\right]}{(1-e_c)\sqrt{1-\mathsf{m}}}\\ &\frac{-1/e_c^2}{\sqrt{1-e_c^4}}\int\frac{1+e_c\cos H}{\sqrt{1-\mathsf{m}\cos H}}dH = \frac{-\frac{1}{e_c^2}}{\sqrt{1-e_c^4}}\frac{2}{\mathsf{m}\sqrt{1-\mathsf{m}}}\times\\ &\qquad\left((e_c+\mathsf{m})\,\mathbb{F}\left[\frac{H}{2}\middle|\frac{2\mathsf{m}}{\mathsf{m}-1}\right] + e_c\,(\mathsf{m}-1)\,\mathbb{E}\left[\frac{H}{2}\middle|\frac{2\mathsf{m}}{\mathsf{m}-1}\right]\right)\\ &\frac{1+e_c^2}{\sqrt{1-e_c^4}}\int\frac{\sqrt{1-\mathsf{m}\cos H}}{1-e_c\cos H}dH = \frac{1+e_c^2}{\sqrt{1-e_c^4}}\frac{2}{e_c\,(e_c-1)\,\sqrt{1-\mathsf{m}}}\times\\ &\qquad\left(\mathsf{m}\,(e_c-1)\,\mathbb{F}\left[\frac{H}{2}\middle|\frac{2\mathsf{m}}{\mathsf{m}-1}\right] + (\mathsf{m}-e_c)\,\mathbb{\Pi}\left[\frac{2e_c}{e_c-1};\frac{H}{2}\middle|\frac{2\mathsf{m}}{\mathsf{m}-1}\right]\right)\end{aligned} \tag{4.24}$$

which can be obtained with the aid of bisection formulae.

4.5.3 Indefinite integral of h^0

$$\mathfrak{h}^0 = \int h^0(E)dE = \int -\mathfrak{A}^0_{61}f^1_{b1}\,(E) - \mathfrak{A}^0_{62}f^1_{b2}\,(E) + f^1_{b6}\,(E)\,dE \tag{4.25}$$

In performing such integration, the identities in Chapter Appendix 4.6.3 are used to give:

$$\begin{aligned}
&\int -\mathfrak{A}^0_{62} f_{b1}\left(E\right)dE = \epsilon\left(1-e_c^2\right)\ 2\ I_{sc}\\
&\int -\mathfrak{A}^0_{61} f_{b2}\left(E\right)dE \cong -\frac{3}{2}\epsilon\left(E^2 - e_c^2\ I_{c2} - \frac{e_c^4}{4}I_{c4}\right) + 3\epsilon e_c I_s,
\end{aligned} \tag{4.26}$$

where to write the second equation, an expansion of the elliptic integral is used to integrate terms of the type $E\mathbb{E}[E,\cdot]$.
The last integral in Eq. 4.25 coincides with $\widetilde{\delta t}^{I}\left(E\right)$ already given in Section 4.5.1.

4.5.4 Indefinite integral of $\boldsymbol{h}^1$

The next integral we need for the envisaged solution is:

$$\mathfrak{h}^1 = \int \boldsymbol{h}^1 dE = \begin{bmatrix} \int -\mathfrak{A}^0{}_{61}A^1_{11} - \mathfrak{A}^0{}_{62}A^1_{21} + A^1_{61}dE \\ \int -\mathfrak{A}^0{}_{61}A^1_{12} - \mathfrak{A}^0{}_{62}A^1_{22} + A^1_{62}dE \end{bmatrix}^T$$

The integral involving the term $\mathfrak{A}^0{}_{61}$ imposes the use of the expansion for the elliptic functions as given in Chapter Appendix 4.6.3, to obtain:

$$\begin{aligned}
&\int -\mathfrak{A}^0_{61}A^1_{11}\left(E\right)dE = -9\epsilon\left(\frac{E^2}{2} - \frac{e_c^2}{2}I_{c2} - \frac{e_c^4}{8}I_{c4}\right) + 9\epsilon e_c I_s\\
&\int -\mathfrak{A}^0_{61}A^1_{12}\left(E\right)dE = 3\epsilon e_c\left(I_{c2} + \frac{e_c^2}{2}I_{c4} + \frac{e_c^4}{8}I_{c6}\right) - 3\epsilon e_c^2 I_{sc3},
\end{aligned} \tag{4.27}$$

whereas the ones involving $\mathfrak{A}^0{}_{62}$ results to be

$$\begin{aligned}
&\int -\mathfrak{A}^0_{62}A^1_{21}\left(E\right)dE = 4(1-e_c^2)\epsilon I_{sc}\\
&\int -\mathfrak{A}^0_{62}A^1_{22}\left(E\right)dE = -2\epsilon\left(2e_c I_{sc} + \left(1-e_c^2\right)\ I_{sc2}\right),
\end{aligned} \tag{4.28}$$

where we made use of the recurrent integrals given in Chapter Appendix 4.6.3. The two integrals involving A^1_{61} and A^1_{62} only were already given in Section 4.5.2, i.e. $\mathfrak{A}^1_{61}$ and $\mathfrak{A}^1_{62}$.

The last integral we need is $\int \mathfrak{h}^1 dE$. Let us start by the two parts involving the double integration of A^1_{61} and A^1_{62} alone, the former reads:

$$
\begin{aligned}
\int \mathfrak{A}^1_{61} dE = & \frac{7}{2}\left[-\frac{4\epsilon}{e_c^2}\int\sqrt{\frac{1+e_c\cos E}{1-e_c\cos E}}dE+\right. \\
& +\frac{5\epsilon}{e_c}\int\sqrt{\frac{1+e_c\cos E}{1-e_c\cos E}}\cos E dE-\epsilon\int\sqrt{\frac{1+e_c\cos E}{1-e_c\cos E}}\cos^2 E dE+ \\
& \left.+\frac{6\epsilon}{e_c^2}\int\arcsin\sqrt{\frac{1-e_c\cos E}{2}}dE\right] \\
= & \frac{7}{2}\left[-\frac{4\epsilon}{e_c^2}\left(I_{c0F}+e_c\,I_{c1F}\right)+\frac{5\epsilon}{e_c}\left(I_{c1F}+e_c\,I_{c2F}\right)dE+\right. \\
& \left.-\epsilon\left(I_{c2F}+e_c I_{c3F}\right)+\frac{6\epsilon}{e_c^2}\left(E\arcsin\sqrt{\frac{1-e_c\cos E}{2}}-\frac{e_c}{2}I_{EsF}\right)\right]
\end{aligned}
$$

Then, similarly:

$$
\begin{aligned}
\int \mathfrak{A}^1_{62} dE = & \frac{4\epsilon}{e_c^3}\int\left(\sqrt{\frac{1-e_c\cos E}{1+e_c\cos E}}\left(2+e_c\cos E\right)+3\arcsin\sqrt{\frac{1-e_c\cos E}{2}}\right)dE \\
= & \frac{4\epsilon}{e_c^3}\Big[2\left(I_{c0F}-e_c\,I_{c1F}\right)+e_c\left(I_{c1F}-e_c\,I_{c2F}\right)+ \\
& +3\left(E\arcsin\sqrt{\frac{1-e_c\cos E}{2}}-\frac{e_c}{2}I_{EsF}\right)\Big]
\end{aligned}
$$

To complete $\int \mathfrak{h}^1 dE$, we need finally to perform the integration of the terms in

4.27 and 4.28. Then we need integrals:

$$
\begin{aligned}
\int I_{c2}dE &= \int \frac{E^2}{4} - \frac{\sin^2 E}{8} + \frac{\cos^2 E}{8} + \frac{E}{2}\sin E \cos E dE \\
\int I_{c4}dE &= \int \frac{3E^2}{16} + \frac{E\sin(2E)}{4} + \frac{E\sin(4E)}{32} + \\
&\qquad + \frac{\cos(2E)}{8} + \frac{\cos(4E)}{128} dE \\
\int I_{c6}dE &= \int \frac{5E^2}{32} + \frac{15E\sin(2E)}{64} + \frac{3E\sin(4E)}{64} + \\
&\qquad + \frac{E\sin(6E)}{192} + \frac{15\cos(2E)}{128} + \frac{3\cos(4E)}{256} + \frac{\cos(6E)}{1152} dE \\
\int I_{sc}dE &= \frac{-1}{2e_c^2} \int \left(\frac{-e_c^3\cos^3 E + 2e_c^2\cos^2 E + e_c\cos E - 2}{\sqrt{1-e_c^2\cos^2 E}} + \right. \\
&\qquad \left. +2\arcsin\sqrt{\frac{1-e_c\cos E}{2}} \right) dE \\
\int I_{sc2}dE &= \int \frac{1}{e_c^3} \left(\frac{\sqrt{1-e_c^2\cos^2 E}\,(2+e_c\cos E)}{1+e_c\cos E} + \right. \\
&\qquad \left. + \arcsin(e_c\cos E) \right) dE \\
\int I_{sc3}dE &= \int \frac{\cos E}{2e_c^2}\sqrt{1-e_c^2\cos^2 E} - \frac{\arcsin(e_c\cos E)}{2e_c^3} dE \\
\int I_s dE &= \int -\frac{\cos E}{2}\sqrt{1-e_c^2\cos^2 E} - \frac{\arcsin(e_c\cos E)}{2e_c} dE
\end{aligned}
\tag{4.29}
$$

Most of these integrals can be easily solved analytically by hand or by any symbolic manipulator. There are however two integrals that are not trivial, still they can be reduced to known integrals or approximated. One is:

$$\int \arcsin(e_c\cos E)dE \cong E\arcsin(e_c\cos E) + e_c\, I_{EsF},$$

where the recurrent integrals in Chapter Appendix 4.6.3 was used after integrating by parts.

The other is:

$$\int \cos E\sqrt{1-e_c^2\cos^2 E}dE = \frac{\sin E}{2}\sqrt{1-e_c^2\cos^2 E}+ \\ +(1-e_c^2)\frac{\operatorname{arsinh}\left(\frac{e_c}{\sqrt{1-e_c^2}}\sin E\right)}{2e_c},$$

where we first integrated by parts and then used the integral 630.11 from the handbook of elliptic integrals (Byard and Friedman, 1970).

4.5.5 Short-Period integration constant

The integration constant in Eq. 4.15 for the short period variations of the slow elements,

$$\frac{1}{2\pi}\int_0^{2\pi}\left(\mathfrak{f}^1_{br}(s)-\bar{\boldsymbol{f}}^1_{br}s+\left(\mathfrak{A}^1_r(s)-\boldsymbol{B}^1_r s\right)\delta\bar{\boldsymbol{\alpha}}_r\right)ds,$$

can be computed analytically using the completeness property of elliptic integrals and the symmetry of some integrand functions in the interval $[0,\ 2\pi]$.

Start from the integrand $\mathfrak{f}^1_{br}(s)-\bar{\boldsymbol{f}}^1_{br}s$. Since we are interested only in its first 5 elements, the only non-zero component is the fifth one.

In fact, the elliptic integrals of the first two equations of Eqs. 4.21 (a and e elements of $\mathfrak{f}^1_{br}(s)$) can be split between an exact linear drift in s which is compensated by $\bar{\boldsymbol{f}}^1_{br}s$ and a periodic component, which amounts to zero when integrated between $[0, 2\pi]$. Additionally, the symmetry of the function argument of the natural logarithm proves the claim.

On the other hand, the fifth component has to be integrated resulting in the sum of a complete elliptic integral contribution and a constant, $\pi/4$, from integration of the $\arcsin$ term. The latter conclusion can be easily obtained expanding the integrand in a Taylor series around null eccentricity. Then, integrating on the complete circle, only the 0-order term is not null, which amounts to $\pi/4$ for any

Table 4.1: Benchmark orbits for the target spacecraft

a [km]	e	i [°]	Ω [°]	ω [°]	E_0 [°]
8500	0.2	0	0	0	0

eccentricity. In summary:

$$\frac{1}{2\pi}\int_0^{2\pi} \mathfrak{f}^1_{br}(s) - \bar{\boldsymbol{f}}^1_{br} s ds = 2\frac{\sqrt{1-e_c^2}}{e_c}\begin{bmatrix} 0 \\ 0 \\ 0 \\ 0 \\ \pi/2 - \sqrt{1-e_c^2}\mathbb{E}[2\pi, \mathsf{k}]/(2\pi) \end{bmatrix}$$

For the integrand $\mathfrak{A}^1_r(s) - \boldsymbol{B}^1_r s$ similar arguments can be used to show that only the fifth row of the resulting matrix is not null. The integrals therein can be again calculated leveraging symmetry and the results collected in this Chapter Appendix (See section 4.6.3), to obtain:

$$\frac{1}{2\pi}\int_0^{2\pi} \mathfrak{A}^1_r(s) - \boldsymbol{B}^1_r s ds =$$

$$\frac{1}{2\pi}\begin{bmatrix} 0 & 0 & \dots \\ 0 & 0 & \dots \\ 0 & 0 & \dots \\ 0 & 0 & \dots \\ 4\frac{\sqrt{1-e_c^2}}{e_c}\left(\pi^2 - \sqrt{1-e_c^2}\mathbb{E}[2\pi, \mathsf{k}]\right) & -2\left(\frac{\pi^2 - \sqrt{1-e_c^2}\mathbb{E}[2\pi,\mathsf{k}]}{{e_c}^3\sqrt{1-e_c^2}} - \frac{\mathbb{F}[2\pi,\mathsf{k}]}{{e_c}^3(1-e_c^2)}\right) & \dots \end{bmatrix}$$

4.5.6 Model performance as position propagator

The accuracy of the obtained model has been assessed through numerical simulations. We took as a test case a reference LEO orbit with the initial elements reported in Table 4.1, considering a propagation interval of 5 orbits and a small constant-tangential acceleration of 1e-7km/s^2.
This reference case is then modified to test the sensitivity of the model to perturbation magnitude, semi-major axis and eccentricity.

Remark 4.7. Section 4.2 provides results for the error behavior that hold within an ϵ-dependent propagation interval, i.e. $0 < E < L/\epsilon$, with L some positive constant. Thus, when comparing results for different values of ϵ it may have sense to scale the propagation interval accordingly, rather than using a fixed number of orbits. Such a scaling, however, may lead to extremely small propagation horizons.

For instance, for an acceleration of 1e-5km/s^2, we would obtain a propagation interval of 0.05 orbits which is of low interest in low thrust collision avoidance. For this reason, we opted for retaining a fixed propagation interval throughout the entire analysis. △

The ground-truth solution has been obtained solving numerically Eq. 4.1 with MATLAB's built-in ode113 function.

The double-stage linearized form in Eq. 4.8 was solved numerically as well, to check the agreement between the full GPE and their linearization.

In fact, our method introduces two distinct levels of approximation:

- First, the model we seek to solve,(Eq. 4.8), is a simplification, through the dual-stage linearization, of the true one (Eq. 4.1).
  We call the resulting error an *intrinsic error*.
- Second, the developed solution method to the linearized model is by itself approximate, due to the application of averaging theory, introducing a further source of error.
  We call this latter *averaging error*.

Figure 4.1 depicts the errors with respect to the ground truth in the reference case for both intrinsic and global (intrinsic plus averaging) errors. The global error tracks reasonably closely the intrinsic error, meaning that we are solving the averaged problem accurately enough with respect to the limit set by the linearization process. This is especially true for semi-major axis and time elements. For relatively large perturbation forces however (see Figure 4.2), the prediction drifts apart from the linear solution, especially for the time element. This is expected as when the acceleration gets larger, the fundamental assumption of averaging technique degrades.

With reference to Figure 4.1, the drift of the intrinsic error on ω, resulting from the numerical integration of Eq. 4.8, is worth to be noted. Such an effect is originated by the approximation of the derivative $\left(\frac{dE}{dt}\right)^{-1}$ within the linearization process described in Section 4.3, and can be explained by inspecting higher order

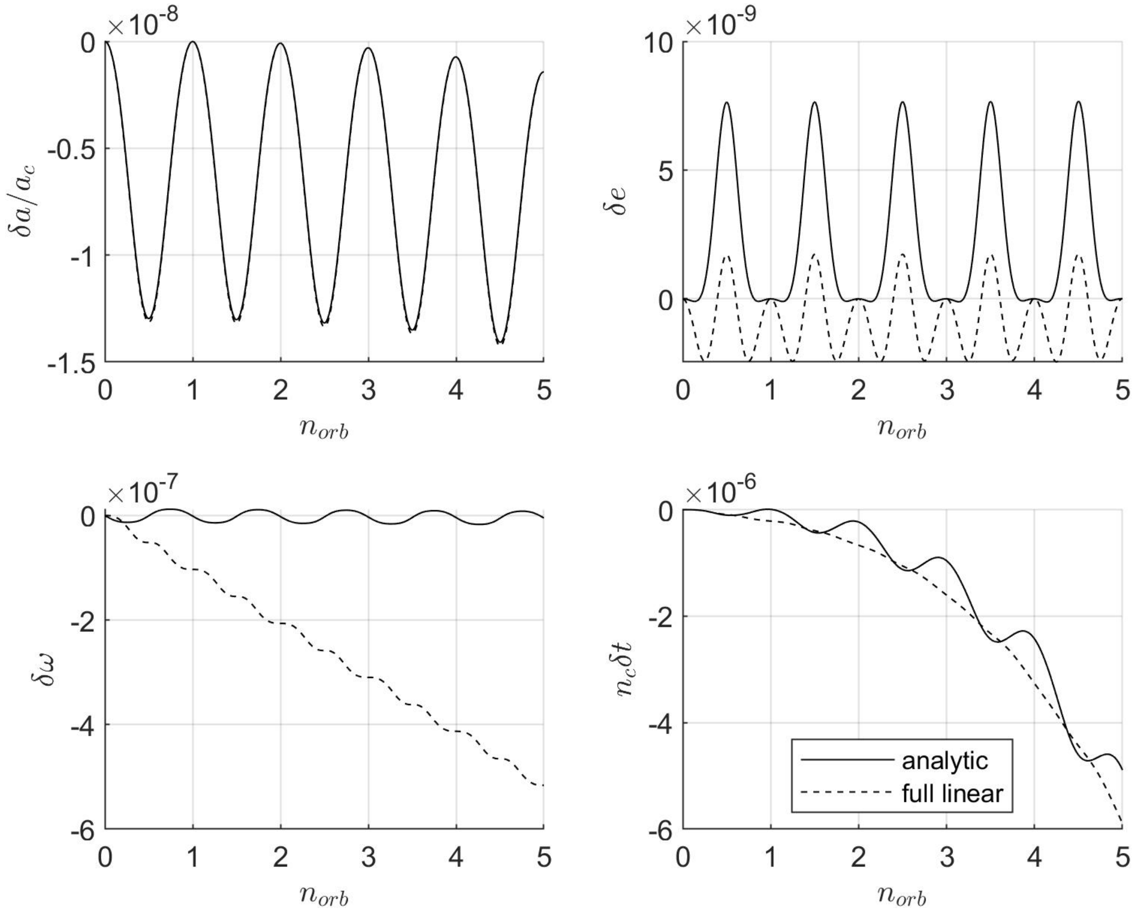

Figure 4.1: Non-dimensional errors of proposed solution and (numerically solved) linearized solution with respect to the ground truth on the reference orbit

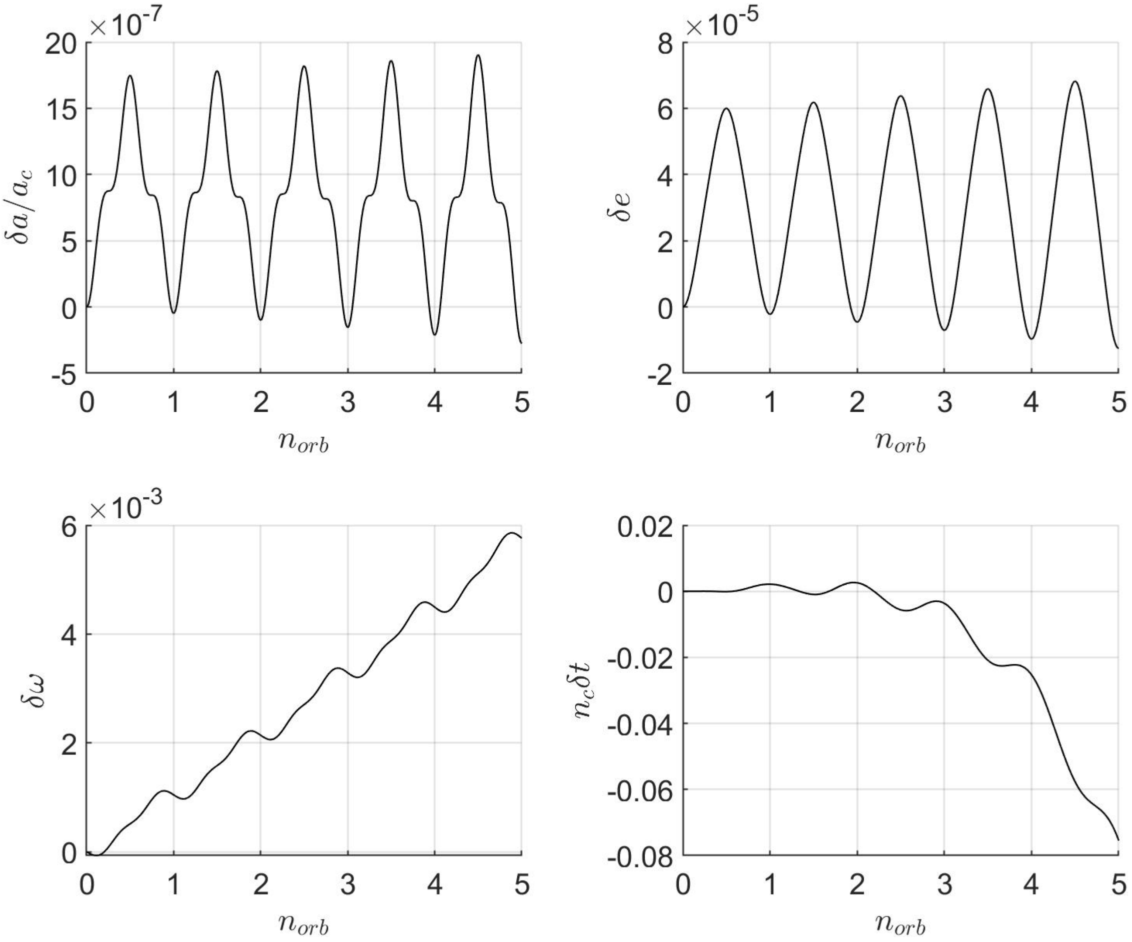

Figure 4.2: Non-dimensional errors of proposed solution with respect to the linear solution (averaging error) on the reference orbit with perturbing acceleration of 1e-5km/s^2

Table 4.2: Root mean square errors of orbital elements with respect to the ground truth varying tangential acceleration (non-dimensional form)

$\tilde{\boldsymbol{a}}_p$	$\delta\tilde{a}$	δe	$\delta\omega$	$\delta\tilde{t}$
1.812e-6 (1e-8$[\frac{km}{s^2}]$)	7.71e-11	3.50e-11	9.84e-11	2.23e-08
1.812e-5 (1e-7$[\frac{km}{s^2}]$)	7.99e-09	3.50e-09	9.86e-09	2.13e-06
1.812e-4 (1e-6$[\frac{km}{s^2}]$)	1.18e-06	3.59e-07	1.02e-06	2.43e-04
1.812e-3 (1e-5$[\frac{km}{s^2}]$)	8.31-04	5.50e-05	2.87e-04	6.20e-02

Table 4.3: Root mean square errors in radial and transversal components with respect to the ground truth varying tangential acceleration

$\boldsymbol{a}_p[\frac{km}{s^2}]$	$R[km]$	$T[km]$
1e-8	1.33e-4	1.35e-4
1e-7	1.26e-2	1.28e-2
1e-6	1.444	1.472
1e-5	349.1	371.7

terms which are neglected in the first-order expansion Eq. 4.18. In particular, the second order (ϵ^2) term is proportional to $\beta(E)\boldsymbol{f}_b^1(E)$. The resulting functions are periodic with zero mean for a, e derivatives, having instead non-zero mean for ω and t derivatives. Thus, error drifts arise upon integration of these latter. The effect is less visible for t element, since its derivative is dominated by the Keplerian part, $\boldsymbol{f}^0(E)$ in Eq. 4.7. As a result, the integration error is mostly affected by that of the semimajor axis used to evaluate $\boldsymbol{f}^0(E)$.

Table 4.2 reports the non-dimensional root mean square errors of the proposed averaged model with respect to the ground-truth solution. As expected, the accuracy degrades as the magnitude of the perturbing acceleration increases: a change of one order of magnitude in the perturbing acceleration causes a change of at least two orders of magnitude in a, e and ω. Notice also that the results in Table 4.2 are global errors, so the intrinsic error introduced by the linearization of GPE plays a role as well.

For collision avoidance applications, these errors would be more useful when expressed in the R-T-N frame of reference. Table 4.3 reports these errors for R and T cartesian components; N component is instead identically null, being the acceleration on the orbital plane.

Taking into consideration the results of Chapter 3, we can draw qualitative conclusion about the applicability of the model to conjunction assessment. If we

consider accurate enough a log-Pc error of 10% at 1σ level (i.e. 68% of conjunctions), the propagated position can be biased at most by half the positional bound in Section 3, i.e. 102 meters. As a consequence, we can reasonably say that the proposed model can be reliably used in LEO up to accelerations of about 1e-$7km/s^2$. For larger accelerations this model shall implement a covariance inflation strategy to account for model uncertainty.
Remind that this conclusion is contingent upon the specific simulation scenario, most significantly the 5 orbital periods of propagation and 8500 km semi-major axis.

We now consider the sensitivity of the proposed solution. We study the effect of varying the eccentricity and semi-major axis to the values in the sets $[0.2,\ 0.5,\ 0.8]$ and $[6800,\ 8500,\ 10200]$ respectively. Argument of pericenter and initial eccentric anomaly were not considered in this analysis, as they have negligible effects on the error.
Notice that these orbits have been chosen solely for evaluation purposes and some of them are not physically meaningful, e.g. orbit with 8500km semi-major axis and 0.8 eccentricity has pericenter below Earth's surface.
As it can be seen in Figure 4.3, changing the semi-major axis changes the orbital period and the error scales accordingly and almost proportionally. For this reason, the proposed solution can be said to be tolerant to changes in semi-major axis.
Figure 4.4 instead shows the behavior of the proposed model changing the eccentricity. Here we can distinguish two characteristics, from one side the average behavior seems quite stable varying the eccentricity except for the time element. This is due to the fact that in approximating an analytic solution for the time element, Taylor expansions around null eccentricity was used. The error committed in this expansion, although precise, becomes larger as the eccentricity gets further from 0.
The second comment regards the increasing oscillations as the eccentricity approaches 0. Figure 4.5 helps understanding that this behavior is inherent to the linearization of the true orbital model (intrinsic error) and not to the approximation made for solving that linear model (averaging error). The behaviour can be adduced to the singularity of the adopted orbital elements for null eccentricity, whereby the gradient becomes numerically very large amplifying errors in the

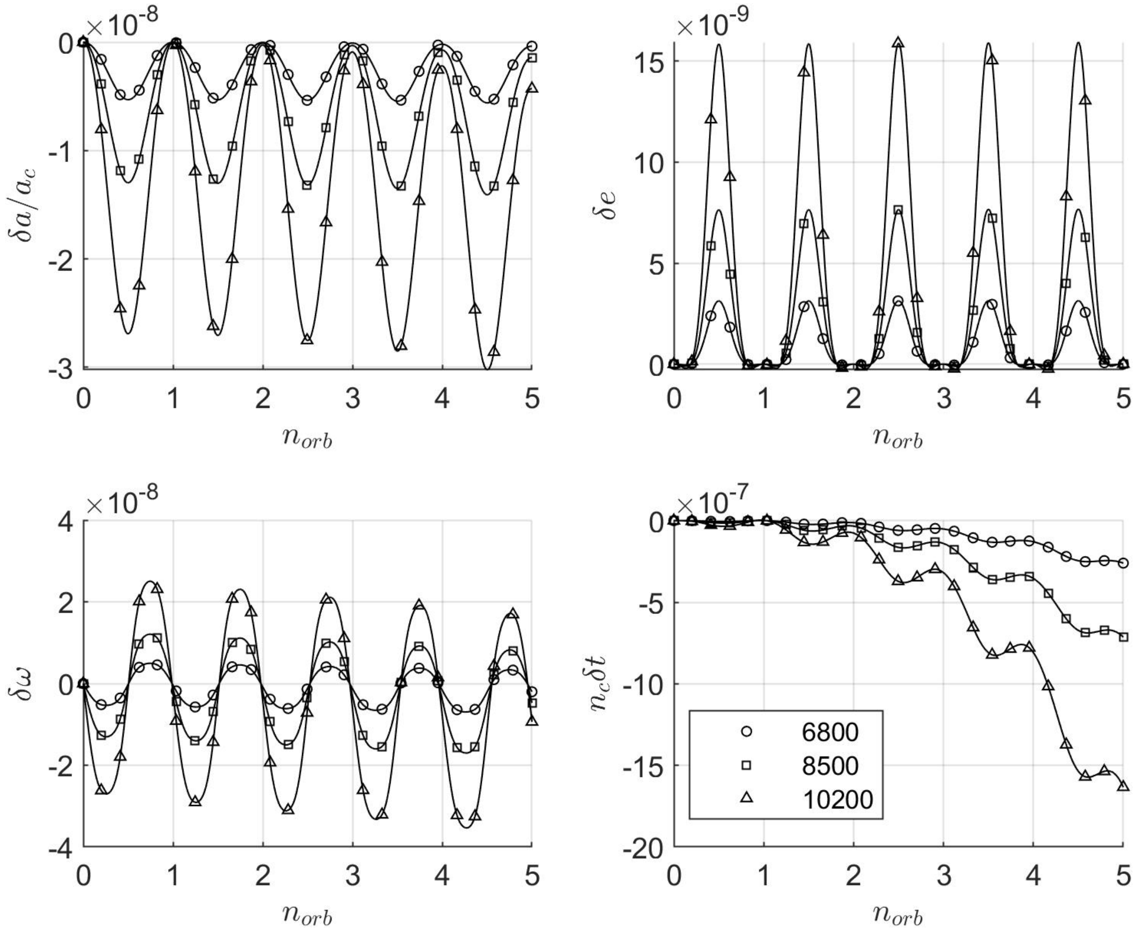

Figure 4.3: Non-dimensional errors of proposed solution with respect to the ground truth on the reference orbit changing semi-major axis

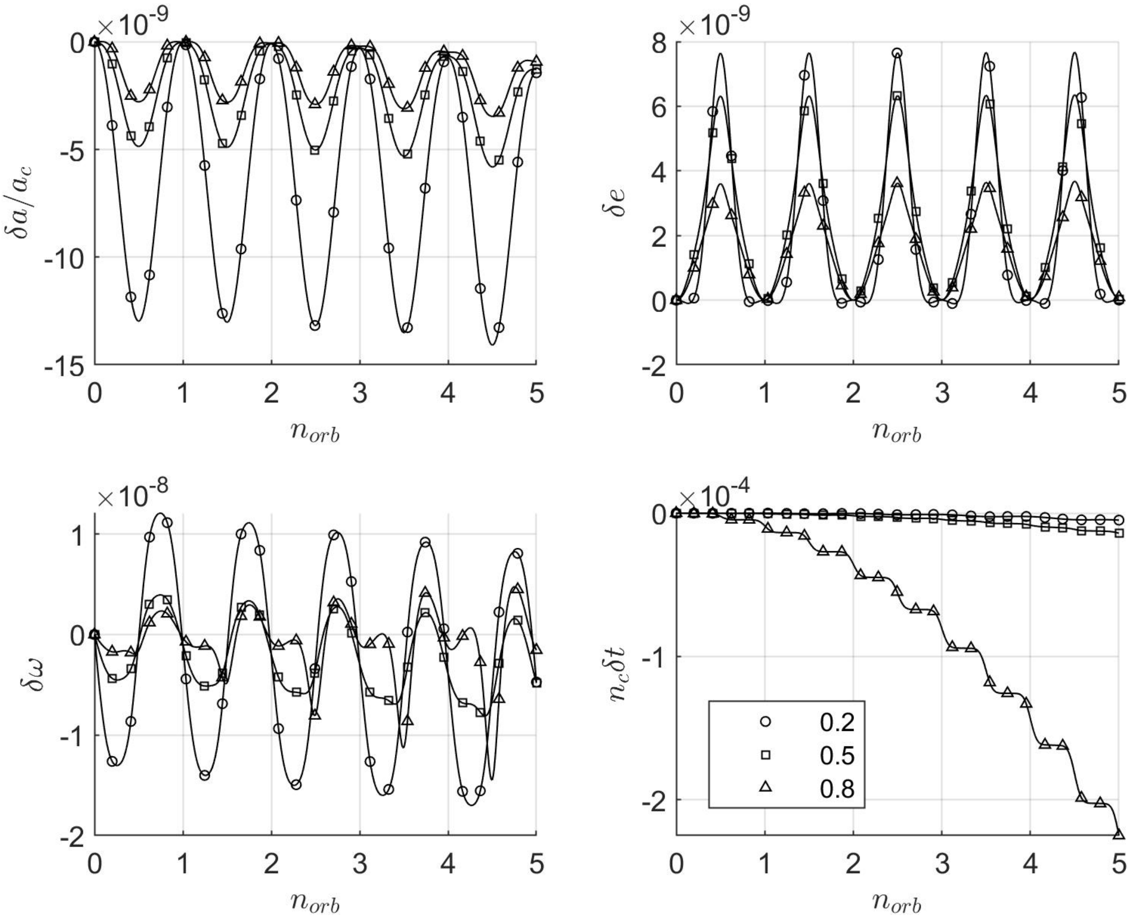

Figure 4.4: Non-dimensional errors of proposed solution with respect to the ground truth on the reference orbit changing eccentricity

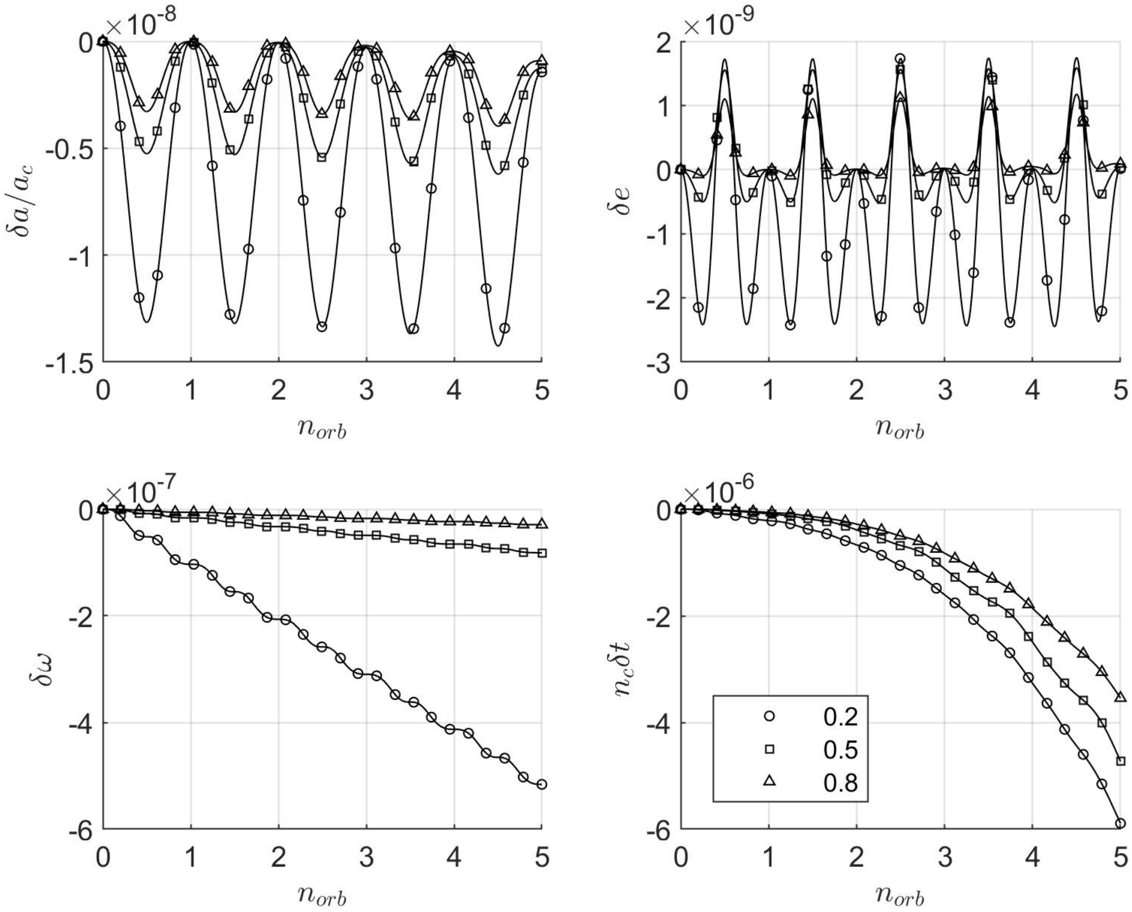

Figure 4.5: Non-dimensional intrinsic errors with respect to the ground truth on the reference orbit changing eccentricity, i.e. error between linearized model and ground truth

orbital elements.

To compare the solution method developed herein with state of the art, we simulated the reference case also with the models from Bombardelli et al. (2011) and Gonzalo and Colombo (2021), for simplicity referred as Bombardelli's method and Gonzalo's method respectively.

Figure 4.6 shows the model proposed herein accurately tracking the average trend of the orbital elements. The semi-major axis is experiencing the best improvement reducing the error by two orders of magnitude. The improvements of the other orbital elements amount to about one order of magnitude.

Overall, the rms value of the position error magnitude along the entire propagation interval reduces from 183.9 and 116.5 meters obtained respectively from

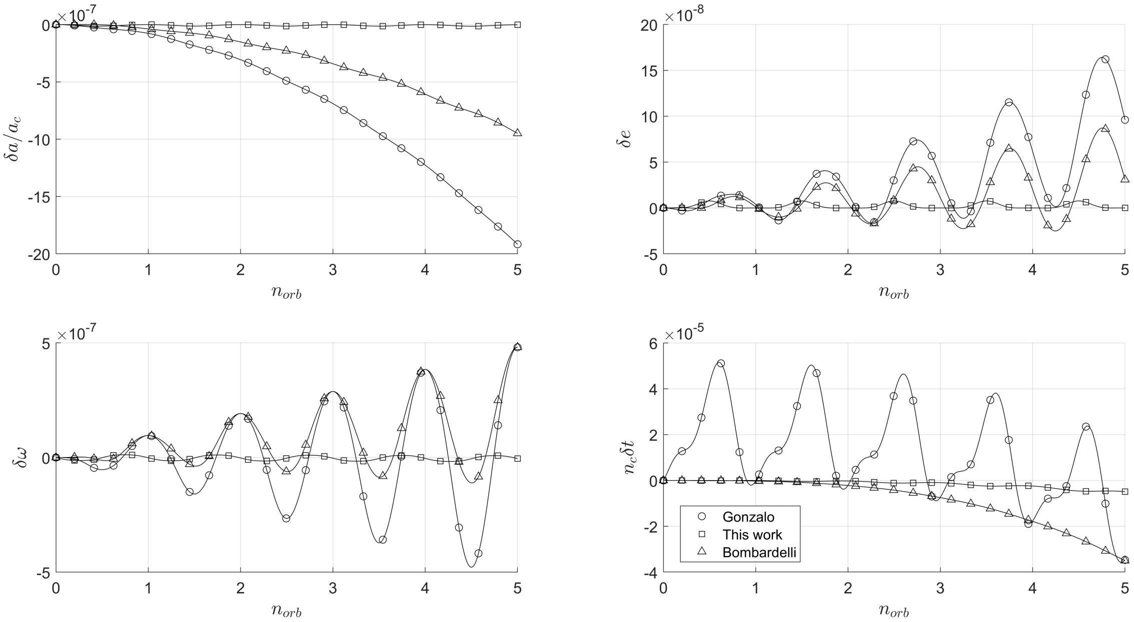

Figure 4.6: Non-dimensional errors of proposed (linear), Bombardelli's and Gonzalo's solutions with respect to the ground truth on the reference test case

Gonzalo's and Bombardelli's methods down to 18.0 meters. The largest error being on the tangential component which still reduces from 139.3 and 84.3 to 12.8 meters respectively.

Comparing more in details the results, one can appreciate that the present method offers the largest improvement on the semi-major axis and eccentricity elements. This is a beneficial effect of including the averaged gradient term, $\boldsymbol{B}_r^1$, in the average solution (see Eq. 4.13).

Furthermore the errors in eccentricity and argument of pericenter exhibit a sensible decrease in the oscillatory behavior. This is again a benefit of the linearization step which allows the short period solution to account also for accelerations arising from the gradient of the system dynamics.

Looking at the time element, improvements can be found both in the secular and periodic components of the error. The key advantage of our method in this case does not reside in the linearization of the GPE time-component, rather in the more accurate modelling of the semi-major axis. In fact, the latter appears in the GPE time law in a non-linear form and more importantly non-proportionally to the perturbation ϵ.

In addition, it is worth to be noted that a disadvantage exist that is shared by all the methods. In collision avoidance, we typically work with positions (e.g.

Table 4.4: Non-dimensional execution time for the different methods with respect to the fastest.

Method	Time
Numeric	45.3
Gonzalo	1.2
Bombardelli	1
This	5.6

anomaly) at given times, while the above models provide times at given anomalies. In case there is no possibility to work in a framework with anomaly as independent variable, this implies an iterative procedure to find the position at a given time.

Lastly, we compare the computational burden of the proposed analytical model with respect to state of the art. In order to make such comparison we considered the base scenario in Table 4.1 always with the same tangential perturbation and 5-orbit propagation length.
We compared to the proposed method other three methods: the numeric method using the Matlab's ode113 commands (a variable-step, variable-order Adams-Bashforth-Moulton Predict–Evaluate–Correct–Evaluate solver of orders 1 to 13), Bombardelli and Gonzalo. We acknowledge that other efficient numeric solvers exist that have been used in orbital mechanics, such as Livermore Solver for Ordinary Differential equations with Automatic Root-findingi.e., LSODAR (Amato et al., 2018), but differences are not expected to be significant given the relatively short integration window (few orbits). For the numeric method to be comparable, we fixed the convergence tolerance to a relative value of 1e-6, which is in the order of the error for the proposed model.
For the results not to depend from the machine hardware, we report in Table 4.4 the non-dimensional execution time using as a reference value the fastest among the methods i.e., Bombardelli.

It can be concluded that the proposed method is heavier than the analogous models proposed in the literature, which is a price to be paid for the increased accuracy. This is expected as our model uses matrix exponential functions and needs to evaluate a total of 15 elliptic integrals against the 3 of Gonzalo's method, which are computationally intensive routines.
Still, it retains a sensible advantage on the numerical integration, by running

roughly 10 times faster.

4.5.7 Model performance as uncertainty propagator

As discussed in Chapter 3, a trajectory propagator to be adopted for COLA shall fulfill accuracy requirements also in terms of positional covariance. To measure accuracy of the proposed model in this sense, we take as a use case the base scenario of the previous Section 4.5.6. In this case, based on Section 2.3, we shall additionally make the gaussian assumption for the initial uncertainty and provide an initial covariance matrix which was set to:

$$\boldsymbol{C}_0 = \begin{bmatrix} .02^2 & 0 & 0 \\ 0 & .25^2 & 0 \\ 0 & 0 & .02^2 \end{bmatrix} [km^2]$$

Since we want to emphasize the error of the model rather than the error of the propagation method we have chosen a compromise between computational complexity and uncertainty realism, e.g. accuracy. In order to propagate the initial covariance we used the Unscented Transform method.
UT can enforce a high degree of covariance realism (see Section 2.4) while containing the computational costs, offering a good compromise between the linear (simplest) and the ideal Monte Carlo approach. With such method, we propagated the covariance (i.e. sigma-points) for both ground truth and analytical models under tests. The sample propagation of the ground truth covariance was performed fully numerically.

We tested our proposed model against the two state of the art models: Bombardelli and Gonzalo.
Figure 4.7 reports the error of the position mean. As it can be seen, the position mean error is coherent with previous section.
Figure 4.8 reports instead the error of the positional covariance. Taking again into consideration the results of Chapter 3, we can draw qualitative conclusion about the applicability of the model as uncertainty propagator to conjunction assessment. Assuming as acceptable a log-Pc error of 10% at 1σ level (i.e. 68% of conjunctions), the propagated covariance can be biased at most by half the bound in Section 3, i.e. 77.5 meters. Regarding the models performance then, one can see that in this use case all the models could be used with acceptable

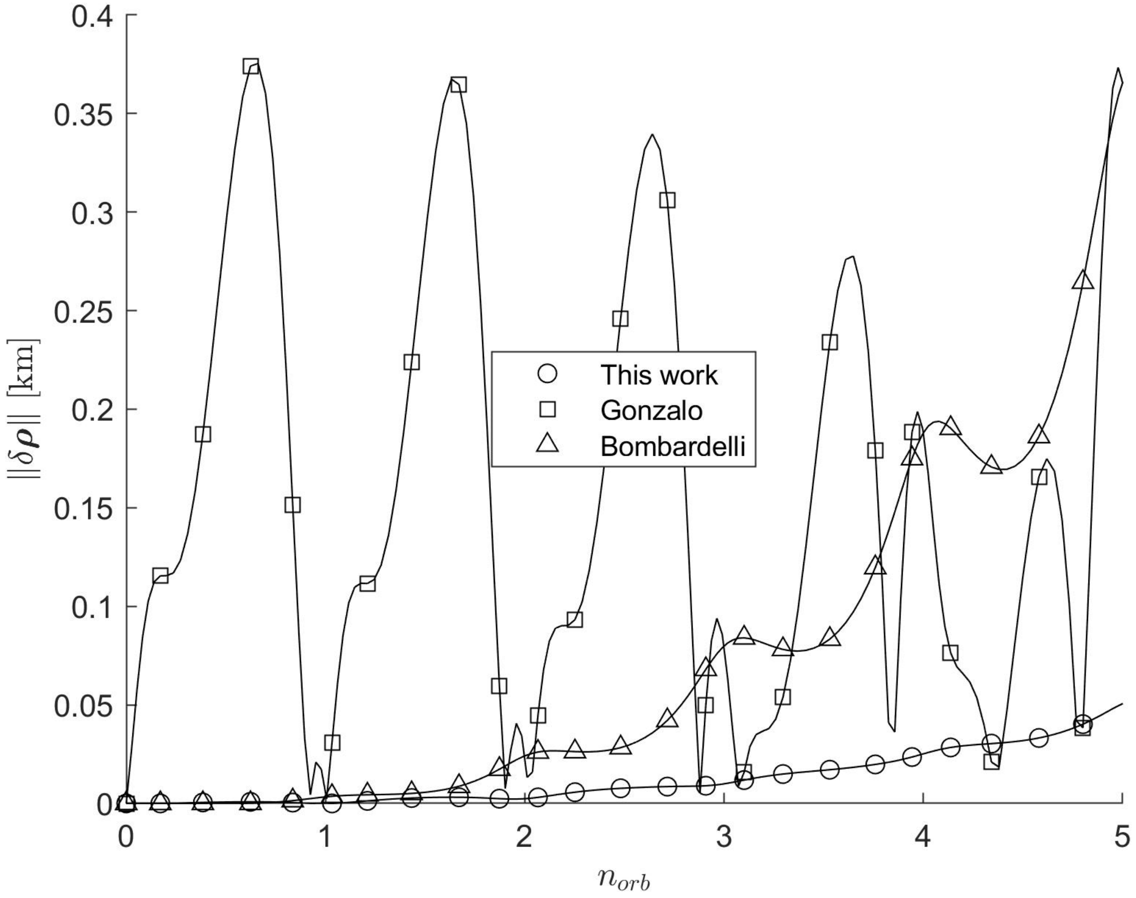

Figure 4.7: Error of position mean against numerical solution for proposed model and other state of the art methods using Unscented Transform

errors on the first 5 orbital periods of propagation and potentially even beyond. Figure 4.8 also depicts that despite the better positional accuracy of each propagated sigma-point, the improvement in covariance accuracy of the proposed model is not as large as the one in the position accuracy. Nonetheless, it has been shown to provide sufficient accuracy, both in position and covariance predictions, for COLA application on longer propagation periods.

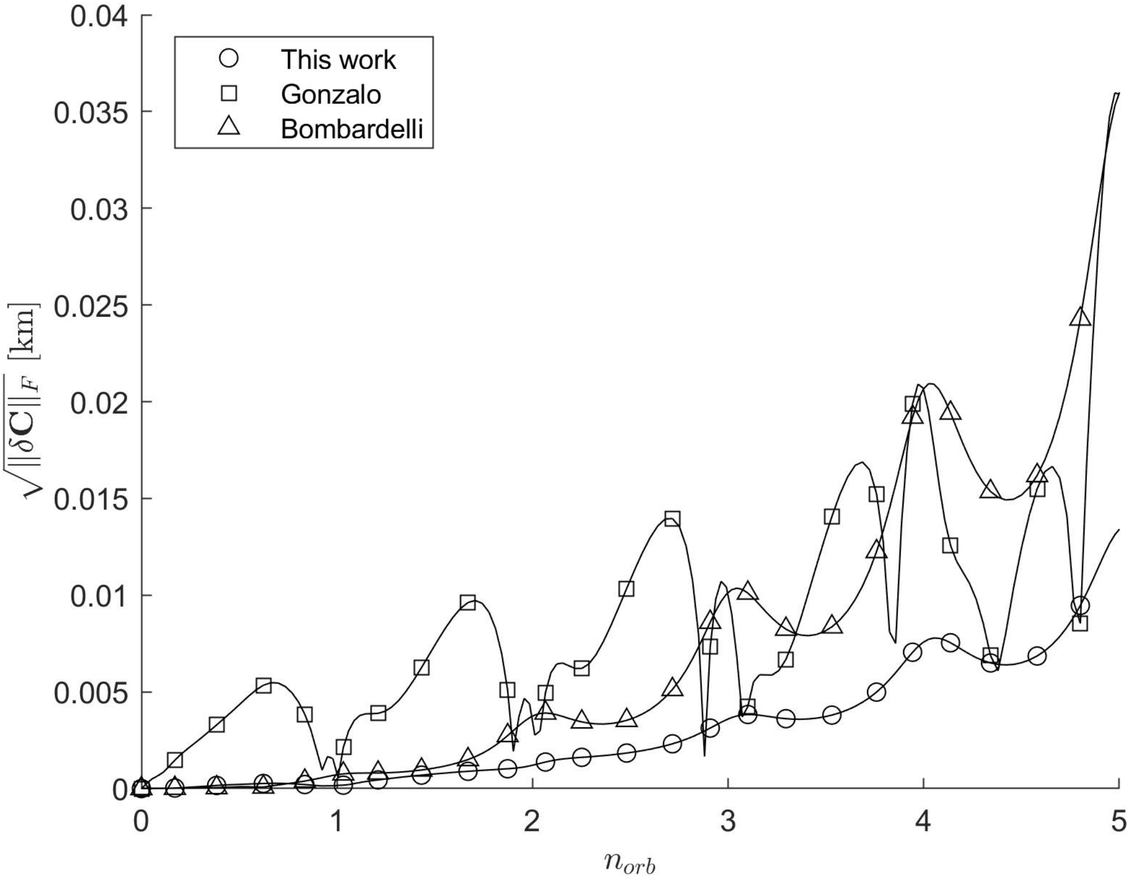

Figure 4.8: Error of position covariance in frobenious norm against numerical solution for proposed model and other state methods of the art using Unscented Transform

4.6 Chapter Appendix

4.6.1 Non-dimensional GPE form

We will make here use of the identities

$$\|\boldsymbol{v}\| = na\sqrt{\frac{1+e\cos E}{1-e\cos E}}$$

$$\cos f = \frac{\cos E - e}{1-e\cos E}$$

$$\sin f = \sqrt{1-e^2}\frac{\sin E}{1-e\cos E}$$

Let us furthermore recall the non-dimensional thrust definition as vector $\boldsymbol{\epsilon} = [\epsilon_\eta \; \epsilon_\tau \; \epsilon_n]^T = \boldsymbol{a}_p/\sqrt{\mu/a_c^2}$

Starting from the Gauss Planetary equation provided by Battin (1999) at Problem 10-7 we have:

$$\begin{aligned}
\frac{d\tilde{a}}{d\tilde{t}} &= 2\tilde{a}^{3/2}\sqrt{\frac{1+e\cos E}{1-e\cos E}}\epsilon_\tau \\
\frac{de}{d\tilde{t}} &= \sqrt{\tilde{a}}\sqrt{\frac{1-e\cos E}{1+e\cos E}}\left[\frac{2(1-e^2)\cos E}{1-e\cos E}\epsilon_\tau - \sqrt{1-e^2}\sin E\;\epsilon_\eta\right] \\
\frac{di}{d\tilde{t}} &= \sqrt{\frac{\tilde{a}}{1-e^2}}(\cos E - e)\epsilon_n \\
\frac{d\Omega}{d\tilde{t}} &= \sqrt{\tilde{a}}\frac{1-e\cos E}{\sin i}\sin E\;\epsilon_n \\
\frac{d\omega}{d\tilde{t}} &= \frac{\sqrt{\tilde{a}}}{e}\sqrt{\frac{1-e\cos E}{1+e\cos E}}\left[\frac{2\sqrt{1-e^2}\sin E}{1-e\cos E}\epsilon_\tau + (e+\cos E)\epsilon_\eta\right] + \\
&\quad - \sqrt{\tilde{a}}\frac{1-e\cos E}{\sqrt{1-e^2}}\frac{\cos i}{\sin i}\epsilon_n \\
\frac{dM}{d\tilde{t}} &= \sqrt{\tilde{a}^{-3}} - \frac{1-e^2}{e}\sqrt{\tilde{a}}\sqrt{\frac{1-e\cos E}{1+e\cos E}}\left[\frac{2(1-e^3\cos E)}{\sqrt{1-e^2}}\frac{\sin E}{1-e\cos E}\epsilon_\tau + \right. \\
&\quad \left. (\cos E - e)\;\epsilon_\eta\right]
\end{aligned} \tag{4.30}$$

Rewriting the latter in terms of eccentric anomaly instead of mean anomaly, one has:

$$\frac{dE}{d\tilde{t}} = \frac{\tilde{a}^{-3/2}}{1-e\cos E} - \frac{\sqrt{\tilde{a}}}{e}\sqrt{\frac{1-e\cos E}{1+e\cos E}}\left[\frac{2\sin E}{1-e\cos E}\epsilon_\tau + \sqrt{1-e^2}\cos E\;\epsilon_\eta\right]$$

4.6.2 Non-dimensional GPE gradient in perturbation

The rows of the 6×3 matrix evaluated at $\boldsymbol{\epsilon} = \mathbf{0}$ are:

$$\nabla_{\epsilon} \frac{d\tilde{a}}{dE} = (1 - e\cos E) \begin{bmatrix} 0 \\ 2\tilde{a}^3 \sqrt{\frac{1+e\cos E}{1-e\cos E}} \\ 0 \end{bmatrix}^T$$

$$\nabla_{\epsilon} \frac{de}{dE} = (1 - e\cos E)\tilde{a}^2 \sqrt{\frac{1 - e\cos E}{1 + e\cos E}} \begin{bmatrix} -\sqrt{1-e^2}\sin E \\ \frac{2(1-e^2)\cos E}{1-e\cos E} \\ 0 \end{bmatrix}^T$$

$$\nabla_{\epsilon} \frac{di}{dE} = (1 - e\cos E)\tilde{a}^{3/2} \begin{bmatrix} 0 \\ 0 \\ \sqrt{\frac{\tilde{a}}{1-e^2}}(\cos E - e) \end{bmatrix}^T$$

$$\nabla_{\epsilon} \frac{d\Omega}{dE} = (1 - e\cos E)\tilde{a}^{3/2} \begin{bmatrix} 0 \\ 0 \\ \sqrt{\tilde{a}}\frac{1-e\cos E}{\sin i}\sin E \end{bmatrix}^T$$

$$\nabla_{\epsilon} \frac{d\omega}{dE} = (1 - e\cos E)\frac{\tilde{a}^2}{e} \sqrt{\frac{1 - e\cos E}{1 + e\cos E}} \begin{bmatrix} (e + \cos E) \\ \frac{2\sqrt{1-e^2}\sin E}{1-e\cos E} \\ \sqrt{\tilde{a}}\frac{1-e\cos E}{\sqrt{1-e^2}}\frac{\cos i}{\sin i} \end{bmatrix}^T$$

$$\nabla_{\epsilon} \frac{d\tilde{t}}{dE} = -(1 - e\cos E)^2 \frac{\tilde{a}^{7/2}}{e} \begin{bmatrix} \sqrt{1-e^2}\cos E \\ \frac{2\sin E}{\sqrt{1-e^2\cos^2 E}} \\ 0 \end{bmatrix}^T$$

4.6.3 Some recurrent integrals

An analytic solution for the integrals of $E\sqrt{1 - e_c^2\cos^2 E}$ or $\frac{E}{\sqrt{1-e_c^2\cos^2 E}}$ is not known at the authors. Therefore, we adopted an expansion of the elliptic part of the integrand function to approximate a solution

$$\sqrt{1 - e_c^2\cos^2 E} = 1 - \frac{e_c^2}{2}\cos^2 E - \frac{e_c^4}{8}\cos^4 E + \mathcal{O}(e_c^6)$$

$$\frac{1}{\sqrt{1 - e_c^2\cos^2 E}} = 1 + \frac{e_c^2}{2}\cos^2 E + \frac{e_c^4}{8}\cos^4 E + \mathcal{O}(e_c^6)$$

Being the eccentricity typically between 0 and 1, we considered satisfactory an expansion of 4-th order around null eccentricity.
Then the integrals involving either $E\sqrt{1-e_c^2\cos^2 E}$ or $\frac{E}{\sqrt{1-e_c^2\cos^2 E}}$, both reduces to the sum or subtraction of integrals of the type:

$$\begin{aligned} I_{c2} &= \int E\cos^2 E dE = \frac{E^2}{4} - \frac{\sin^2 E}{8} + \frac{\cos^2 E}{8} + \frac{E}{2}\sin E\cos E \\ I_{c4} &= \int E\cos^4 E dE = \frac{3E^2}{16} + \frac{E\sin(2E)}{4} + \frac{E\sin(4E)}{32} + \frac{\cos(2E)}{8} + \frac{\cos(4E)}{128} \\ I_{c6} &= \int E\cos^6 E dE = \frac{5E^2}{32} + \frac{15E\sin(2E)}{64} + \frac{3E\sin(4E)}{64} + \frac{E\sin(6E)}{192} + \\ &\qquad \frac{15\cos(2E)}{128} + \frac{3\cos(4E)}{256} + \frac{\cos(6E)}{1152} \end{aligned}$$

Whereas another useful integral of the same kind is:

$$\begin{aligned} I_{EsF} = \int \frac{E\sin E}{\sqrt{1-e_c^2\cos^2 E}}\, dE \cong \int E\sin E\, dE + \frac{e_c^2}{2}\int E\sin E\cos^2 E\, dE + \\ \frac{3e_c^4}{8}\int E\sin E\cos^4 E\, dE \end{aligned}$$

Other recurrent integrals that can be analytically solved are those involving sine and cosine multiplying elliptic functions:

$$\begin{aligned}
I_{sc} &= \int \sin E \sqrt{\frac{1 - e\cos E}{1 + e\cos E}} \cos E \; dE = \\
&\quad - \frac{1}{2e_c^2}\left(\frac{-e_c^3 \cos^3 E + 2e_c^2 \cos^2 E + e_c \cos E - 2}{\sqrt{1 - e_c^2 \cos^2 E}} + \right. \\
&\quad \left. + \, 2\arcsin\sqrt{\frac{1 - e_c \cos E}{2}} \right) \\
I_{sc2} &= \int \sin E \frac{\cos^2 E}{(1 + e\cos E)\sqrt{1 - e_c^2 \cos^2 E}} dE = \\
&\quad \frac{\frac{\sqrt{1 - e_c^2 \cos^2 E}(2 + e_c \cos E)}{1 + e_c \cos E} + \arcsin\left(e_c \cos E\right)}{e_c^3} \\
I_{sc3} &= \int \sin E \frac{\cos^2 E}{\sqrt{1 - e_c^2 \cos^2 E}} dE = \\
&\quad \frac{\cos E}{2e_c^2}\sqrt{1 - e_c^2 \cos^2 E} - \frac{\arcsin\left(e_c \cos E\right)}{2e_c^3} \\
I_s &= \int \sin E \sqrt{1 - e_c^2 \cos^2 E} dE = \\
&\quad - \frac{\cos E}{2}\sqrt{1 - e_c^2 \cos^2 E} - \frac{\arcsin\left(e_c \cos E\right)}{2e_c}
\end{aligned}$$

A useful recurrence is also noticed using the integrals:

$$\begin{aligned}
I_{c0F} &= \int \frac{1}{\sqrt{1 - e_c^2 \cos^2 E}} dE = \frac{F\left[E|\mathsf{k}\right]}{\sqrt{1 - e_c^2}} \\
I_{c1F} &= \int \frac{\cos E}{\sqrt{1 - e_c^2 \cos^2 E}} dE = \frac{1}{e_c} \operatorname{arsinh}\left(\frac{e_c}{\sqrt{1 - e_c^2}} \sin E \right) \\
I_{c2F} &= \int \frac{\cos^2 E}{\sqrt{1 - e_c^2 \cos^2 E}} dE = \frac{F\left[E|\mathsf{k}\right] + \left(e_c^2 - 1\right) E\left[E|\mathsf{k}\right]}{e_c^2 \sqrt{1 - e_c^2}} \\
I_{c3F} &= \int \frac{\cos^3 E}{\sqrt{1 - e_c^2 \cos^2 E}} dE = \\
&\quad \frac{\left(e_c^2 + 1\right) \operatorname{artanh}\left(\frac{e_c sin E}{\sqrt{1 - e_c^2 \cos^2 E}} \right) - e_c \sin E \sqrt{1 - e_c^2 \cos^2 E}}{2e_c^3},
\end{aligned} \tag{4.31}$$

where we recall that $\mathsf{k} = \frac{e_c^2}{(e_c^2 - 1)}$.

In fact, multiplying and dividing by $\sqrt{1 \pm e_c \cos E}$ which is always different from 0 for elliptic orbits, one can show that:

$$\int \sqrt{\frac{1 \pm e_c \cos E}{1 \mp e_c \cos E}} \cos^i E \, dE = I_{ciF} \pm e_c \, I_{c(i+1)F}$$

5

Conclusions

This thesis has reported the results obtained as part of the PhD research on efficient tools for management of satellite constellations.
After identifying the main technical and operational challenges to be faced for the sustainability of satellite constellations, a main line of research was identified in the space traffic management and collision avoidance operations using low thrust electric propulsion. As in the era of large constellations the number of collision warnings is expected to become too large to be handled by manual procedures, the on-board automation of (at least part) of the COLA process would be a great asset. This, in turn, has led the investigation towards the development of efficient analytic methods for orbit propagation under low trust and the formulation of the research questions:

1. Which are the requirements for an orbit propagator under low thrust to be used for COLA operations?
2. Can we fulfil such requirements with an efficient analytic orbit propagator?

To answer the first question, we considered the problem of satellites conjunction assessment adopting as risk metric the probability of collision in the encounter plane, which is the most widely adopted index. For such metric, we enforced a desired maximum error, and derived accuracy requirements for both

position and positional covariance propagation.
With the propagation requirements, we studied a couple of show-cases arriving at a classification of low thrust systems characteristics that shall be taken into account when applying low thrust to COLA operations. We concluded that the systematic error on the realized low thrust is the most significant source of error for the collision metric if not taken into account.
Given the importance of accounting for propulsion systems characteristics in COLA, we moved the focus on analytic orbit propagation models for such systems, to answer research question 2.

Inspired by recent literature on analytical models for perturbed motion, we developed a novel solution method which improves state of the art propagation accuracy, both in terms of position and positional covariance predictions. We based our analytical model on the theory of averaging applied to a linearized version of Gauss Planetary Equations. The main merit of the proposed approach is that of relaxing the commonly employed hypothesis of keeping constant the slow orbital elements while integrating GPE.
After recognizing the relevance of *tangential maneuvers* in COLA, we specialized the model to such case, and assessed its performance on several numerical test cases. Results suggest the proposed model is a good candidate to be used for COLA applications, for instance to optimize low thrust maneuvers that starts few orbit before the TCA (3-4 orbits).

5.1 Limitations and future work

As future work, we mention the possibility of formulating the problem in some non-singular orbital elements. In fact, a limitation is the increasing error of the model when approaching null eccentricities. Towards circular orbits in fact, the intrinsic error resulted to increase sensibly because of the formulation in singular Keplerian orbital elements.
Furthermore, to accurately model cases approaching unitary eccentricity, higher order expansions for solving the most complex integrals are desirable. In fact, towards parabolic orbits, the global error increases because of the approximations involved in integrating complex elliptic integrals.

Another limitation lies in the range of accelerations up to which the prediction accuracy meets the COLA requirements. Although the 1e-7km/s^2 limit includes a large amount of the available low thrust propulsion systems, there exist other orbital perturbations that may exceed this limit, and thereby could be embedded in the model developed herein only at the price of significantly degraded accuracy. For instance, J2 acceleration in LEO is in the order of 1e-6, 1e-5 km/s^2. One possibility to overcome such limitation, at least for conservative perturbations, is the formulation of the problem in a set of orbital elements that could absorb such major perturbations, similarly to the J2-equinoctial elements proposed in (Bau et al., 2021).

Bibliography

G. Acciarini, C. Greco, and M. Vasile. On the Solution of the Fokker-Planck Equation without Diffusion for Uncertainty Propagation in Orbital Dynamics. *2020 AAS/AIAA Astrodynamics Specialist Conference, South Lake Tahoe, CA*, Aug. 2020.

K. T. Alfriend, M. R. Akella, J. Frisbee, J. L. Foster, D. jin Lee, and M. Wilkins. Probability of collision error analysis. *Kluwer Academic*, Space Debris 1:21–35, May 1999. doi: 10.1023/A:1010056509803.

D. Amato, A. J. Rosengren, and C. Bombardelli. THALASSA: a fast orbit propagator for near-earth and cislunar space. *2018 Space Flight Mechanics Meeting, Kissimmee, Florida*, 2018.

M. S. Balch. A Corrector for Probability Dilution in Satellite Conjunction Analysis. *18th AIAA Non-Deterministic Approaches Conference*, Jan. 2016. doi: 10.2514/6.2016-1445.

M. S. Balch, R. Martin, and S. Ferson. Satellite Conjunction Analysis and the false confidence theorem. *Procedings Royal Society A*, 475:1–20, 2019. doi: 10.1098/rspa.2018.0565.

R. H. Battin. *An Introduction to the Mathematics and Methods of Astrodynamics, Revised Edition*. AIAA education series, 1999. ISBN 0-13-805326-X.

G. Bau, J. Hernando-Ayuso, and C. Bombardelli. A generalization of the equinoctial orbital elements. *Celestial Mechanics and Dynamical Astronomy*, pages 1–32, 2021. doi: 10.1007/s10569-021-10049-1.

C. Bombardelli and J. Hernando-Ayuso. Collision avoidance maneuver optimization. *Advances in the Astronautical Sciences*, 152(7402):1857–1870, Jan. 2014.

C. Bombardelli, G. Baù, and J. Peláez. Asymptotic solution for the two-body problem with constant tangential thrust acceleration. *Celestial Mechanics and Dynamical Astronomy*, 110, 2011. doi: 10.1007/s10569-011-9353-3.

L. D. Brown, T. T. Cai, and A. DasGupta. Interval estimation for a binomial proportion. *Statistical Science*, 16(2):101–133, 2001. doi: 10.1214/ss/1009213286.

F. D. Bruijn, F. Letizia, and J. C. Bastante. Operational concept for orbit raising with low thrust. *Proc. 26th International symposium on Space Flight Dynamics*, June 2017.

P. F. Byard and M. D. Friedman. *Handbook of elliptic integrals for engineers and scientists*. Springer, 1970. ISBN 0-387-05318-2.

J. R. Carpenter and F. L. Markley. Wald Sequential Probability Ratio Test for Space Object Conjunction Assessment. *NASA Goddard Space Flight Center, Greenbelt, MD 20771*, pages 1–30, 2014. doi: 10.2514/1.G000478.

J. R. Carpenter, F. L. Markley, and D. Gold. Sequential Probability Ratio Test for Collision Avoidance Maneuver Decisions. *The Journal of the Astronautical Sciences*, 59(1):273–286, 2012. doi: 10.1007/s40295-013-0017-2.

J. R. Carpenter, S. Alfano, D. T. Hall, M. D. Hejduk, J. A. Gaebler, M. K. Jah, S. O. Hasan, R. L. Besser, R. R. DeHart, M. G. Duncan, M. S. Herron, and W. J. Guit. Relevance of the american statistical Society's warning on p-values for conjunction assessment. *AAS/AIAA Astrodynamics Specialist Conference, Stevenson, WA*, pages 1–19, Aug. 2017.

F. Castellini, G. Bellei, and F. Budnik. Bepicolombo orbit determination activities during electric propulsion arcs. *Proc. AIAA Scitech 2020 Forum*, Jan. 2020.

F. K. Chan. *Spacecraft collision probability*. American Institute of Aeronautics and Astronautics, Inc, second edition, 2008.

Z. Chen, Y. Qu, H. Deng, W. Zhong, Z. He, and W. Deng. Near-Earth Orbit Satellite Collision Probability Estimation and Collision Avoidance. *Chinese Au-*

tomation Congress, pages 855–860, Nov. 2019. doi: 10.1109/CAC48633.2019.8996239.

S. Clark, P. Randall, R. Lewis, D. Marangone, D. Goebel, V. Chaplin, H. Gray, K. Kempkens, and N. Wallace. Bepicolombo - solar electric propulsion system test and qualification approach. *Proc. 36th International Electric Propulsion Conference*, Sept. 2019.

V. T. Coppola. Including velocity uncertainty in the probability of collision between space objects. *Proceedings of the 22nd AAS/AIAA Space Flight Mechanics Meeting, Univelt, San Diego, CA*, 143:2159–2178, 2012.

G. Curzi and D. Modenini. Analytic solution for perturbed keplerian motion under small acceleration using averaging theory. *Advances in Space Research*, 2022. Manuscript submitted for publication.

G. Curzi, D. Modenini, and P. Tortora. Large constellations of small satellites: A survey of near future challenges and missions. *Aerospace*, 7(133):1–18, 2020. doi: 10.3390/aerospace7090133.

T. Denoeux. Logistic regression, neural networks and Dempster–Shafer theory: A new perspective. *Knowledge-Based Systems*, 176:54–67, 2019. doi: 10.1016/j.knosys.2019.03.030.

M. Di Carlo, S. da Graça Marto, and M. Vasile. Extended analytical formulae for the perturbed Keplerian motion under low-thrust acceleration and orbital perturbations. *Celestial Mechanics and Dynamical Astronomy*, 133(13):1–39, 2021. doi: 10.1007/s10569-021-10007-x.

W. Ding, X. Li, H. Yang, Z. Zhang, and J. An. An Analytical Method for Calculating Short-Term Space Interception Probability. *International Journal of Aerospace Engineering*, page 23, Nov. 2019. doi: 10.1155/2019/5316396.

ESA. Collision avoidance challenge - data, 2019. URL `https://kelvins.esa.int/collision-avoidance-challenge/data/`.

L. S. Fernández-Mellado and M. Vasile. On the use of Machine Learning and Evidence Theory to improve collision risk management. *Acta Astronautica*, 181:694–706, 2021. doi: 10.1016/j.actaastro.2020.08.004.

C. R. Fox and G. Ülkümen. Chapter 1: Distinguishing two dimensions of uncertainty. *Perspectives on Thinking, Judging, and Decision Making, Oslo, Universitetsforlaget*, pages 22–28, 2011.

G. Goff, J. T. Black, and J. A. Beck. Short arc radar observation considerations in covariance intersection. *International Journal of Space Science and Engineering*, 3(1):50–67, 2015. doi: 10.1504/IJSPACESE.2015.069358.

J. L. Gonzalo and C. Colombo. Lightweight algorithms for collision avoidance applications. *11th International ESA Conference on Guidance, Navigation and Control Systems*, June 2021.

J. L. Gonzalo, C. Colombo, and P. Di Lizia. A semi-analytical approach to low-thrust collision avoidance manoeuvre design. *70th International Astronautical Congress*, Oct. 2019.

J. L. Gonzalo, C. Colombo, and P. Di Lizia. Introducing MISS, a new tool for collision avoidance analysis and design. *Journal of Space Safety Engineering*, 7 (3):282–289, 2020. ISSN 2468-8967. doi: 10.1016/j.jsse.2020.07.010.

M. Graziano, F. Pirondini, N. Sánchez, and E. D. Sotto. CRYOSAT collision warning and low thrust avoidance manoeuvre strategy. *Proceedings of the 3rd European Conference on Space Debris, ESOC*, Mar. 2001. doi: ESASP-473.

L. Gremyachikh, D. Dubov, N. Kazeev, A. Kulibaba, A. Skuratov, A. Tereshkin, A. Ustyuzhanin, L. Shiryaeva, and S. Shishkin. SPACE NAVIGATOR: A tool for the optimization of collision avoidance maneuvers. *IAA-AS-SciTech2018-068, Advances in Astronautial Sciences*, 170:303–318, Feb. 2020. doi: 10.1109/CAC48633.2019.8996239.

M. D. Hejduk. Satellite Conjunction Assessment Risk Analysis for "Dilution Region" Events: Issues and Operational Approaches. *Space Traffic Management Conference*, 28, 2019.

J. Hernando-Ayuso and C. Bombardelli. Low-thrust collision avoidance in circular orbits. *Journal of Guidance, Control, and Dynamics*, 44(5):983–995, 2021. doi: 10.2514/1.G005547.

J. T. Horwood, Navraj Singh, and Jeffrey M. Aristoff. KRATOS: Kollision Risk Assessment Tool in Orbital Element Spaces. *Proceedings of the 2016 Advanced Maui Optical and Space Surveillance Technologies Conference*, 2016.

B. A. Jones and A. Doostan. Satellite collision probability estimation using polynomial chaos expansions. *Advances in Space Research*, 52:1860–1875, 2013. doi: 10.1016/j.asr.2013.08.027.

A. D. Kiureghian and O. Ditlevsen. Aleatory or epistemic? does it matter? *Advanced Maui Optical and Space Surveillance Technologies Conference, Maui, Hawai'i*, 31(2):105–112, 2009.

F. J. Krage. *NASA Spacecraft Conjunction Assessment and Collision Avoidance Best Practices Handbook*. American Institute of Aeronautics and Astronautics, Inc, 2020. URL `https://nodis3.gsfc.nasa.gov/OCE_docs/OCE_50.pdf`.

E. Kulu. Satellite constellations - 2021 industry survey and trends. *35th Annual Small Satellite Conference, Utah State University Logan, UT*, pages 1–20, 2021.

Kumar Vishwajeet and Puneet Singla. Adaptive Split/Merge-Based Gaussian Mixture Model Approach for Uncertainty Propagation. *Journal Of Guidance, Control, And Dynamics*, 41(3):603–617, Mar. 2018. doi: 10.2514/1.G002801.

A. Kyle and T. PARK. When does the uncertainty become non-gaussian. *Advanced Maui Optical and Space Surveillance Technologies Conference, Maui, Hawai'i*, Sept. 2016.

B. Lal, E. de la Rosa Blanco, J. R. Behrens, B. A. Corbin, E. K. Green, A. J. Picard, and A. Balakrishnan. Global Trends in Small Satellites, July 2017.

Y.-Z. Luo and Z. Yang. A review of uncertainty propagtion in orpital mechanics. *Progress in Aerospace Sciences*, 89:23–29, 2017. doi: 10.1016/j.paerosci.2016.12.002.

M. Matney, P. Anz-Meador, and J. L. Foster. Covariance correlations in collision avoidance probability calculations. *Advances in Space Research*, 34:1109–1114, 2004. doi: 10.1016/j.asr.2003.11.012.

K. Merz, B. B. Virgili, V. Braun, T. Flohrer, Q. Funke, H. Krag, S. Lemmens, and J. Siminsky. Current Collision avoidance Service by ESA's Space Debris Office. *ESA Space Debris Office*, Apr. 2017.

L. Miraux. Environmental limits to the space sector's growth. *Science of The Total Environment*, 806(150862):1–10, 2022. doi: 10.1016/j.scitotenv.2021.150862.

D. Morante, M. Sanjurjo Rivo, and M. Soler. A survey on low-thrust trajectory optimization approaches. *Aerospace*, 8(3), 2021. ISSN 2226-4310. doi: 10.3390/aerospace8030088.

T. J. Muelhaupt, M. E. Sorge, J. Morin, and R. S. Wilson. Space traffic management in the new space era. *The Journal of Space Safety Engineering*, May 2019. doi: 10.1016/j.jsse.2019.05.007.

R. P. Patera. General Method for Calculating Satellite Collision Probability. *Journal of Guidance, Control, and Dynamics*, 24(4):716–722, July 2001. ISSN 0731-5090, 1533-3884. doi: 10.2514/2.4771.

R. P. Patera. Satellite Collision Probability for Nonlinear Relative Motion. *Journal Of Guidance, Control, And Dynamics*, 26(5), Oct. 2003. doi: 10.2514/2.5127.

A. Petit, E. M. Alessi, and A. Rossi. Low-thrust strategies and implications in the perspective of space debris mitigation for large constellations. *First Int'l. Orbital Debris Conf*, 2019.

F. Pinto, G. Acciarini, S. Metz, S. Boufelja, S. Kaczmarek, K. Merz, J. A. Martinez-Heras, F. Letizia, C. Bridges, and A. G. Baydin. Towards automated satellite conjunction management with bayesian deep learning. *AI for Earth Sciences Workshop at NeurIPS 2020*, 2020.

A. B. Poore, J. M. Aristoff, and J. T. Horwood. Covariance and Uncertainty Realism in Space Surveillance and Tracking. *Numerica Corporation Fort Collins United States*, pages i – 161, June 2016.

W. Richardson-Little, C. Patterson, and G. Peake. Collision Avoidance Management for Earth Observation Constellation Missions. *First Int'l. Orbital Debris Conf*, 2019.

L. Sanchez, M. Vasile, and E. Minisci. AI to Support Decision Making in Collision Risk Assessment. *Ienternational Astronautical Congress 2019,* 2019. doi: IAC-19-A6/IP/20/x53728.

J. Sanders, F. Verhulst, and J. Murdock. *Averaging Methods in Nonlinear Dynamical Systems.* Springer, 2000. ISBN 0-387-48916-9.

V. Schaeffer, S. Laurens, P. Seimandi, and F. Delmas. Collision probability through time integration Implementation and operational results. *2018 SpaceOps Conference*, June 2018. doi: 10.2514/6.2018-2720.

R. Serra, D. Arzeiler, M. Joldes, J.-B. Laserre, A. Rodepierre, and B. Salvy. Fast and Accurate Computation for orbital Collision Probability for Short-Term Encounters. *Journal Of Guidance, Control, And Dynamics*, 39(5):1009–1021, May 2016. doi: 10.2514/1.G001353.

G. Shafer. *A mathematical theory of evidence.* Princeton University press, 1976.

J. R. Vetter. Fifty Years of Orbit Determination: Development of Modern Astrodynamics Methods. *Johns Hopkins APL Technical Digest*, 27(3):239–252, 2007.

E. A. Wan and R. V. D. Merwe. The unscented kalman filter for nonlinear estimation. *Proceedings of the IEEE 2000 Adaptive Systems for Signal Processing, Communications, and Control Symposium*, pages 153–158, 2000.

J. W. Widhalm and S. A. Heise. Optimal in-plane orbital evasive maneuvers using continuous thrust propulsion. *Journal of Guidance, Control, and Dynamics*, 14(6):1323–1326, 1991. doi: 10.2514/3.20793.

M. Willis and S. D'Amico. Analytical approach to spacecraft formation-flying with low-thrust relative spiral trajectories. *Acta Astronautica*, 153:175–190, 2018. doi: 10.1016/j.actaastro.2018.02.002.

G. Yang. Near-optimal very low-thrust earth-orbit transfers and guidance schemes. *Journal of Guidance, Control, and Dynamics*, 30(2):529–539, 2007. doi: 10.2514/1.24836.

Z. Yang, Y.-Z. Luo, and J. Zhang. Nonlinear semi-analytical uncertainty propagation of trajectory under impulsive maneuvers. *Astrodynamics*, 3(1):61–77, 2019. doi: 10.1007/s42064-018-0036-7.

G. Zhang and Y. Geng. Minimizing the Effects of Impulsive Orbit Maneuver Uncertainty. *Journal of aerospace engineering*, 31(5):04018055, 2018. doi: 10.1061/(ASCE)AS.1943-5525.0000890.

F. Zuiani, M. Vasile, A. Palmas, and G. Avanzini. Direct transcription of low-thrust trajectories with finite trajectory elements. *Acta Astronautica*, 72:108–120, 2012. ISSN 0094-5765. doi: 10.1016/j.actaastro.2011.09.011.